AN EXAMINATION OF THE ARCTIC ENVIRONMENT AND ARCTIC CYCLONES DURING PERIODS OF LOW AND HIGH FORECAST SKILL OF THE SYNOPTIC-SCALE FLOW

by

Kevin A. Biernat

A Dissertation

Submitted to the University at Albany, State University of New York

In Partial Fulfillment of

the Requirements for the Degree of

Doctor of Philosophy

College of Arts & Sciences

Department of Atmospheric and Environmental Sciences

2021

ABSTRACT

This dissertation compares Arctic environmental conditions and Arctic cyclones (ACs) between periods of low and high forecast skill of the synoptic-scale flow over the Arctic during summer, hereafter referred to as low-skill periods and high-skill periods, respectively. This dissertation also examines features and processes influencing the evolution and forecast skill of selected categories of ACs.

Climatologies of low-skill and high-skill periods during the summers of 2007–2017, and climatologies of ACs occurring during low-skill and high-skill periods, are constructed to compare Arctic environmental conditions and ACs between these respective periods. The Arctic environment tends to be characterized by greater synoptic-scale flow amplitude, greater lower-to-midtropospheric Eady growth rates, greater moisture transport, and greater latent heating during low-skill periods compared to high-skill periods. ACs occur more frequently across much of the Arctic, tend to be stronger, and tend to be embedded in more favorable dynamic and thermodynamic environments for development and intensification during low-skill periods compared to high-skill periods. Four skill categories of ACs are determined based on the forecast skill of intensity of ACs: low-skill ACs during low-skill periods, high-skill ACs during low-skill periods, low-skill ACs during high-skill periods, and high-skill ACs during high-skill periods. Low-skill ACs during low-skill periods are found to be relatively strong, and embedded in regions of relatively large lower-tropospheric baroclinicity, relatively large lower-to-midtropospheric Eady growth rates, relatively large moisture transport, and relatively large latent heating, when compared to the other skill categories of ACs.

Features and processes influencing the development and intensification of strong low-skill ACs during low-skill periods and strong high-skill ACs during low-skill periods are

examined and compared through AC-centered composites for these respective categories of ACs. The composite analysis for the strong low-skill ACs during low-skill periods suggests that these ACs interact with tropopause polar vortices (TPVs) in a region of strong lower-to-midtropospheric baroclinicity and relatively large lower-to-midtropospheric Eady growth rates, and that these ACs are associated with a corridor of moisture transport and well-defined regions of latent heating. The features and processes influencing the evolution of the strong high-skill ACs during low-skill periods tend to be less robust compared to the features and processes influencing the evolution of the strong low-skill ACs during low-skill periods.

Features and processes influencing the forecast skill of a strong low-skill AC during a low-skill period in August 2016 (AC16) are examined by utilizing the ensemble-based sensitivity analysis (ESA) technique and by comparing the most-accurate and least-accurate ensemble forecasts of AC16. The ESA and the comparison of the most-accurate and least-accurate ensemble forecasts of AC16 suggest that the predictability of AC16 is sensitive to the amplitude and strength of an upper-tropospheric trough, and to the strength of an embedded TPV, upstream of AC16. It is speculated from the ESA and the comparison of the most-accurate and least-accurate ensemble forecasts that a more amplified and stronger upper-tropospheric trough, and a stronger embedded TPV, upstream of AC16 are associated with greater downstream upper-tropospheric flow amplification and greater intensification of AC16. It is also speculated from the ESA and the comparison of the most-accurate and least-accurate ensemble forecasts that the position of a moisture corridor and a region of latent heating associated with AC16 may matter more to the predictability of AC16 than the amount of moisture in the moisture corridor and the magnitude of latent heating.

ACKNOWLEDGMENTS

I would like to thank my co-advisors, Drs. Lance Bosart and Daniel Keyser, for their advisement, mentorship, and support throughout the last seven years. It has been a pleasure to work with them and learn from them. I am very grateful to them for helping me to grow as a scientist and a writer. I would also like to thank the remaining members of my Ph.D. committee, Drs. Steven Cavallo, Andrea Lang, and Ryan Torn, for their guidance and insights.

Thanks go to the faculty and staff in the Department of Atmospheric and Environmental Sciences at the University at Albany for the high-quality education, and for technical and administrative support. Thanks go to my friends and fellow graduate students for their support and camaraderie.

Thanks go to my family for their love and support throughout my time in graduate school. Their encouragement has meant a lot to me and has supported me throughout my graduate journey.

Financial support provided by Office of Naval Research Grant N00014-18-1-2200.

TABLE OF CONTENTS

1. Introduction

a. Motivation and objectives

The Arctic environment is rapidly changing in response to enhanced near-surface warming relative to the rest of the globe, referred to as Arctic amplification, and diminishing sea ice (e.g., Stroeve et al. 2007; Screen and Simmonds 2010; Dai et al. 2019). As the Arctic environment rapidly changes, human activities, including shipping, tourism, and military operations, are increasing in the Arctic (e.g., Hall and Saarinen 2010; Eguíluz et al. 2016; Jung et al. 2016; Melia et al. 2016, 2017; Maher 2017; U.S. Department of the Navy 2021). Accurate weather prediction over the Arctic is important given that these human activities can be impacted by weather conditions in the Arctic. Previous studies have examined the forecast skill of short-to-medium-range (1–15-day) forecasts of 500-hPa geopotential height over the Arctic (e.g., Jung and Leutbecher 2007; Bauer et al. 2016; Jung and Matsueda 2016; Sandu and Bauer 2018), providing insight into the forecast skill of the synoptic-scale flow over the Arctic. Forecast skill of the synoptic-scale flow over the Arctic has been shown to be lower than that over middle latitudes (e.g., Sandu and Bauer 2018). However, there has been a dearth of research concerning Arctic environmental conditions associated with periods of low and high forecast skill of the synoptic-scale flow over the Arctic, aside from a recent study by Yamagami and Matsueda (2021). In this dissertation, Arctic environmental conditions refer to the state of the troposphere in the Arctic described in terms of the synoptic-scale flow, horizontal and vertical motions, baroclinicity, moisture, and latent heating. Improving understanding of Arctic environmental conditions associated with periods of low and high forecast skill of the synoptic-scale flow over the Arctic is important given that these conditions may be associated with adverse impacts on human activities in the Arctic.

Arctic cyclones (ACs) are synoptic-scale surface cyclones that may originate within the Arctic or move into the Arctic from lower latitudes (e.g., Serreze 1995; Zhang et al. 2004; Serreze and Barrett 2008; Simmonds and Rudeva 2012, 2014; Crawford and Serreze 2016; Valkonen et al. 2021). ACs occur most frequently during summer (e.g., Zhang et al. 2004; Serreze and Barrett 2008) and may play important roles in influencing Arctic environmental conditions and the forecast skill of the synoptic-scale flow over the Arctic (e.g., Yamagami and Matsueda 2021). ACs may be associated with strong surface winds and high waves (e.g., Holt and Martin 2001; Asplin et al. 2012; Zhang et al. 2013; Thomson and Rogers 2014), may transport warm, moist air into the Arctic (e.g., Moore 2016; Binder et al. 2017; Messori et al. 2018; Fearon et al. 2021), and may contribute to rapid sea ice loss and rapid sea ice movement (e.g., Asplin et al. 2012; Parkinson and Comiso 2013; Zhang et al. 2013; Stern et al. 2020; Lukovich et al. 2021; Peng et al. 2021). It is critical to improve understanding of features and processes influencing the evolution and forecast skill of ACs because strong surface winds, high waves, rapid sea ice loss, and rapid sea ice movement associated with ACs can have significant impacts on human activities in the Arctic (e.g., Inoue 2020). Previous studies that have examined features and processes influencing the evolution of ACs have primarily been conducted through case studies of selected ACs (e.g., Simmonds and Rudeva 2012; Tanaka et al. 2012; Aizawa et al. 2014; Tao et al. 2017a,b; Yamagami et al. 2017). In addition, there have been a limited number of studies that have examined features and processes influencing the forecast skill of ACs (e.g., Tao et al. 2017b; Yamagami et al. 2018a; Johnson and Wang 2021).

The overarching objective of this research is to improve understanding of Arctic environmental conditions and ACs during periods of low and high forecast skill of the synoptic-scale flow over the Arctic during summer. Specifically, this dissertation aims to: 1) examine

characteristics of the Arctic environment and the frequency, characteristics, and forecast skill of ACs during periods of low and high forecast skill of the synoptic-scale flow over the Arctic, 2) examine features and processes influencing the evolution of strong ACs associated with low forecast skill and strong ACs associated with high forecast skill during periods of low forecast skill of the synoptic-scale flow over the Arctic, and 3) examine features and processes influencing the forecast skill of a selected strong AC associated with low forecast skill during a period of low forecast skill of the synoptic-scale flow over the Arctic.

b. Literature review

1) Forecast skill over the Arctic

There is relatively sparse coverage of conventional data in the Arctic, but there is relatively large areal coverage and relatively high spatial density of satellite sounding data in the Arctic (e.g., Lawrence et al. 2019). Analysis uncertainty has been shown to be greater in the Arctic compared to the middle latitudes, particularly for near-surface variables like 2-m temperature over snow and ice (e.g., Bauer et al. 2016; Jung and Matsueda 2016). Short-to-medium-range (1–15-day) forecast skill of the synoptic-scale flow over the Arctic in terms of short-to-medium-range forecast skill of 500-hPa geopotential height over the Arctic has been evaluated by Jung and Leutbecher (2007), Bauer et al. (2016), Jung and Matsueda (2016), and Sandu and Bauer (2018). Sandu and Bauer (2018) conclude that forecast skill over the Arctic is lower than that over Northern Hemisphere middle latitudes based on day-6 anomaly correlation coefficient (ACC) of 500-hPa geopotential height for the European Centre for Medium-Range Weather Forecasts (ECMWF) operational system and ERA-Interim during 1990–2016. However, Jung and Matsueda (2016) conclude that forecast skill over the Arctic is slightly lower

than, but comparable to, that over Northern Hemisphere middle latitudes based on ACC of 1–15 day forecasts of 500-hPa geopotential height for the control runs of nine different ensemble prediction systems (EPSs) during the winters of 2006/2007 to 2012/2013. The different forecast lead times, datasets, and time periods used for Arctic forecast skill evaluation by Sandu and Bauer (2018) and Jung and Matsueda (2016) may contribute to the different conclusions reached by these respective studies. Furthermore, Sandu and Bauer (2018) evaluate Arctic forecast skill over 60–90°N, whereas Jung and Matsueda (2016) evaluate Arctic forecast skill over 65–90°N, which may also contribute to the different conclusions reached by these respective studies. Jung and Matsueda (2016) show that the average forecast skill over the Arctic during winter, in terms of the forecast lead time at which the ACC of 500-hPa geopotential height over the Arctic falls below 0.6, ranges between 6 and 9.5 days for the control runs of the EPSs examined.

Although there has been research that has examined the forecast skill of the synoptic-scale flow over the Arctic, there has been a dearth of research that has examined Arctic environmental conditions associated with periods of low and high forecast skill of the synoptic-scale flow over the Arctic, with the exception of a recent study by Yamagami and Matsueda (2021). Yamagami and Matsueda (2021) identify forecast busts over the Arctic based on ACC and root mean square error of day-6 forecasts of 500-hPa geopotential height over the Arctic for the control runs of five different EPSs during 2008–2019. They show that the largest proportion of forecast busts generally occurs during summer, the season during which ACs occur most frequently (e.g., Zhang et al. 2004; Serreze and Barrett 2008). They examine Arctic weather patterns associated with forecast busts during summer at forecast initialization, and find that one of the most frequent patterns is referred to as the "Arctic Cyclone" pattern, which is characterized by anomalously low 500-hPa geopotential height and sea level pressure (SLP) over

the Arctic. Although not discussed by Yamagami and Matsueda (2021), the "Arctic cyclone" pattern may be related to the positive phase of the Arctic Oscillation (AO), which is also characterized by anomalously low 500-hPa geopotential height and SLP over the Arctic (e.g., Thompson and Wallace 1998; Ogi et al. 2004; Serreze and Barrett 2008). Yamagami and Matsueda (2021) suggest that forecast busts over the Arctic during summer may be linked to forecast errors in synoptic-scale systems such as ACs. Since ACs may influence forecast skill of the synoptic-scale flow over the Arctic, it would be instructive to understand how the frequency of ACs, intensity of ACs, and dynamic and thermodynamic environments in which ACs are embedded in compare between periods of low and high forecast skill of the synoptic-scale flow over the Arctic.

It has been shown that forecast errors propagating along upper-tropospheric waveguides and forecast errors associated with features embedded within upper-tropospheric waveguides (e.g., troughs and ridges) can contribute to forecast errors in the synoptic-scale flow over the middle latitudes (e.g., Sanders 1992; Langland et al. 2002; Hakim 2005; Davies and Didone 2013; Lamberson et al. 2016; Lillo and Parsons 2017; Torn 2017; Baumgart et al. 2018; Berman and Torn 2019). It has also been shown that forecast errors related to baroclinic processes (e.g., Tribbia and Baumhefner 2004; Davies and Didone 2013; Boisseri et al. 2014; Selz and Craig 2015; Berman and Torn 2019) and latent heating (e.g., Davies and Didone 2013; Rodwell et al. 2013; Madonna et al. 2015; Lamberson et al. 2016; Martínez-Alvarado et al. 2016; Grams et al. 2018; Berman and Torn 2019) can contribute to forecast errors in the synoptic-scale flow over the middle latitudes. It is anticipated that forecast errors propagating along upper-tropospheric waveguides, forecast errors associated with features embedded within upper-tropospheric

waveguides, and forecast errors related to baroclinic processes and latent heating may also contribute to forecast errors in the synoptic-scale flow over the Arctic.

2) ACs

(i) Climatologies of ACs

There are seasonal differences in the frequency, location, lifetime, and intensity of ACs. ACs have primarily been shown in previous studies to track more frequently over Eurasia, the Laptev, East Siberian, and Chukchi Seas, and the Arctic Ocean during summer compared to winter, and more frequently over the North Atlantic, and the Greenland, Norwegian, and Barents Seas during winter compared to summer (e.g., Zhang et al. 2004; Serreze and Barrett 2008; Crawford and Serreze 2016; Valkonen et al. 2021) (see Fig. 1.1 hereafter for map of Arctic geography). Zhang et al. (2004) and Crawford and Serreze (2016) also show that ACs track more frequently over northern Baffin Bay and the Gulf of Alaska during winter compared to summer. ACs are more likely to undergo genesis over Eurasia during summer compared to winter and over the North Atlantic, and the Greenland, Norwegian, and Barents Seas during winter compared to summer (e.g., Serreze 1995; Zhang et al. 2004; Serreze and Barrett 2008; Crawford and Serreze 2016; Valkonen et al. 2021). AC genesis over Eurasia during summer may be linked in part to a reduction in static stability associated with turbulent and radiative heat fluxes from the heated landmass, lee cyclogenesis downstream of mountain ranges over northern Eurasia, and upper-tropospheric divergence associated with frequent upper-tropospheric troughs east of the Ural Mountains (e.g., Crawford and Serreze 2016).

ACs moving into the Arctic from Eurasia during summer may be influenced by a band of strong lower-tropospheric horizontal thermal gradient along the Arctic coast, referred to as the

Arctic frontal zone (AFZ) (e.g., Serreze et al. 2001; Serreze and Barrett 2008; Crawford and Serreze 2015, 2016). The AFZ becomes established due to differential heating of the atmosphere between the heated landmass of Eurasia and the cold Arctic Ocean and sea ice, and has been shown to contribute to the intensification of ACs crossing the Arctic coast (e.g., Serreze et al. 2001; Serreze and Barrett 2008; Crawford and Serreze 2015, 2016). Crawford and Serreze (2016) do not find the AFZ to act as a generator of ACs, and so they do not find AC genesis frequency maxima along the Arctic coast during summer. AC genesis and intensification over the North Atlantic, and the Greenland, Norwegian, and Barents Seas during winter can be linked to dynamical support and baroclinicity associated with the North Atlantic storm track (e.g., Serreze 1995; Madonna et al. 2020). Crawford and Serreze (2016) show that there is an AC genesis frequency maximum off the southeast coast of Greenland during both winter and summer, which likely relates to lee cyclogenesis associated with westerly flow over southern Greenland and to secondary cyclone development associated with cyclones approaching Greenland from the south (e.g., Serreze et al. 1997). Crawford and Serreze (2016) discuss that ACs tend to undergo cyclolysis during winter and summer over similar regions as to which they undergo genesis, as well as tend to undergo cyclolysis during winter and summer across the Arctic Ocean.

ACs tend to be stronger during winter compared to summer, with the strongest ACs attaining peak intensities in the 930–940-hPa range during winter and in the 960–970-hPa range during summer (e.g., Zhang et al. 2004; Simmonds and Rudeva 2012, 2014; Valkonen et al. 2021). ACs can have lifetimes ranging from a few days to a few weeks (e.g., Zhang et al. 2004; Simmonds and Rudeva 2012, 2014; Tanaka et al. 2012; Yamagami et al. 2017), with longer lifetimes observed during summer compared to winter (e.g., Zhang et al. 2004; Simmonds and

Rudeva 2014). The Great Arctic Cyclone of August 2012, hereafter referred to as AC12, is a notable strong and long-lasting summer AC that has been extensively studied (e.g., Simmonds and Rudeva 2012; Zhang et al. 2013; Yamazaki et al. 2015; Tao et al. 2017b; Yamagami et al. 2018a; Stern et al. 2020). AC12 attained a peak intensity of approximately 962 hPa and had a lifetime of approximately 13 days in the ERA5 dataset (from an analysis conducted by the author of this dissertation). Simmonds and Rudeva (2012) find that out of a total of 1618 ACs occurring in August during 1979–2012, AC12 is the most intense AC in terms of lowest SLP attained when located in the Arctic (north of 70°N) and 12th longest-lived AC in terms of lifetime spent in the Arctic. In addition, AC12 has been shown to lead to rapid and widespread sea ice loss (Parkinson and Comiso 2013; Zhang et al. 2013; Stern et al. 2020).

(ii) Features and processes influencing the evolution of ACs

Features and processes influencing the evolution of ACs have primarily been investigated from a case study perspective of selected ACs (e.g., Simmonds and Rudeva 2012; Tanaka et al. 2012; Aizawa et al. 2014; Aizawa and Tanaka 2016; Tao et al. 2017a,b; Yamagami et al. 2017). Tropopause polar vortices (TPVs) have been shown to play important roles in the development and intensification of ACs (e.g., Simmonds and Rudeva 2012, 2014; Tanaka et al. 2012; Aizawa and Tanaka 2016; Tao et al. 2017a,b; Yamagami et al. 2017). TPVs are coherent tropopause-based cyclonic vortices that are characterized by a local minimum of dynamic tropopause (DT) potential temperature, a cyclonic potential vorticity (PV) anomaly, and anomalously cold air throughout the depth of the troposphere (e.g., Cavallo and Hakim 2009, 2010, 2012). TPVs occur frequently over the Arctic and can be transported into middle latitudes, where they have been shown to contribute to the development of intense midlatitude cyclones (e.g., Hakim et al. 1995;

Bosart et al. 1996), cold air outbreaks (e.g., Biernat et al. 2021; Lillo et al. 2021), and tornado outbreaks (Bray et al. 2021). Hoskins et al. (1985, section 6e) show that an upper-tropospheric cyclonic PV anomaly (e.g., a TPV) moving over a baroclinic zone can lead to the development of a lower-tropospheric cyclonic PV anomaly (e.g., a surface cyclone), and further show that these PV anomalies can become phase-locked and mutually amplify one another. AC12 (e.g., Simmonds and Rudeva 2012; Tao et al. 2017a) and a strong AC that occurred during August 2016, hereafter referred to as AC16 (Yamagami et al. 2017), have been shown to develop and intensify downshear of TPVs in baroclinic zones associated with high Eady growth rates. Yamagami et al. (2017) show the importance of baroclinic processes to the intensification of AC16. AC16 attained a minimum SLP of 967 hPa in the ERA-Interim dataset (Yamagami et al. 2017) and contributed to rapid sea ice loss (Peng et al. 2021). Yamagami et al. (2017) show that AC16 is characterized by strong lower-tropospheric relative vorticity and intensifies as it moves east-northeastward north of Eurasia and merges with a second AC located over the Arctic. Yamagami et al. (2017) further show that AC16 intensifies in regions of strong baroclinicity that are characterized by strong lower-tropospheric horizontal temperature gradients and high midtropospheric Eady growth rates. Yamagami et al. (2017) discuss that AC16 is associated with warm and cold frontal structures as AC16 intensifies.

TPVs can be associated with regions of baroclinicity throughout the troposphere and upper-tropospheric jet streaks that influence AC development and intensification (e.g., Yamazaki et al. 2015; Tao et al. 2017b; Johnson and Wang 2021). An analysis of the evolution of AC12 from Tao et al. (2017b) will be used to discuss how TPVs can be associated with regions of baroclinicity throughout the troposphere and upper-tropospheric jet streaks that influence AC development and intensification. Since AC12 is a very strong AC, the evolution exhibited by

AC12 will not apply to all ACs, especially weaker ACs. Still, features and processes influencing the evolution of AC12 may influence the evolution of weaker ACs, but to a lesser extent. Tao et al. (2017b) show that during the "incipient stage" of AC12, a strong thermal gradient (related to the AFZ) contributes to a strong baroclinic zone throughout the troposphere and an associated upper-tropospheric jet streak. They show that a TPV interacting with this jet streak contributes to the intensification of the jet streak, and show that upper-tropospheric divergence in the right-entrance region of the jet streak supports tropospheric ascent and the formation of AC12. Pyle et al. (2004) show that TPVs interacting with upper-tropospheric jets can contribute to the intensification of DT potential temperature gradients associated with the jets and to the concomitant formation and intensification of upper-tropospheric jet streaks.

Tao et al. (2017b) show that as AC12 intensifies during the "early development stage," cold and warm temperature advections lead to deformation of the baroclinic zone throughout the troposphere and to splitting of the upper-tropospheric jet streak into two jet streaks. They show that associated with the formation of the two jet streaks is an increase in upper-tropospheric divergence and tropospheric ascent between the two jet streaks, supporting the intensification of AC12. Afterward, they show that during the "drastic intensification period," strong temperature advections continue to deform the baroclinic zone throughout the troposphere, with the two jet streaks transitioning into a stronger, cyclonically curved jet streak on the eastern side of the TPV, which has moved closer to AC12. They further show that associated with this stronger jet streak is stronger upper-tropospheric divergence and tropospheric ascent within the left-exit region of the jet streak above AC12. The stronger upper-tropospheric divergence and tropospheric ascent, combined with interaction between the TPV and AC12, contribute to the rapid intensification of AC12 (Tao et al. 2017b).

AC12 also merges with a second, weaker AC during the "drastic intensification period" (Yamazaki et al. 2015; Tao et al. 2017b). Similarly, and as discussed previously, Yamagami et al. (2017) show that AC16 merges with a second AC as AC16 intensifies. The merger of ACs has been shown to occur in association with the merger of lower-tropospheric vorticity and lower-tropospheric PV associated with ACs, and the concomitant merger of TPVs that may be linked to the merging ACs (e.g., Aizawa et al. 2014; Yamagami et al. 2017). Yamagami et al. (2017) illustrate that the merger of ACs can prolong AC lifetime, with the lifetime AC16 being prolonged due to multiple mergers with other ACs.

Tao et al. (2017b) show that after AC12 rapidly intensifies, it becomes vertically coupled with the TPV, resulting in an equivalent barotropic structure and associated tropospheric-deep cyclonic circulation, which is similarly shown in other studies of ACs coupling with TPVs (e.g., Aizawa et al. 2014; Aizawa and Tanaka 2016; Tao et al. 2017a; Yamagami et al. 2017). Aizawa et al. (2014) show that during the vertical coupling of a strong AC with a TPV during June 2008, downward advection of PV from a cyclonic PV maximum associated with the TPV and upward advection of PV from a cyclonic PV maximum associated with the AC contribute to the vertical merging of the PV maxima. The vertical merging of the PV maxima is associated with the formation of a tropospheric-deep PV tower. ACs, once vertically coupled with TPVs, may meander around the Arctic for relatively long periods of time (e.g., Tao et al. 2017b; Yamagami et al. 2017).

Latent heating may also contribute to the development and intensification of ACs. Latent heating associated with the formation of clouds and precipitation has been shown to contribute to the development and intensification of midlatitude cyclones in numerous studies (e.g., Tracton 1973; Kuo and Reed 1988; Reed et al. 1988, 1992; Kuo et al. 1991; Davis et al. 1993; Stoelinga

1996; Dickinson et al. 1997; Wernli et al. 2002; Doyle et al. 2014, 2019). However, there has been a dearth of research that has examined the role of latent heating in the development and intensification of ACs. ACs can be associated with intrusions of warm, moist air into the Arctic (e.g., Binder et al. 2017; Messori et al. 2018; Fearon et al. 2021), which may be related to atmospheric rivers (ARs) and warm conveyor belts (WCBs) of ACs. Fearon et al. (2021) show that moist intrusions associated with ACs occur most frequently from Scandinavia, Russia, and Alaska during summer, and most frequently from the North Atlantic, and Barents and Kara Seas during winter. Fearon et al. (2021) also show that sources of moisture for moist intrusions associated with ACs include surface evaporation over the Atlantic Gulf Stream throughout the year and surface evaporation over high-latitude continental landmasses, especially Eurasia, during summer. A sounding within a corridor of warm and moist air on the eastern side of AC12 at 0000 UTC 5 August 2012 for Cherskij, Russia, which is located near the northeastern Russian coast, is associated with a value of convective available potential energy (CAPE) of 119.4 J kg^{-1} (not shown). This value of CAPE suggests that the warm and moist air associated with AC12 has the potential to support deep convection.

Upper-tropospheric cyclonic PV anomalies, such as TPVs, that influence AC development can be associated with upward motion on the downshear side of the PV anomalies (e.g., Hakim 2000; Cavallo and Hakim 2010) that occur in response to cyclonic PV advection (e.g., Hoskins et al. 1985, section 4). The upward motion combined with moisture within the ARs and WCBs of ACs may contribute to the formation of clouds and precipitation. Latent heating associated with the formation of clouds and precipitation may contribute to lower-tropospheric cyclonic PV production, which may contribute to the intensification of ACs, as shown to occur with midlatitude cyclones (e.g., Reed et al. 1992; Davis et al. 1993; Wernli et al.

2002). In addition, latent heating may contribute to a reduction of static stability in the troposphere, which may strengthen upward vertical motions and contribute to larger Rossby penetration depths of upper-tropospheric cyclonic PV anomalies associated with TPVs and of lower-tropospheric cyclonic PV anomalies associated with ACs (Hoskins et al. 1985, section 6e). The larger Rossby penetration depths of the upper-tropospheric and lower-tropospheric cyclonic PV anomalies may result in stronger coupling and mutual amplification of the PV anomalies and, consequently, stronger ACs (Hoskins et al. 1985, section 6e).

(iii) Forecast skill of ACs

There have been a limited number of predictability studies of ACs in the literature, but interest in AC predictability has recently been growing. Yamagami et al. (2018a) examine the forecast skill of AC12 with five operational EPSs, and find that accurate forecasts of AC12 only extend out to 2–3-day lead times relative to the time of peak intensity of AC12. Yamagami et al. (2018b) examine and compare the forecast skill of 10 extraordinary ACs occurring during the summers of 2008–2016 with five operational EPSs, and Yamagami et al. (2019) examine the forecast skill of 26 extraordinary ACs occurring during the summers of 1986–2016 (including the aforementioned 10 extraordinary ACs) with the National Oceanic and Atmospheric Administration (NOAA) Global Ensemble Forecast System (GEFS) reforecast dataset version 2. Extraordinary ACs were determined by Yamagami et al. (2018b, 2019) to be ACs that attain a minimum SLP of < 980 hPa when located north of 70°N and that are associated with a 250-hPa temperature anomaly, averaged within 800 km of the AC center, of > 5 K. A warm 250-hPa temperature anomaly can be a signature of a TPV (e.g., Yamagami et al. 2018a). Yamagami et al. (2019) show that average forecast errors in the intensity and position of the 10 and 26

extraordinary ACs for the time of peak intensity of the extraordinary ACs increase as forecast lead time increases across the various EPSs. For example, Yamagami et al. (2019) show that for the 26 extraordinary ACs in the GEFS reforecast dataset version 2, the average forecast error in the intensity of these extraordinary ACs increases from around 3 hPa for the 1-day lead time to around 12 hPa for the 7-day lead time, and the average forecast error in the position of these extraordinary ACs increases from around 100 km for the 1-day lead time to around 800 km for the 7-day lead time. Yamagami et al. (2019) indicate that stronger extraordinary ACs tend to be associated with larger intensity errors, especially for lead times of > 5 days. Yamagami et al. (2018b) state that the forecast skill of extraordinary ACs is lower than that of midlatitude cyclones in the Northern Hemisphere. Capute and Torn (2021) compare the forecast skill of the intensity and position of ACs and of midlatitude cyclones over the North Atlantic using the GEFS reforecast dataset version 2. They show that ACs are less predictable in terms of position compared to midlatitude cyclones over the North Atlantic, and show that ACs are more predictable in terms of intensity compared to midlatitude cyclones over the North Atlantic.

Although there have been numerous studies that have examined features and processes influencing the forecast skill of midlatitude cyclones (e.g., Langland et al. 2002; Zhang et al. 2003; Chang et al. 2013; Zheng et al. 2013; Doyle et al. 2014, 2019; Lamberson et al. 2016), there have been relatively few studies that have examined features and processes influencing the forecast skill of ACs. Forecast errors propagating along upper-tropospheric waveguides and forecast errors associated with features embedded within upper-tropospheric waveguides (e.g., troughs and ridges) have been shown to contribute to forecasts errors in midlatitude cyclones (e.g., Langland et al. 2002; Chang et al. 2013; Zheng et al. 2013; Lamberson et al. 2016). In addition, forecast errors related to baroclinic processes (e.g., Sanders 1986; Zhu and Thorpe

2006; Zhang et al. 2007; Zheng et al. 2013) and latent heating (e.g., Zhang et al. 2003, 2007; Doyle et al. 2014, 2019) have been shown to contribute to forecast errors in midlatitude cyclones. It is anticipated that forecast errors propagating along upper-tropospheric waveguides, forecast errors associated with features embedded within upper-tropospheric waveguides, and forecast errors related to baroclinic processes, moisture, and latent heating may also contribute to forecast errors in ACs.

The forecast skill of AC12 has been shown to be sensitive to the position and strength of TPVs and to the strength of tropospheric baroclinicity (Yamazaki et al. 2015; Tao et al. 2017b; Yamagami et al. 2018a). Tao et al. (2017b) perform two sensitivity experiments for AC12 in which 1) tropospheric baroclinicity is weakened, and 2) the TPV influencing the evolution of AC12 is weakened. The sensitivity experiments illustrate that weakening the tropospheric baroclinicity and weakening the TPV contribute to weaker upper-tropospheric jet streaks influencing the evolution of AC12 and concomitantly a weaker AC12. Johnson and Wang (2021) conduct an ensemble sensitivity analysis of an AC occurring during July 2018 and find that track and intensity errors of the AC are sensitive to the structure of a large-scale Rossby wave, the position and intensity of TPVs embedded within the Rossby wave, midtropospheric moisture located within the WCB of the AC, and the structure of the lower-tropospheric thermal field. Observing system experiments by Yamazaki et al. (2015) and Johnson and Wang (2021) show that the denial of radiosonde observations located in the vicinity of TPVs linked to the development of AC12 and the AC during July 2018, respectively, significantly degrade the forecasts of the ACs.

c. Research contributions and novel aspects of dissertation

As discussed in the literature review, there is a dearth of research regarding how Arctic environmental conditions and ACs compare between periods of low and high forecast skill of the synoptic-scale flow over the Arctic, hereafter referred to as low-skill and high-skill periods, respectively. This dissertation aims to improve understanding of how Arctic environmental conditions and ACs compare between low-skill and high-skill periods by constructing climatologies of low-skill and high-skill periods for the summers of 2007–2017 using the NOAA GEFS reforecast dataset version 2, and by constructing AC climatologies for these periods using an ERA-Interim cyclone climatology. Characteristics of the Arctic environment and the frequency, location, and characteristics of ACs are compared between low-skill and high-skill periods using the ERA-Interim dataset. Additionally, the forecast skill of ACs is compared between low-skill and high-skill periods using the NOAA GEFS reforecast dataset version 2. Characteristics of ACs that are associated with low forecast skill, hereafter referred to as low-skill ACs, are compared to those of ACs that are associated with high forecast skill, hereafter referred to as high-skill ACs.

Also, as discussed in the literature review, features and processes influencing the evolution of ACs have primarily been investigated from a case study perspective of selected ACs. Accordingly, composite analyses of ACs are lacking in the literature. This dissertation aims to improve understanding of features and processes influencing the evolution of ACs by conducting AC-centered composite analyses for strong low-skill ACs and strong high-skill ACs during low-skill periods using the ERA5 dataset. Consideration is restricted to low-skill periods because low-skill periods may pose greater challenges to human activities in the Arctic that rely on accurate weather prediction compared to high-skill periods. Strong low-skill ACs during low-

skill periods may pose particularly great challenges to human activities in the Arctic relative to strong high-skill ACs during low-skill periods, and it is of interest to determine how these strong low-skill ACs and strong high-skill ACs may evolve differently. Future work should also consider the evolution of strong low-skill ACs and strong high-skill ACs during high-skill periods to determine how these ACs may evolve differently relative to those during low-skill periods. Strong low-skill ACs during high-skill periods may still pose challenges to human activities in the Arctic because the forecast skill of the synoptic-scale flow over the Arctic during high-skill periods would suggest that ACs occurring during high-skill periods would be high-skill ACs and not low-skill ACs. Lastly, as discussed in the literature review, features and processes influencing the forecast skill of ACs have been investigated in only a few predictability studies. This dissertation aims to improve understanding of features and processes influencing the forecast skill of ACs by performing forecast error and sensitivity analyses of a selected strong low-skill AC during a low-skill period using the ECMWF EPS.

d. Hypotheses

In pursuit of the objectives stated in section 1a and expanded upon in section 1c, and based on the literature review presented in section 1b, the following five hypotheses will be addressed in this dissertation.

1. The Arctic environment tends to be characterized by greater synoptic-scale flow amplitude, greater baroclinic growth rates, and greater latent heating during low-skill periods compared to high-skill periods.
2. ACs occur more frequently across the Arctic, tend to be stronger, tend to be embedded in in more favorable dynamic and thermodynamic environments for development and

intensification, and tend to be characterized by lower forecast skill during low-skill periods compared to high-skill periods.

3. Low-skill ACs during low-skill periods tend to be stronger and tend to be embedded in more favorable dynamic and thermodynamic environments for development and intensification compared to high-skill ACs during low-skill periods. Similarly, low-skill ACs during high-skill periods tend to be stronger and tend to be embedded in more favorable dynamic and thermodynamic environments for development and intensification compared to high-skill ACs during high-skill periods.
4. TPVs, baroclinic zones, and WCBs, and TPV–AC interactions, baroclinic processes, and latent heating, influence the evolution of strong low-skill ACs during low-skill periods and strong high-skill ACs during low-skill periods, although these features and processes tend to be more robust for strong low-skill ACs during low-skill periods.
5. Forecast errors in TPVs, baroclinic zones, and WCBs, and forecast errors in TPV–AC interactions, baroclinic processes, and latent heating, contribute to forecast errors in strong low-skill ACs during low-skill periods.

e. Organization of dissertation

The remainder of this dissertation is organized as follows. Chapter 2 presents a climatological comparison of the Arctic environment and ACs between low-skill and high-skill periods. Chapter 3 presents an examination of features and processes influencing the evolution of strong low-skill ACs during low-skill periods and strong high-skill ACs during low-skill periods. Chapter 4 presents an examination of features and processes influencing the forecast skill of a

selected strong low-skill AC during a low-skill period. Chapter 5 provides a summary, conclusions, and recommendations for future work.

f. Figure

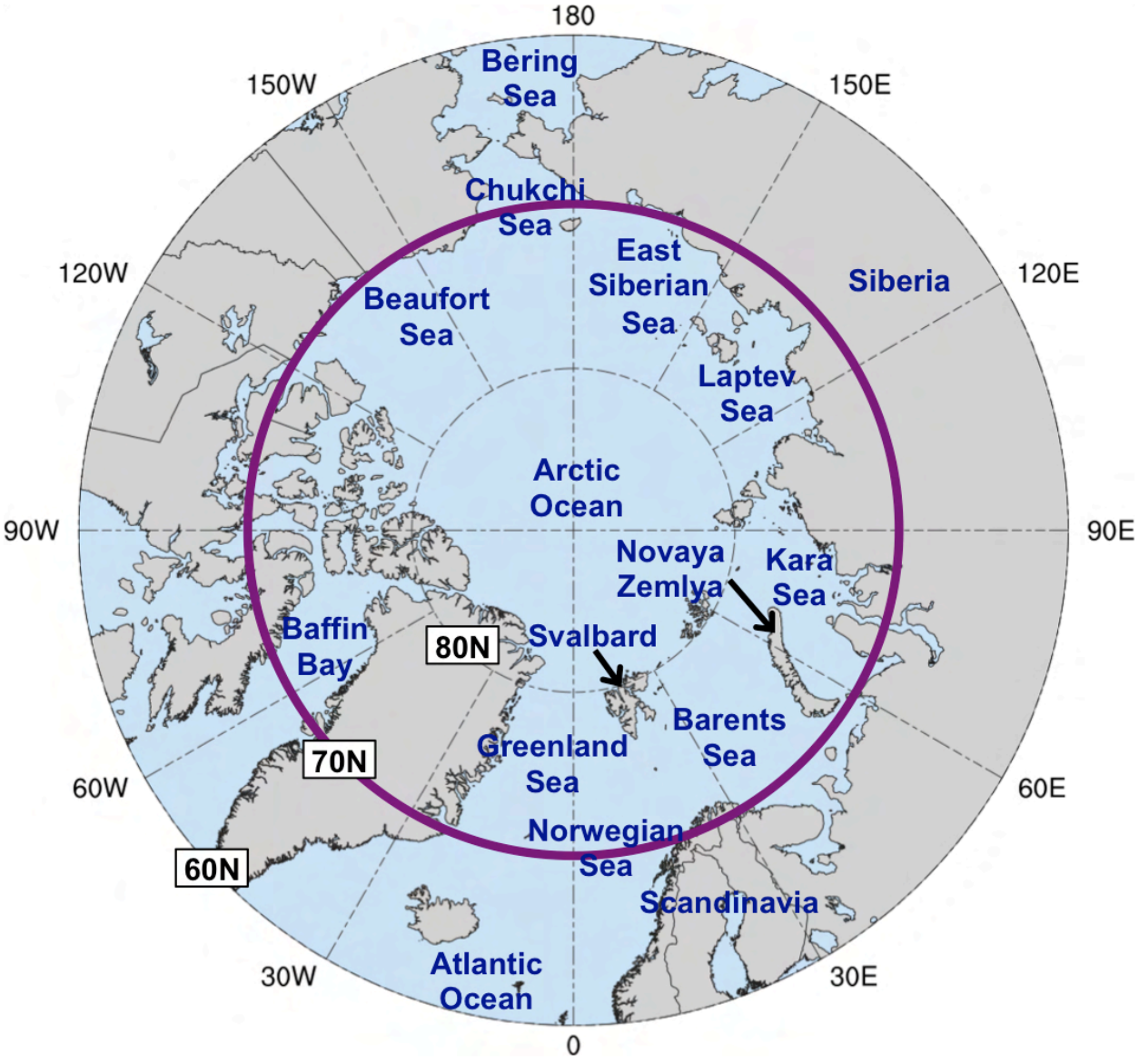

Fig. 1.1. Map of Arctic geography, including names of seas and nations. Anywhere north of the purple circle (70°N) denotes the Arctic for the purposes of this dissertation.

2. Climatological comparison of the Arctic environment and of ACs between low-skill and high-skill periods

a. Overview and objectives

In this chapter, hypotheses 1–3 are addressed. Hypothesis 1 states that the Arctic environment tends to be characterized by greater synoptic-scale flow amplitude, greater baroclinic growth rates, and greater latent heating during low-skill periods compared to high-skill periods. Hypothesis 1 is addressed by constructing 2007–2017 climatologies of low-skill and high-skill periods, and by comparing characteristics of the Arctic environment between these respective periods. Hypothesis 2 states that ACs occur more frequently across the Arctic, tend to be stronger, tend to be embedded in more favorable dynamic and thermodynamic environments for development and intensification, and tend to be characterized by lower forecast skill during low-skill periods compared to high-skill periods. Hypothesis 2 is addressed by constructing 2007–2017 climatologies of ACs during low-skill and high-skill periods, and by comparing the frequency, characteristics, and forecast skill of the ACs between the respective periods. Hypothesis 3 states that low-skill ACs during low-skill periods tend to be stronger and tend to be embedded in more favorable dynamic and thermodynamic environments for development and intensification compared to high-skill ACs during low-skill periods. Hypothesis 3 also states that low-skill ACs during high-skill periods tend to be stronger and tend to be embedded in more favorable dynamic and thermodynamic environments for development and intensification compared to high-skill ACs during high-skill periods. Hypothesis 3 is addressed by comparing characteristics of low-skill ACs during low-skill periods with those of high-skill ACs during low-skill periods, and by comparing characteristics of low-skill ACs during high-skill periods with those of high-skill ACs during high-skill periods.

b. Data and methods

1) Identification of low-skill and high-skill periods

The 1° NOAA GEFS reforecast dataset version 2 (Hamill et al. 2013) is utilized to evaluate forecast skill of the synoptic-scale flow over the Arctic in order to identify low-skill and high-skill periods. The GEFS reforecast dataset version 2 is comprised of 11-member ensemble forecasts initialized daily at 0000 UTC for December 1984–present. A fixed model (i.e., the 2012 operational version of the NCEP GEFS) is used to produce the ensemble forecasts, such that forecast skill can be evaluated with the ensemble forecasts without having to account for changes in model configuration over time (e.g., Hamill and Kiladis 2014).

Forecasts of 500-hPa geopotential height initialized during the summers (June–August) of 2007–2017 are used to evaluate forecast skill of the synoptic-scale flow over the Arctic. The root mean square error (RMSE) of day-5 500-hPa geopotential height forecasts is first calculated at each grid point (k) over the Arctic (≥ 70°N) via

$$RMSE = \sqrt{\frac{1}{N}\sum_{n=1}^{N}[f_n(k) - O(k)]^2}\,, \tag{1}$$

where N denotes the number of ensemble members (i.e., 11), n denotes the nth ensemble member, f_n denotes the 500-hPa geopotential height from the nth ensemble member, and O denotes the 500-hPa geopotential height from ERA-Interim (Dee et al. 2011) at 1° horizontal resolution. After the RMSE is calculated at each grid point over the Arctic, the RMSE values are area-averaged over the Arctic (≥ 70°N) to obtain an area-averaged RMSE value. Standardized anomalies of area-averaged RMSE, hereafter referred to as σ_{RMSE}, relative to a 1985–2017 climatology of area-averaged RMSE are then calculated following the approach used by Moore [2017, section 5b(3)] to determine whether forecast skill is relatively low or high with respect to the baseline forecast skill of the GEFS reforecast dataset version 2.

Forecasts associated with the top and bottom 10% of σ_{RMSE} at day 5 are referred to as low-skill forecasts and high-skill forecasts, respectively. There are 101 low-skill forecasts and 101 high-skill forecasts. Time periods extending from day 0 through day 5 that are encompassed by low-skill forecasts and high-skill forecasts are referred to as low-skill periods and high-skill periods, respectively. There are instances in which a given low-skill period may overlap a given high-skill period when these periods occur in relatively short succession, resulting in some days occurring during both a low-skill period and a high-skill period, hereafter referred to as overlapping days. In order to avoid including an overlapping day in both a low-skill period and a high-skill period, the overlapping day is assigned to the period that occurs earlier. An overlapping day is assigned to the period that occurs earlier because low-skill and high-skill periods are determined based on forecast skill at day 5, with the overlapping days typically occurring closer to or on day 5 of the earlier period. There were 345 days and 297 days originally determined to occur during low-skill periods and high-skill periods, respectively. A total of 33 overlapping days were identified. Subsequently, 17 overlapping days were removed from low-skill periods, resulting in a total of 328 days during low-skill periods, and 16 overlapping days were removed from high-skill periods, resulting in a total of 281 days during high-skill periods (Table 2.1). The are a total of 1067 days in the 2007–2017 climatology (Table 2.1), which is the number of days encompassed by all forecasts initialized during the summers of 2007–2017 from day 0 through day 5, i.e., all days during 1 June–5 September of 2007–2017.

2) Identification of ACs

A cyclone climatology prepared by Sprenger et al. (2017) is used to identify ACs. Sprenger et al. (2017) use an objective SLP-based cyclone tracking algorithm developed by

Wernli and Schwierz (2006) to track cyclones globally every 6 h in the ERA-Interim dataset at 1° horizontal resolution. ACs in this dissertation are identified as cyclones that have a lifetime of ≥ 48 h and spend at least 6 h poleward of 70°N. The latitudinal requirement is the same as that used by Simmonds and Rudeva (2012, 2014) to identify ACs. All ACs that occur at any time during the climatology, low-skill periods, and high-skill periods are identified. There are 730 ACs during the climatology, 298 ACs during low-skill periods, and 208 ACs during high-skill periods (Table 2.1).

3) Characteristics of the Arctic environment and ACs

Selected dynamic and thermodynamic quantities are calculated to characterize the Arctic environment and ACs. The quantities are calculated using the ERA-Interim dataset at 1° horizontal resolution and will now be described. Synoptic-scale flow amplitude is measured in terms of the absolute value of the standardized anomaly of 500-hPa v wind, hereafter referred to as σ_{v500}. The strength of upper-tropospheric flow is measured in terms of 300-hPa wind speed. Lower-tropospheric baroclinicity is measured in terms of 850-hPa potential temperature (θ) gradient magnitude. Lower-to-midtropospheric baroclinic growth rate is measured in terms of the Eady growth rate (EGR) (e.g., Hoskins and Valdes 1990) calculated over the 850–600-hPa layer. EGR is calculated following Hoskins and Valdes (1990) via

$$\mathrm{EGR} = 0.31 \frac{\mathrm{f}}{\mathrm{N}} \left| \frac{\partial \mathbf{v}}{\partial \mathrm{z}} \right|, \tag{2}$$

where **v** is the horizontal vector wind, z is the geopotential height, f is the Coriolis parameter, and N is the Brunt–Väisälä frequency. The strength of upper-tropospheric divergence is measured in terms of positive values of 350–250-hPa divergence. The strength of upward lower-to-midtropospheric motion (ω) is measured in terms of negative values of 800–600-hPa ω.

Moisture transport throughout the troposphere is measured in terms of 1000–300-hPa integrated water vapor transport (IVT). Positive values of 1000–300-hPa integrated moisture flux convergence (IMFC) are used as a proxy for latent heating (e.g., Torn and Hakim 2015). IVT and IMFC were also calculated for the 1000–500-hPa layer, but the differences between the values of IVT and IMFC for the 1000–300-hPa layer that are shown in this chapter and the corresponding values of IVT and IMFC for the 1000–500-hPa layer (not shown) were found to be relatively small and inconsequential (not shown).

The aforementioned quantities are area-averaged over the Arctic (≥ 70°N) to characterize the Arctic environment. The aforementioned quantities are area-averaged within a 1000-km radius from the center of each AC to characterize the environment in the vicinity of each AC. The center of an AC is defined as the location of minimum SLP of the AC. The most extreme value of the area-averaged quantities, and the lowest SLP, for each AC during a period of interest (i.e., climatology, low-skill periods, or high-skill periods) when located in the Arctic during the period of interest are determined. The choice of a 1000-km radius is motivated by Yamagami et al. (2018b), who find that the mean radius of 10 extraordinary ACs is approximately 938 km, and Valkonen et al. (2021), who find that the median radii of ACs for the months of June–August of 1979–2015 are approximately 1000–1100 km.

4) Forecast skill of ACs

The GEFS reforecast dataset version 2 is utilized to examine the forecast skill of the intensity and position of the ACs identified in section 2b(2). The ACs identified in section 2b(2) are hereafter referred to as “analysis ACs” in this section. An approach used by Yamagami et al. (2019) to evaluate forecast skill of the intensity and position of ACs is adapted. Yamagami et al.

(2019) evaluate the forecast skill of the intensity and position of a given AC using the GEFS reforecast dataset version 2 at the 0000 UTC time of lowest SLP of the AC, i.e., the verification time, for forecast lead times of 1–7 days, every 1 day. Yamagami et al. (2019) choose a verification time that occurs at 0000 UTC because the GEFS reforecast dataset version 2 is only initialized at 0000 UTC. In this dissertation, the verification time for a given analysis AC during a period of interest (i.e., climatology, low-skill periods, or high-skill periods) is considered the 0000 UTC time of lowest SLP of the given analysis AC when located in the Arctic (> 70°N) during the period of interest. If there is no 0000 UTC time at which the given analysis AC is located in the Arctic during the period of interest, the time of lowest SLP of the given analysis AC when located in the Arctic during the period of interest is determined, and the surrounding 0000 UTC time at which the minimum SLP of the given analysis AC is lower and occurs during the period of interest is considered the verification time.

An objective SLP-based cyclone tracking algorithm developed by Crawford et al. (2021) is used to track cyclones in ensemble forecasts initialized 1–7 days, every 1 day, prior to the verification time of each analysis AC. A cyclone matching procedure developed by Korfe and Colle (2018) to match extratropical cyclone tracks in ERA-Interim with those in ensemble forecasts of various EPSs is adapted to match the analysis ACs with cyclones in the ensemble forecasts. The matching procedure determines which cyclone in an ensemble forecast exhibits the best temporal and spatial overlap with a given analysis AC based on a threshold value of "*T*" that will be discussed below. Cyclones are tracked in each ensemble forecast from forecast initialization to 192 h, every 6 h, over the Northern Hemisphere. Cyclones in ensemble forecasts that last ≥ 24 h are considered "candidate forecast cyclones" to match with the analysis ACs. For each candidate forecast cyclone, the percentage of 6-h time steps of the given analysis AC track

for which the center of the candidate forecast cyclone is ≤ 1200 km from, and closest to, the center of the given analysis AC is recorded. The candidate forecast cyclone corresponding to the percentage that is largest and ≥ *T*% is considered the "final candidate forecast cyclone." At least *T*% of the times in the final candidate forecast cyclone track must coincide with those of the given analysis AC track according to the following equation:

$$100 \times \left(\frac{2N_M}{N_A+N_F}\right) \geq T, \tag{3}$$

where N_A denotes the number of time steps in the given analysis AC track, N_F denotes the number of time steps in the final candidate forecast cyclone track, and N_M denotes the number of time steps in the final candidate forecast cyclone track that coincide in time with those of the given analysis AC track. If Eq. (3) is satisfied, the final candidate forecast cyclone is considered to be a "matching forecast AC."

Korfe and Colle (2018) use a *T* value of 60%. *T* values of 30–60%, every 10%, are tested in this dissertation. A *T* value of 60% is found to be too restrictive when evaluating all analysis ACs in the climatology, as a *T* value of 60% results in too few ensemble forecasts with a matching forecast AC (not shown). Increasing the *T* value may result in an increasing chance of a "miss" in which a given analysis AC is not matched with a candidate forecast cyclone that legitimately corresponds to the given analysis AC. Decreasing the *T* value may result in an increasing chance of a "false alarm" in which an analysis AC is matched with a candidate forecast cyclone that does not legitimately correspond to the given analysis AC. A *T* value of 40% is found to be optimal when considering forecasts for AC12 and AC16, and is thus used in this dissertation. It is noted that misses and false alarms can still occur when using a *T* value of 40%. To exemplify the impact of the *T* value on the number of matching forecast AC tracks, the matching forecast AC tracks for *T* values of 30–60%, every 10%, are shown for AC12 for the 5-

day lead time in Figs. 2.1a–d. The number of matching forecast AC tracks decreases from 10 to 4 as the *T* value is increased from 30% to 60% (Figs. 2.1a–d), indicating that the number of misses increases as the *T* value increases.

A minimum number of ensemble members with a matching forecast AC occurring at the verification time for a given analysis AC and a given forecast lead time is needed to evaluate the forecast skill of the given analysis AC for the given forecast lead time. The number of matching forecast ACs tends to decrease with increasing forecast lead time (e.g., Yamagami et al. 2019) as forecast uncertainty increases. Following Korfe and Colle (2018) and Froude (2010), this dissertation requires that ≥ 5 (out of 11) ensemble members have a matching forecast AC occurring at the verification time for a given analysis AC and a given forecast lead time. Forecast skill of the intensity of a given analysis AC for a given forecast lead time is determined by calculating the intensity RMSE via

$$RMSE = \sqrt{\frac{1}{N}\sum_{n=1}^{N}(f_n - O)^2}\,, \tag{4}$$

where N denotes the number of ensemble members with a matching forecast AC occurring at the verification time, n denotes the nth ensemble member, f_n denotes the minimum SLP of the matching forecast AC for the nth ensemble member at the verification time, and O denotes the minimum SLP of the given analysis AC at the verification time. Forecast skill of the position of a given analysis AC for a given forecast lead time is determined by calculating the position RMSE via Eq. (4), except that $f_n - O$ now represents the great circle distance between the center of the matching forecast AC for the nth ensemble member and the center of the given analysis AC.

For each forecast lead time, ACs during low-skill periods associated with the top and bottom 25% of intensity RMSE are referred to low-skill ACs during low-skill periods and high-skill ACs during low-skill periods, respectively. Also for each forecast lead time, ACs during

high-skill periods associated with the top and bottom 25% of intensity RMSE are referred to low-skill ACs during high-skill periods and high-skill ACs during high-skill periods, respectively. Corresponding sets of low-skill ACs and high-skill ACs based on the top and bottom 25% of position RMSE, respectively, during low-skill periods and high-skill periods are also identified.

5) Statistical significance testing

Bootstrap resampling with replacement tests are used to determine statistical significance of various quantities throughout this chapter. When testing for statistical significance of a quantity (e.g., lowest SLP) for a subgroup (e.g., ACs during low-skill periods) with respect to a corresponding climatological group (e.g., ACs during climatology) of which the subgroup is a part, the following procedure is used. A sample of values of the quantity equal in size to the number of values of the quantity in the subgroup is randomly selected from the climatological group, and the mean value of the quantity for the sample is calculated. This process is repeated 10000 times. If the mean value of the quantity for the subgroup is outside the 95% confidence interval of the distribution of mean values of the quantity for the 10000 samples, the mean value of the quantity for the subgroup is determined to be statistically significant.

When testing for statistical significance of differences of a quantity (e.g., lowest SLP) between two subgroups (e.g., low-skill ACs during low-skill periods and high-skill ACs during low-skill periods) within a common group (e.g., ACs during low-skill periods), the following approach is used. Two samples of values of the quantity are randomly selected from the common group, where the first sample is equal in size to the number of values of the quantity in the first subgroup and the second sample is equal in size to the number of values of the quantity in the

second subgroup. The difference between the mean values of the quantity for the two samples is calculated. This process is repeated 10000 times. If the difference between the mean values of the quantity for the two subgroups is outside the 95% confidence interval of the distribution of differences between mean values of the quantity for the 10000 sets of samples, the difference between the mean values of the quantity for the two subgroups is determined to be statistically significant.

c. Results

1) Arctic forecast skill and characteristics of the Arctic environment

Figures 2.2a and 2.2b show the evolution of area-averaged RMSE over the Arctic and σ_{RMSE}, respectively, for low-skill and high-skill forecasts during day 0–5.5, every 0.5 days. Area-averaged RMSE increases during day 0–5.5 for both low-skill forecasts and high-skill forecasts (Fig. 2.2a), but increases at a faster rate for low-skill forecasts compared to high-skill forecasts (Fig. 2.2a). In addition, area-averaged RMSE is statistically significantly high and low relative to climatology for low-skill forecasts and high-skill forecasts, respectively, for almost all of 0–5.5 (Fig. 2.2a). In regard to σ_{RMSE}, σ_{RMSE} increases and decreases throughout most of day 0–5.5 for low-skill forecasts and high-skill forecasts, respectively (Fig. 2.2b). In addition, σ_{RMSE} is statistically significantly high and low relative to climatology for almost all of day 0–5.5 for low-skill forecasts and high-skill forecasts, respectively (Fig. 2.2b). The increase and decrease in σ_{RMSE} throughout most of day 0–5.5 for low-skill forecasts and high-skill forecasts, respectively, indicates that forecast skill of the synoptic-scale flow over the Arctic becomes increasingly anomalously low and high relative to climatology throughout most of day 0–5.5 for low-skill forecasts and high-skill forecasts, respectively. The mean value of σ_{RMSE} for all forecasts in the

2007–2017 climatology is less than zero throughout day 0–5.5 (Fig. 2.2b), indicating that forecast skill of the synoptic-scale flow over the Arctic is higher during 2007–2017 relative to the entire 1985–2017 climatology.

Quantities characterizing the Arctic environment and calculated with the ERA-Interim dataset, as introduced in section 2b(3), are now examined at day 0–5.5, every 0.5 days, for the 101 low-skill forecasts and 101 high-skill forecasts. Only values of the quantities corresponding to days that occur during low-skill periods and high-skill periods are examined. There tends to be anomalously high-amplitude synoptic-scale flow (Fig. 2.3a), anomalously strong upper-tropospheric flow (Fig. 2.3b), anomalously large lower-tropospheric baroclinicity (Fig. 2.3c), and anomalously large lower-to-midtropospheric Eady growth rates (Fig. 2.3d) over the Arctic relative to climatology throughout low-skill periods. There tends to be anomalously low-amplitude synoptic-scale flow (Fig. 2.3a), anomalously weak upper-tropospheric flow (Fig. 2.3b), anomalously small lower-tropospheric baroclinicity (Fig. 2.3c), and anomalously small lower-to-midtropospheric Eady growth rates (Fig. 2.3d) over the Arctic relative to climatology throughout high-skill periods.

There tends to be anomalously strong upper-tropospheric divergence (Fig. 2.4a), anomalously strong lower-to-midtropospheric ascent (Fig. 2.4b), anomalously large moisture transport (Fig. 2.4c), and anomalously large latent heating (Fig. 2.4d) over the Arctic relative to climatology throughout low-skill periods. There tends to be anomalously weak upper-tropospheric divergence (Fig. 2.4a), anomalously weak lower-to-midtropospheric ascent (Fig. 2.4b), anomalously small moisture transport (Fig. 2.4c), and anomalously small latent heating (Fig. 2.4d) over the Arctic relative to climatology throughout high-skill periods.

The hypothesis (hypothesis 1) that the Arctic environment tends to be characterized by greater synoptic-scale flow amplitude, greater baroclinic growth rates, and greater latent heating during low-skill periods compared to high-skill periods is supported. The higher-amplitude synoptic-scale flow over the Arctic and stronger upper-tropospheric jet streaks that may be associated with the stronger upper-tropospheric flow over the Arctic during low-skill periods compared to high-skill periods likely support the stronger upper-tropospheric divergence and stronger lower-to-midtropospheric ascent over the Arctic during low-skill periods compared to high-skill periods. In addition, the higher amplitude synoptic-scale flow over the Arctic may support the greater moisture transport over the Arctic during low-skill periods compared to high-skill periods, which likely contributes to the greater latent heating over the Arctic during low-skill periods compared to high-skill periods. The stronger upper-tropospheric divergence and stronger lower-to-midtropospheric ascent over the Arctic during low-skill periods compared to high-skill periods may also be a signature of the greater latent heating over the Arctic during low-skill periods compared to high-skill periods.

It is hypothesized that greater lower-tropospheric baroclinicity, greater lower-to-midtropospheric Eady growth rates, and greater latent heating over the Arctic may be associated with greater forecast errors that may help explain the lower forecast skill of the synoptic-scale flow over the Arctic during low-skill periods compared to high-skill periods. In addition, greater lower-tropospheric baroclinicity, greater lower-to-midtropospheric Eady growth rates, and greater latent heating over the Arctic during low-skill periods compared to high-skill periods suggest that Arctic environmental conditions are more conducive to AC development and intensification during low-skill periods compared to high-skill periods. The suggested more conducive Arctic environmental conditions for AC development and intensification during low-

skill periods compared to high-skill periods may support more frequent occurrences of ACs and stronger ACs during low-skill periods compared to high-skill periods.

2) Frequency, location, and characteristics of ACs

As discussed in the previous section, it is anticipated that Arctic environmental conditions are more favorable for more frequent occurrences of ACs during low-skill periods compared to high-skill periods. Track frequencies of ACs during climatology, ACs during low-skill periods, and ACs during high-skill periods are shown in Figs. 2.5a–c, respectively (refer to Fig. 1.1 for map of Arctic geography). There are relatively high track frequencies of ACs during climatology (Fig. 2.5a), ACs during low-skill periods (Fig. 2.5b), and ACs during high-skill periods (Fig. 2.5c) across the Barents, Kara, and Laptev Seas, portions of the central Arctic Ocean, central portions of the northern Eurasian coast, and portions of the Canadian Archipelago. Crawford and Serreze (2016) and Fearon et al. (2021) similarly show relatively high frequencies of ACs across the Kara and Laptev Seas, the central Arctic Ocean, and central portions of the northern Eurasian coast. However, Crawford and Serreze (2016) and Fearon et al. (2021) also show relatively high frequencies of ACs across eastern Russia, which are not apparent in Figs. 2.5a–c. Differences in AC definitions between this dissertation, Crawford and Serreze (2016), and Fearon et al. (2021) may contribute to differences in AC track frequency across eastern Russia. As an example of the differences in AC definitions, ACs in this dissertation are required to spend at least 6 h poleward of 70°N, whereas Fearon et al. (2021) require ACs to be located poleward of 50°N, such that more ACs located equatorward of 70°N across eastern Russia would be identified by Fearon et al. (2021).

ACs during low-skill periods occur more frequently across much of the Arctic compared to ACs during climatology (compare Fig. 2.5a with Fig. 2.5b; Fig. 2.6a). ACs during high-skill periods occur less frequently across much of the Arctic compared to ACs during climatology (compare Fig. 2.5a with Fig. 2.5c; Fig. 2.6b). ACs during low-skill periods occur more frequently across much of the Arctic compared to ACs during high-skill periods (compare Fig. 2.5b with Fig. 2.5c; Fig. 2.6c), supporting the hypothesis (part of hypothesis 2) that ACs occur more frequently across the Arctic during low-skill periods compared to high-skill periods.

There tends to be lower 500-hPa geopotential height across much of the Arctic and higher 500-hPa geopotential height across much of the surrounding middle latitudes during low-skill periods compared to high-skill periods (Fig. 2.7a). The aforementioned 500-hPa geopotential height differences imply that there tends to be stronger 500-hPa geopotential height gradients and concomitantly greater lower-to-midtropospheric baroclinicity over the Arctic during low-skill periods compared to high-skill periods. The greater lower-to-midtropospheric baroclinicity over the Arctic during low-skill periods compared to high-skill periods corresponds to larger lower-to-midtropospheric Eady growth rates across much of the Arctic during low-skill periods compared to high-skill periods (Fig. 2.7b). In addition, there is larger moisture transport across much of the Arctic during low-skill periods compared to high-skill periods (Fig. 2.7c). The regions of larger lower-to-midtropospheric Eady growth rates (Fig. 2.7b) and larger moisture transport (Fig. 2.7c) during low-skill periods generally coincide with regions of higher track frequencies of ACs during low-skill periods (Fig. 2.6c), suggesting that the regions of larger lower-to-midtropospheric Eady growth rates and larger moisture transport support the regions of higher track frequencies of ACs during low-skill periods. Small regions of lower track frequencies of ACs during low-skill periods compared to ACs during high-skill periods over

portions of Baffin Bay, western Greenland, and the Norwegian Sea (Fig. 2.6c) may relate to the higher 500-hPa geopotential height over these regions during low-skill periods compared to high-skill periods (Fig. 2.7a).

The 500-hPa geopotential height differences between low-skill periods and high-skill periods in Fig. 2.7a may suggest that the AO index would tend to be more positive during low-skill periods compared to high-skill periods. A positive AO index is typically associated with anomalously low 500-hPa geopotential height over the Arctic (e.g., Thompson and Wallace 1998; Ogi et al. 2004; Serreze and Barrett 2008). In addition, Simmonds et al. (2008) find that the positive phase of the AO is associated with more frequent occurrences of ACs and stronger ACs during summer, as more frequent occurrences of ACs and stronger ACs may contribute to patterns of anomalously low SLP and 500-hPa geopotential height over the Arctic that correlate with a positive AO pattern. The higher track frequencies of ACs during low-skill periods compared to ACs during high-skill periods across the Arctic (Fig. 2.6c) may thus also suggest that the AO index would tend to be more positive during low-skill periods compared to high-skill periods. Therefore, it is hypothesized that the AO index tends to more often be positive during low-skill periods compared to high-skill periods.

The daily AO index (CPC 2021) throughout low-skill periods and high-skill periods is examined to address the aforementioned hypothesis. Figure 2.8 shows that there is large overlap in the distributions of AO index for low-skill periods and high-skill periods. Figure 2.8 further shows that the mean AO index throughout low-skill periods and high-skill periods is slightly negative and not statistically significantly different from that during climatology, although the mean AO index is slightly higher during low-skill periods (−0.17) compared to high-skill periods (−0.29). The mean change in AO index between day 0 and day 5 (day 5 minus day 0) is slightly

higher for low-skill periods (+0.19) compared to high-skill periods (+0.04), although there are no statistically significant differences in the change of AO index between low-skill periods and high-skill periods. The tendency for anomalously high-amplitude synoptic-scale flow over the Arctic during low-skill periods (Fig. 2.3a) may help explain why a positive AO index is not preferred during low-skill periods. Periods of anomalously high amplitude synoptic-scale flow over the Arctic during low-skill periods may be associated with relatively wavier synoptic-scale flow over the Arctic such that the AO index would tend to be more neutral or negative.

The quantities discussed in section 2b(3) and shown in Figs. 2.9a–d and Figs. 2.10a–d are used to examine characteristics of ACs during low-skill periods and ACs during high-skill periods. ACs during low-skill periods tend to be statistically significantly stronger compared to ACs during high-skill periods (Fig. 2.9a), supporting the hypothesis (part of hypothesis 2) that ACs tend to be stronger during low-skill periods compared to high-skill periods. In addition, ACs during high-skill periods tend to be statistically significantly weaker compared to ACs during climatology (Fig. 2.9a). ACs during low-skill periods tend to be embedded in regions characterized by statistically significantly higher-amplitude synoptic-scale flow (Fig. 2.9b), statistically significantly larger lower-tropospheric baroclinicity (Fig. 2.9c), and statistically significantly larger lower-to-midtropospheric Eady growth rates (Fig. 2.9d) compared to ACs during climatology and ACs during high-skill periods. In addition, ACs during high-skill periods tend to be embedded in regions characterized by statistically significantly lower-amplitude synoptic-scale flow (Fig. 2.9b), statistically significantly smaller lower-tropospheric baroclinicity (Fig. 2.9c), and statistically significantly smaller lower-to-midtropospheric Eady growth rates (Fig. 2.9d) compared to ACs during climatology.

ACs during low-skill periods also tend to be embedded in regions characterized by statistically significantly stronger upper-tropospheric divergence (Fig. 2.10a), statistically significantly stronger lower-to-midtropospheric ascent (Fig. 2.10b), statistically significantly larger moisture transport (Fig. 2.10c), and statistically significantly larger latent heating (Fig. 2.10d) compared to ACs during high-skill periods. In addition, ACs during high-skill periods tend to be embedded in regions characterized by statistically significantly weaker upper-tropospheric divergence (Fig. 2.10a), statistically significantly weaker lower-to-midtropospheric ascent (Fig. 2.10b), statistically significantly smaller moisture transport (Fig. 2.10c), and statistically significantly smaller latent heating (Fig. 2.10d) compared to ACs during climatology.

The hypothesis (part of hypothesis 2) that ACs tend to be embedded in more favorable dynamic and thermodynamic environments for development and intensification during low-skill periods compared to high-skill periods is supported. The more favorable dynamic and thermodynamic environments for development and intensification of ACs during low-skill periods compared to ACs during high-skill periods likely support the tendency for ACs during low-skill periods to be statistically significantly stronger compared to ACs during high-skill periods. It is hypothesized that the regions of greater lower-tropospheric baroclinicity, greater lower-to-midtropospheric Eady growth rates, and greater latent heating for ACs during low-skill periods compared to ACs during high-skill periods may be associated with greater forecast errors. The greater forecast errors may help explain the lower forecast skill of the synoptic-scale flow over the Arctic during low-skill periods as the ACs during low-skill periods interact with the synoptic-scale flow over the Arctic. The greater forecast errors also may help lead to lower forecast skill of ACs during low-skill periods compared to ACs during high-skill periods. The

forecast skill of ACs during low-skill periods and ACs during high-skill periods will next be examined to address the hypothesis (part of hypothesis 2) that ACs tend to be associated with lower forecast skill during low-skill periods compared to high-skill periods.

3) Forecast skill of ACs and a comparison between low-skill ACs and high-skill ACs

Forecast skill of the intensity and position of ACs during climatology, ACs during low-skill periods, and ACs during high-skill periods are examined for forecast lead times of 1–7 days, every 1 day, relative to the verification time of the ACs [see section 2b(4) for definition of the verification time]. Table 2.2 and Fig. 2.11 show the number and percentage, respectively, of ACs during climatology, ACs during low-skill periods, and ACs during high-skill periods for which forecast skill can be evaluated at each forecast lead time. As discussed in section 2b(4), forecast skill for a given AC and a given forecast lead time can be evaluated if there are ≥ 5 ensemble members with a matching forecast AC occurring at the verification time. The number (Table 2.2) and percentage (Fig. 2.11) of ACs during climatology, ACs during low-skill periods, and ACs during high-skill periods for which forecast skill can be evaluated increases slightly from the 1-day lead time to the 3-day lead time and decreases from the 3-day lead time to the 7-day lead time. The decrease from the 3-day lead time to the 7-day lead time is likely due to increasing forecast uncertainties associated with ACs as lead time increases (e.g., Yamagami et al. 2018b, 2019), such that there are fewer ensemble members with a matching forecast AC for a given AC at longer forecast lead times.

Intensity RMSE of ACs during climatology, ACs during low-skill periods, and ACs during high-skill periods tends to increase with increasing forecast lead time (Fig. 2.12a). For example, the mean intensity RMSE of ACs during climatology increases from approximately 2.3

hPa for the 1-day lead time to approximately 7.6 hPa for the 7-day lead time. The mean intensity RMSE for ACs during climatology is lower than the mean intensity error of the 26 extraordinary ACs shown by Yamgami et al. (2019) and discussed in section 1b(2)iii for all forecast lead times, which is likely due to the 26 extraordinary ACs collectively being more intense compared to the ACs during climatology. Yamagami et al. (2019) indicate that more intense extraordinary ACs tend to be associated with larger intensity errors. The mean intensity RMSE of ACs during low-skill periods tends to be slightly higher than the mean intensity RMSE of ACs during high-skill periods for forecast lead times of 2–5 days and 7 days (Fig. 2.12a), and statistically significantly higher than the mean intensity RMSE of ACs during high-skill periods for forecast lead times of 1 and 6 days (Fig. 2.12a).

Position RMSE of ACs during climatology, ACs during low-skill periods, and ACs during high-skill periods tends to increase with increasing forecast lead time (Fig. 2.12b). For example, the mean position RMSE of ACs during climatology increases from approximately 210 km for the 1-day lead time to approximately 817 km for the 7-day lead time. The mean position RMSE for ACs during climatology is generally comparable to the mean position error for the 26 extraordinary ACs shown by Yamgami et al. (2019) for all forecast lead times. There are no statistically significant differences in the mean values of position RMSE between ACs during low-skill periods and ACs during high-skill periods for all forecast lead times (Fig. 2.12b). The hypothesis (part of hypothesis 2) that ACs tend to be associated with lower forecast skill during low-skill periods compared to high skill periods is marginally supported in terms of intensity RMSE and is not supported in terms of position RMSE.

The following four “skill categories” of ACs are now examined: low-skill ACs during low-skill periods, high-skill ACs during low-skill periods, low-skill ACs during high-skill

periods, and high-skill ACs during high-skill periods. The focus is on the four skill categories of ACs that are determined based on intensity RMSE for the 5-day lead time following the approach discussed at the end of section 2b(4). The 5-day lead time is focused on for consistency with using the 5-day lead time to define forecast skill of the synoptic-scale flow over the Arctic. The results for the four skill categories of ACs determined based on position RMSE for the 5-day lead time will be briefly discussed at the end of this section. The results for the four skill categories of ACs determined based on intensity RMSE and position RMSE for other lead times will also be briefly discussed at the end of this section.

The quantities discussed in section 2b(3) and shown in Figs. 2.13a–d and Figs. 2.14a–d are used to examine the characteristics of the four skill categories of ACs determined based on intensity RMSE for the 5-day lead time. Low-skill ACs during low-skill periods tend to be statistically significantly stronger (Fig. 2.13a), and tend to be embedded in regions characterized by higher-amplitude synoptic-scale flow (Fig. 2.13b), larger lower-tropospheric baroclinicity (Fig. 2.13c), and larger lower-to-midtropospheric Eady growth rates (Fig. 2.13d) compared to high-skill ACs during low-skill periods. Low-skill ACs during high-skill periods tend to be stronger (Fig. 2.13a), and tend to be embedded in regions characterized by statistically significantly higher-amplitude synoptic-scale flow (Fig. 2.13b), larger lower-tropospheric baroclinicity (Fig. 2.13c), and statistically significantly larger lower-to-midtropospheric Eady growth rates (Fig. 2.13d) compared to high-skill ACs during high-skill periods.

The tendency for low-skill ACs during low-skill periods to be statistically significantly stronger than high-skill ACs during low-skill periods and the tendency for low-skill ACs during high-skill periods to be stronger than high-skill ACs during high-skill periods are consistent with the results of Yamagami et al. (2019) and Capute and Torn (2021), who both show that ACs with

lower forecast skill of intensity tend to be stronger. The tendency for low-skill ACs during low-skill periods to be embedded in regions characterized by larger lower-to-midtropospheric Eady growth rates compared to high-skill ACs during low-skill periods and the tendency for low-skill ACs during high-skill periods to be embedded in regions characterized by statistically significantly larger lower-to-midtropospheric Eady growth rates compared to high-skill ACs during high-skill periods are consistent with the findings of Capute and Torn (2021). Capute and Torn (2021) find that low-skill ACs are typically embedded in environments characterized by larger lower-to-midtropospheric Eady growth rates compared to high-skill ACs, when considering low-skill ACs and high-skill ACs determined based on forecast skill of intensity.

Low-skill ACs during low-skill periods tend to be embedded in regions characterized by statistically significantly stronger upper-tropospheric divergence (Fig. 2.14a), statistically significantly stronger lower-to-midtropospheric ascent (Fig. 2.14b), statistically significantly larger moisture transport (Fig. 2.14c), and statistically significantly larger latent heating (Fig. 2.14d) compared to high-skill ACs during low-skill periods. Low-skill ACs during high skill periods tend to be embedded in regions characterized by statistically significantly stronger upper-tropospheric divergence (Fig. 2.14a), stronger lower-to-midtropospheric ascent (Fig. 2.14b), larger moisture transport (Fig. 2.14c), and comparable latent heating (Fig. 2.14d) compared to high-skill ACs during high-skill periods. The tendency for low-skill ACs during high-skill periods and high-skill ACs during high-skill periods to be embedded in regions characterized by comparable latent heating is consistent with the findings of Capute and Torn (2021). Capute and Torn (2021) find that there is no systematic difference in latent heating between low-skill ACs and high-skill ACs, when considering low-skill ACs and high-skill ACs determined based on forecast skill of intensity. The tendency for low-skill ACs during low-skill periods to be

embedded in regions characterized by statistically significantly larger latent heating compared to high-skill ACs during low-skill periods is not consistent with the aforementioned finding from Capute and Torn (2021).

The hypothesis (part of hypothesis 3) that low-skill ACs during low-skill periods tend to be stronger and tend to be embedded in more favorable dynamic and thermodynamic environments for development and intensification compared to high-skill ACs during low-skill periods is supported. The hypothesis (part of hypothesis 3) that low-skill ACs during high-skill periods tend to be stronger and tend to be embedded in more favorable dynamic and thermodynamic environments for development and intensification compared to high-skill ACs during high-skill periods is supported, except when considering latent heating. In addition, low-skill ACs during low-skill periods tend to be embedded in the most favorable dynamic and thermodynamic environments for development and intensification when compared to all other skill categories of ACs (Figs. 2.13b–d and Figs. 2.14a–d), which likely contributes to low-skill ACs during low-skill periods tending to be the strongest ACs when compared to all other skill categories of ACs (Fig. 2.13a). Furthermore, the mean values of all quantities shown in Figs. 2.13a–d and Figs. 2.14a–d for low-skill ACs during low-skill periods are statistically significantly different from those of ACs during climatology.

Track densities of the four skill categories of ACs determined based on intensity RMSE for the 5-day lead time are now examined to identify where these ACs occur most frequently (refer to Fig. 1.1 for map of Arctic geography). Low-skill ACs during low-skill periods occur most frequently across the Barents and Kara Seas, and much of the central Arctic Ocean (Fig. 2.15a). High-skill ACs during low-skill periods occur most frequently across central portions of the northern Eurasian coast, portions of the Kara and Laptev Seas, and the Canadian Archipelago

(Fig. 2.15b). Low-skill ACs during high-skill periods occur most frequently across the Barents and Laptev Seas, and portions of the central Arctic Ocean (Fig. 2.15c). High-skill ACs during high-skill periods occur most frequently across central portions of the northern Eurasian coast, portions of the Kara and Laptev Seas, and portions of the Canadian Archipelago and adjacent Arctic Ocean and Baffin Bay (Fig. 2.15d).

There are higher track frequencies of low-skill ACs during low-skill periods compared to high-skill ACs during low-skill periods across much of the seas adjacent to the Eurasian coast and much of the Arctic Ocean (Fig. 2.16a). Similarly, there are higher track frequencies of low-skill ACs during high-skill periods compared to high-skill ACs during high-skill periods across much of the seas adjacent to the Eurasian coast and much of the Arctic Ocean (Fig. 2.16b). There are lower track frequencies of low-skill ACs during low-skill periods compared to high-skill ACs during low-skill periods across a region extending from the Canadian Archipelago to the Greenland Sea, and across portions of central Eurasia (Fig. 2.16a). Similarly, there are lower track frequencies of low-skill ACs during high-skill periods compared to high-skill ACs during high-skill periods across a region extending from the Canadian Archipelago to the Greenland Sea, and across portions of central Eurasia (Fig. 2.16b).

There generally tends to be larger lower-to-midtropospheric Eady growth rates and larger moisture transport over the Eurasian coast and adjacent seas compared to over the region extending from the Canadian Archipelago to the Greenland Sea during low-skill periods (Figs. 2.7b,c) and during high-skill periods (not shown). It is hypothesized that the larger lower-to-midtropospheric Eady growth rates and larger moisture transport over the Eurasian coast and adjacent seas may contribute to ACs with greater forecast errors in these regions, which may help explain the higher track frequencies of low-skill ACs during low-skill periods and low-skill

ACs during high-skill periods across much of the seas adjacent to the Eurasian coast. In addition, the higher track frequencies of low-skill ACs during low-skill periods and low-skill ACs during high-skill periods across much of the Arctic Ocean may relate to the tendency for low-skill ACs during low-skill periods and low-skill ACs during high-skill periods to be embedded in regions of higher-amplitude synoptic-scale flow (Fig. 2.13b). Regions of higher-amplitude synoptic-scale flow may tend to steer the low-skill ACs during low-skill periods and low-skill ACs during high-skill periods farther poleward across the Arctic Ocean.

When considering the four skill categories of ACs based on position RMSE for the 5-day lead time (not shown), there are no statistically significant differences in the quantities shown in Figs. 2.13a–d and Figs. 2.14a–d between low-skill ACs during low-skill periods and high-skill ACs during low-skill periods, and between low-skill ACs during high-skill periods and high-skill ACs during high-skill periods. Therefore, hypothesis 3 is not supported if considering forecast skill of position. The forecast skill of intensity of ACs is likely more sensitive to the favorability of the dynamic and thermodynamic environment for AC development and intensification compared to the forecast skill of position of ACs. Capute and Torn (2021) similarly indicate that low-skill ACs and high-skill ACs determined based on forecast skill of position are not associated with large differences in intensity or environmental characteristics. The same conclusions for hypothesis 3 are generally reached when considering the four skill categories of ACs determined based on intensity RMSE and position RMSE for all other lead times (not shown).

d. Summary

In this chapter, 2007–2017 climatologies of low-skill periods and high-skill periods, and 2007–2017 climatologies of ACs occurring during these respective periods, were constructed and examined. The climatologies of low-skill periods and high-skill periods served as a basis to address the hypothesis (hypothesis 1) that the Arctic environment tends to be characterized by greater synoptic-scale flow amplitude, greater baroclinic growth rates, and greater latent heating during low-skill periods compared to high-skill periods. The climatologies of ACs served as a basis to address the hypothesis (hypothesis 2) that ACs occur more frequently across the Arctic, tend to be stronger, tend to be embedded in more favorable dynamic and thermodynamic environments for development and intensification, and tend to be characterized by lower forecast skill during low-skill periods compared to high-skill periods. The forecast skill of ACs during low-skill periods and ACs during high-skill periods was evaluated in order to address hypothesis 3. Hypothesis 3 states that low-skill ACs during low-skill periods tend to be stronger and tend to be embedded in more favorable dynamic and thermodynamic environments for development and intensification compared to high-skill ACs during low-skill periods. Hypothesis 3 also states that low-skill ACs during high-skill periods tend to be stronger and tend to be embedded in more favorable dynamic and thermodynamic environments for development and intensification compared to high-skill ACs during high-skill periods. A summary of the most noteworthy findings is given below.

- The Arctic environment tends to be characterized by greater synoptic-scale flow amplitude, greater lower-tropospheric baroclinicity, greater lower-to-midtropospheric Eady growth rates, and greater latent heating during low-skill periods compared to high-skill periods (supporting hypothesis 1). The Arctic environment is thus likely more

conducive for AC development and intensification during low-skill periods compared to high-skill periods, which likely supports the more frequent occurrence of ACs across much of the Arctic during low-skill periods compared to high-skill periods (supporting part of hypothesis 2).

- The greater lower-tropospheric baroclinicity, greater lower-to-midtropospheric Eady growth rates, and greater latent heating over the Arctic during low-skill periods compared to high-skill periods likely contribute to the tendency for ACs during low-skill periods to be stronger and to be embedded in regions characterized by greater lower-tropospheric baroclinicity, greater lower-to-midtropospheric Eady growth rates, and greater latent heating compared to ACs during high-skill periods. Therefore, the hypothesis (part of hypothesis 2) that ACs tend to be stronger and tend to be embedded in more favorable dynamic and thermodynamic environments for development and intensification during low-skill periods compared to high-skill periods is supported.
- It is hypothesized that greater forecast errors that may be associated with the greater lower-tropospheric baroclinicity, greater lower-to-midtropospheric Eady growth rates, and greater latent heating over the Arctic during low-skill periods compared to high-skill periods may help explain the lower forecast skill of the synoptic-scale flow over the Arctic during low-skill periods compared to high-skill periods. It was hypothesized (part of hypothesis 2) that ACs tend to be characterized by lower forecast skill during low-skill periods compared to high-skill periods. The expectation was that greater forecast errors that may be associated with the greater lower-tropospheric baroclinicity, greater lower-to-midtropospheric Eady growth rates, and greater latent heating in the vicinity of ACs during low-skill periods may help lead to lower forecast skill of ACs during low-skill

periods. The aforementioned hypothesis is marginally supported in terms of forecast skill of intensity of ACs and is not supported in terms of forecast skill of position of ACs.

- A breakdown of ACs into four skill categories based on intensity RMSE for the 5-day lead time reveals that low-skill ACs during low-skill periods tend to be stronger and tend to be embedded in more favorable dynamic and thermodynamic environments for development and intensification compared to high-skill ACs during low-skill periods (supporting part of hypothesis 3). Similarly, low-skill ACs during high-skill periods tend to be stronger and tend to be embedded in more favorable dynamic and thermodynamic environments for development and intensification, except when considering latent heating, compared to high-skill ACs during high-skill periods (supporting part of hypothesis 3, with the exception of latent heating).
- Low-skill ACs during low-skill periods tend to be the strongest ACs and tend to be embedded in the most favorable dynamic and thermodynamic environments for development and intensification when compared to all other skill categories of ACs. It is hypothesized that relatively large forecast errors that may be associated with relatively large lower-tropospheric baroclinicity, relatively large lower-to-midtropospheric Eady growth rates, and relatively large latent heating in the vicinity of low-skill ACs during low-skill periods may help explain the low forecast skill of intensity of low-skill ACs during low-skill periods. The aforementioned relatively large forecast errors also may help explain the low forecast skill of the synoptic-scale flow over the Arctic as the low-skill ACs during low-skill periods interact with the synoptic-scale flow over the Arctic.

e. Tables

Table 2.1. Number of days and ACs during climatology, low-skill periods, and high-skill periods.

	Climatology	Low-skill periods	High-skill periods
Number of days	1067	328	281
Number of ACs	730	298	208

Table 2.2. Number of ACs during climatology, ACs during low-skill periods, and ACs during high-skill periods for which forecast skill can be evaluated at forecast lead times of 1–7 days, every 1 day.

	Forecast lead time (days)						
	1	2	3	4	5	6	7
Climatology	483	535	543	531	491	430	338
Low skill	193	219	226	220	204	168	140
High skill	134	149	154	142	138	132	99

f. Figures

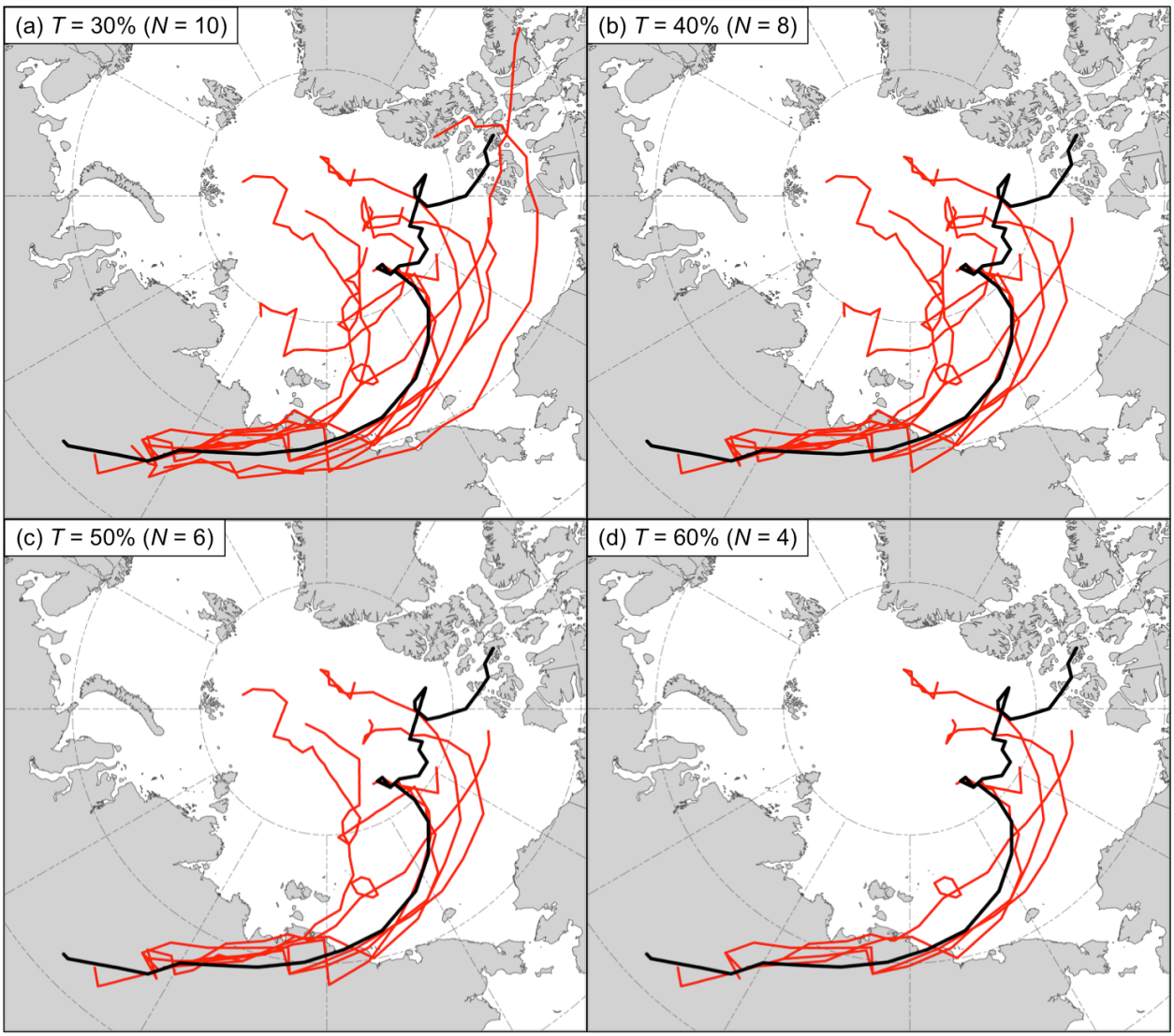

Fig. 2.1. Matching forecast AC tracks (red) corresponding to AC12 for the 5-day lead time when using a *T* value of (a) 30%, (b) 40%, (c) 50%, and (d) 60%. The black line shows the analysis track for AC12. "N" indicates the number of matching forecast AC tracks.

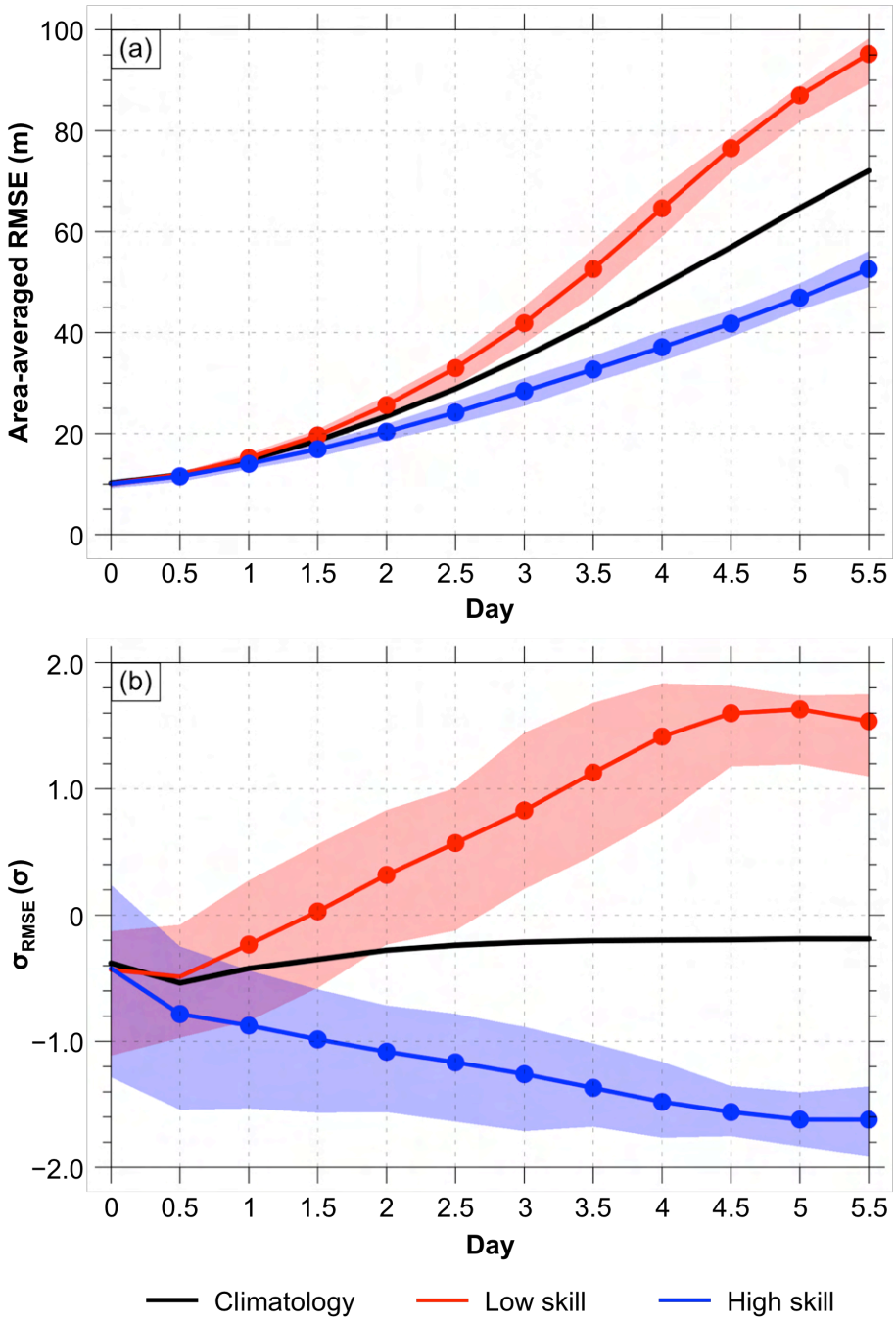

Fig. 2.2. Mean values of (a) area-averaged RMSE over the Arctic (m) and (b) σ_{RMSE} (σ) for low-skill forecasts (red line), high-skill forecasts (blue line), and all forecasts in the 2007–2017 climatology (black line) at days 0–5.5, every 0.5 days. Shading indicates the interquartile range (IQR) (25th–75th percentile values) of the quantities for low-skill forecasts (red) and high-skill forecasts (blue). Dots indicate statistical significance at the 95% confidence level of the mean values of the quantities for low-skill forecasts (red) and high-skill forecasts (blue) with respect to climatology.

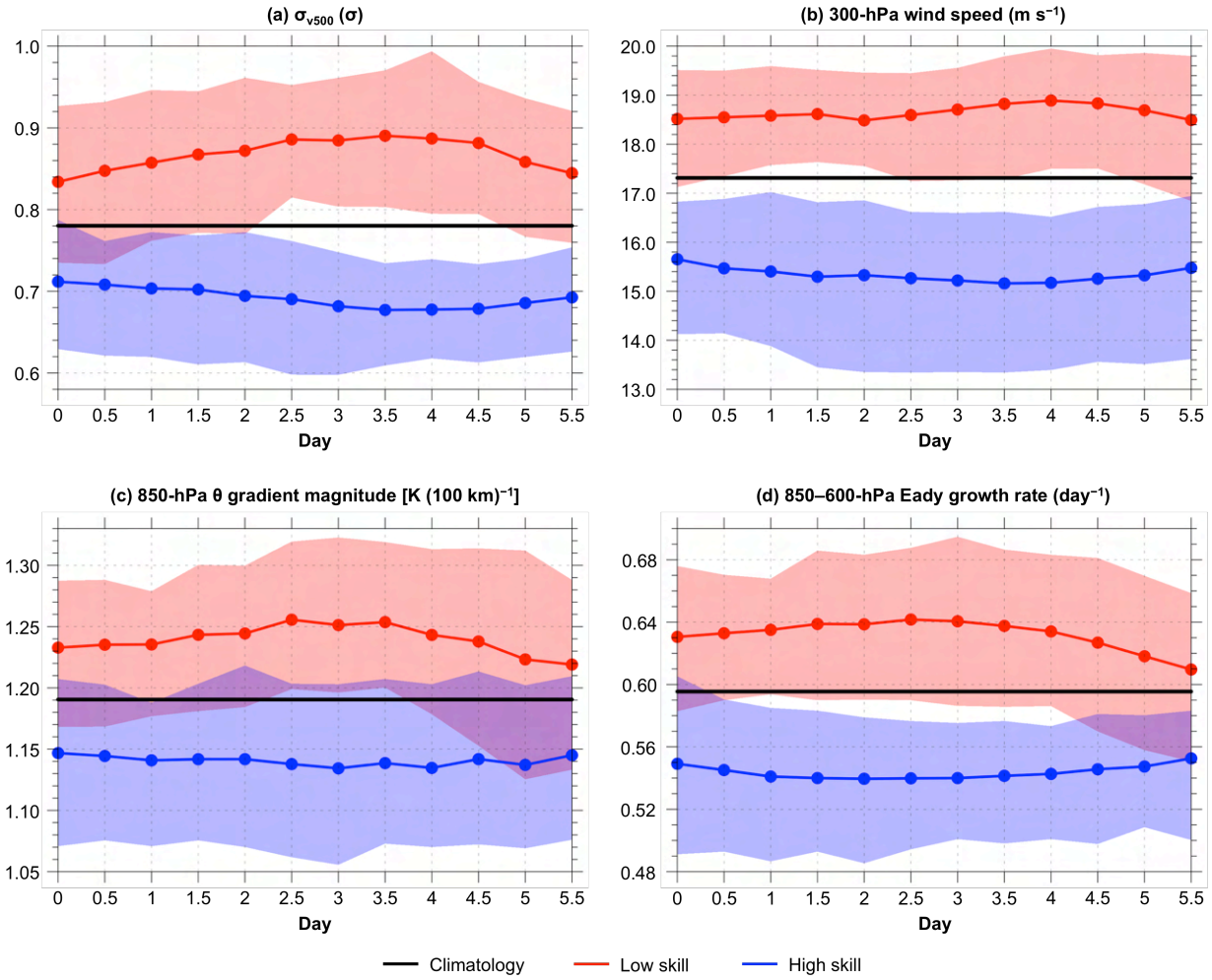

Fig. 2.3. Distributions of (a) area-averaged σ_{v500} (σ), (b) area-averaged 300-hPa wind speed (m s^{-1}), (c) area-averaged 850-hPa θ gradient magnitude [K (100 km)$^{-1}$], and (d) area-averaged 850–600-hPa Eady growth rate (day^{-1}) over the Arctic at days 0–5.5, every 0.5 days, for low-skill forecasts (red) and high-skill forecasts (blue), with solid lines indicating the mean values and shading indicating the IQR. Black lines indicate the mean values of the quantities across all times during the 2007–2017 climatology. Dots indicate statistical significance at the 95% confidence level of the mean values of the quantities for low-skill forecasts (red) and high-skill forecasts (blue) with respect to climatology.

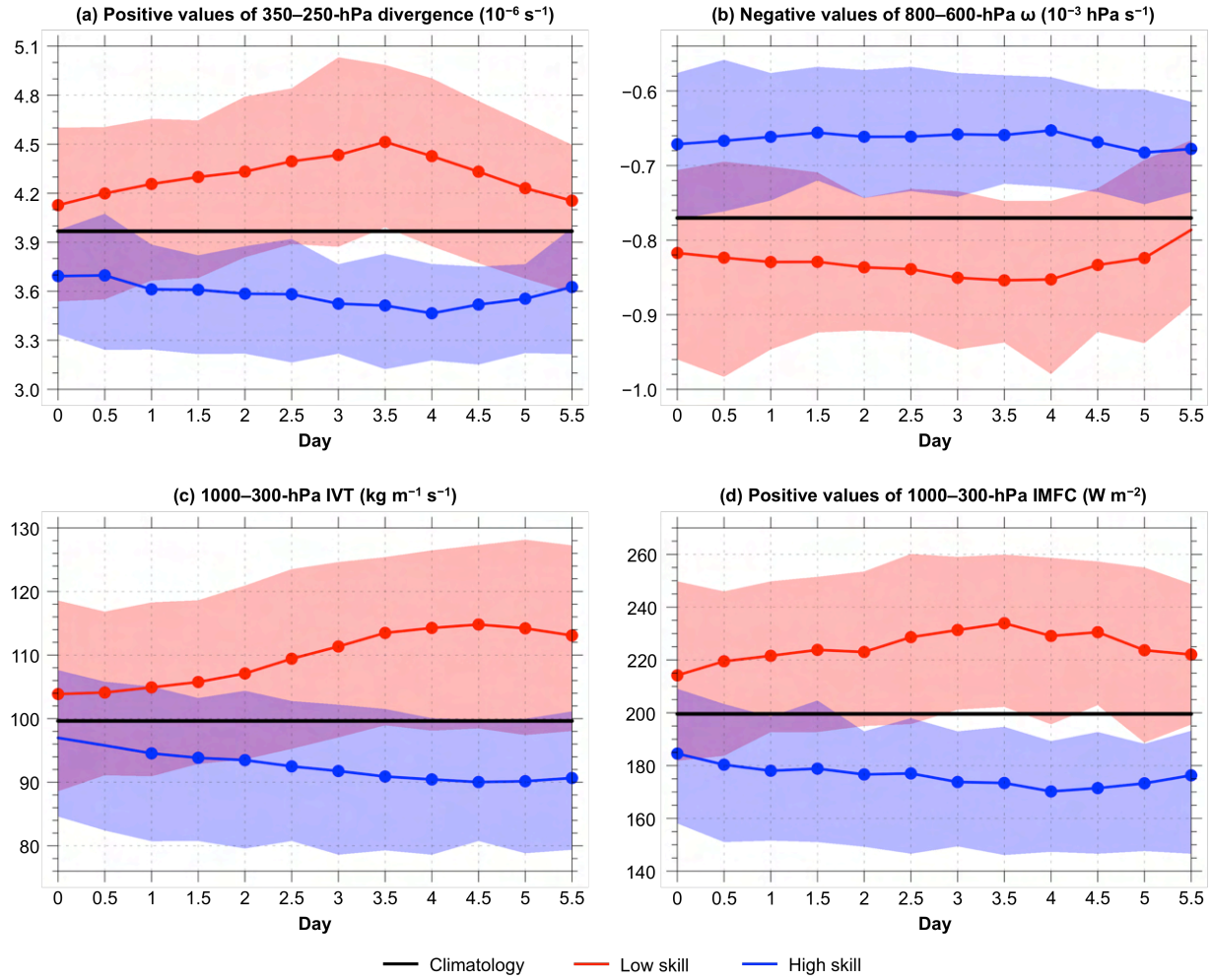

Fig. 2.4. As in Fig. 2.3, but for (a) area-averaged positive values of 350–250-hPa divergence (10^{-6} s^{-1}), (b) area-averaged negative values of 800–600-hPa ω (10^{-3} hPa s^{-1}), (c) area-averaged 1000–300-hPa IVT (kg m^{-1} s^{-1}), and (d) area-averaged positive values of 1000–300-hPa IMFC (W m^{-2}) over the Arctic.

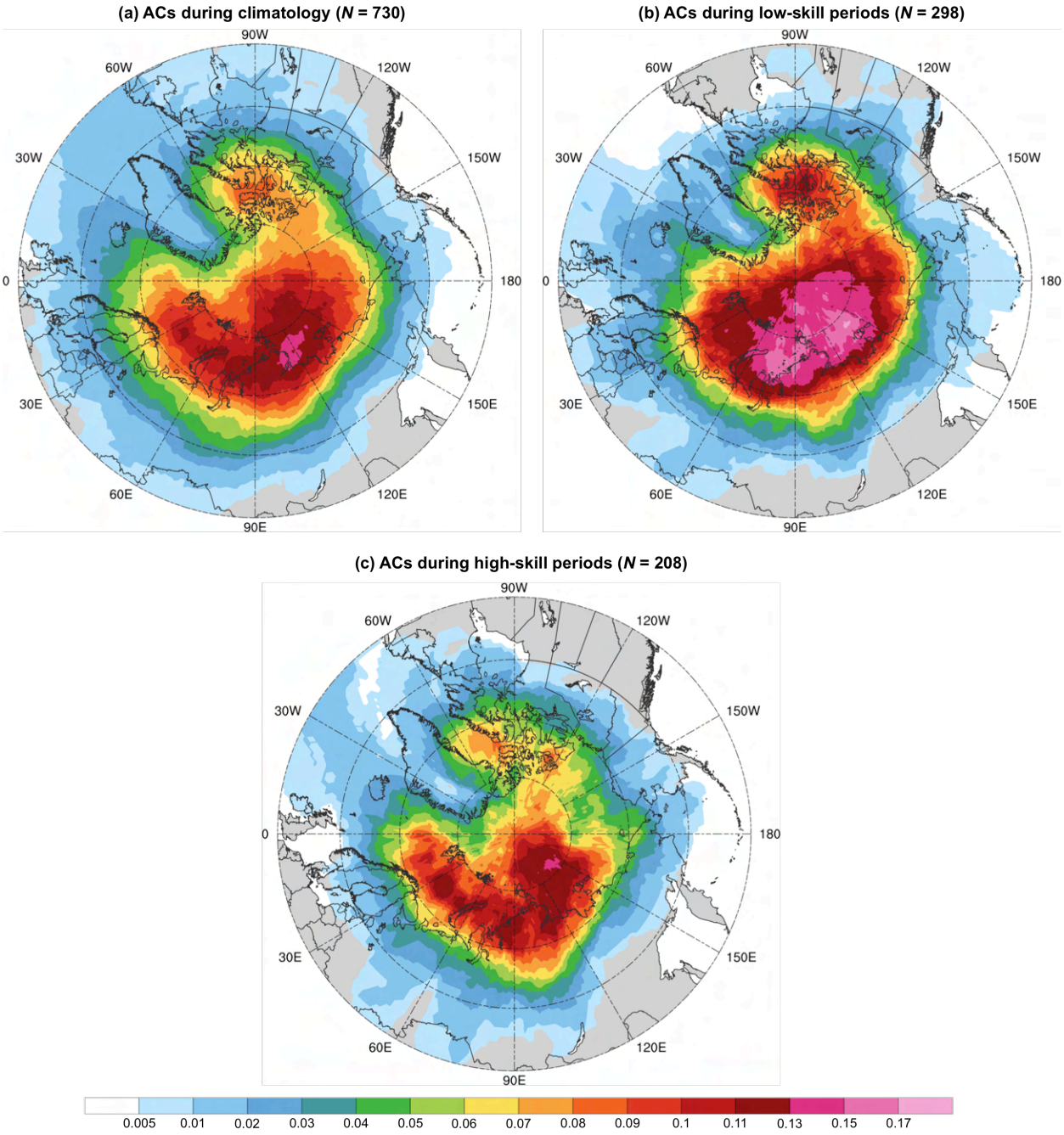

Fig. 2.5. Track frequency of (a) ACs during climatology, (b) ACs during low-skill periods, and (c) ACs during high-skill periods, shaded according to the number of the respective ACs for which a given grid point (using a 1° grid) is located within 500 km of the center of the respective ACs normalized by the number of days in the respective periods (given in Table 2.1). Units: number of ACs day^{-1}.

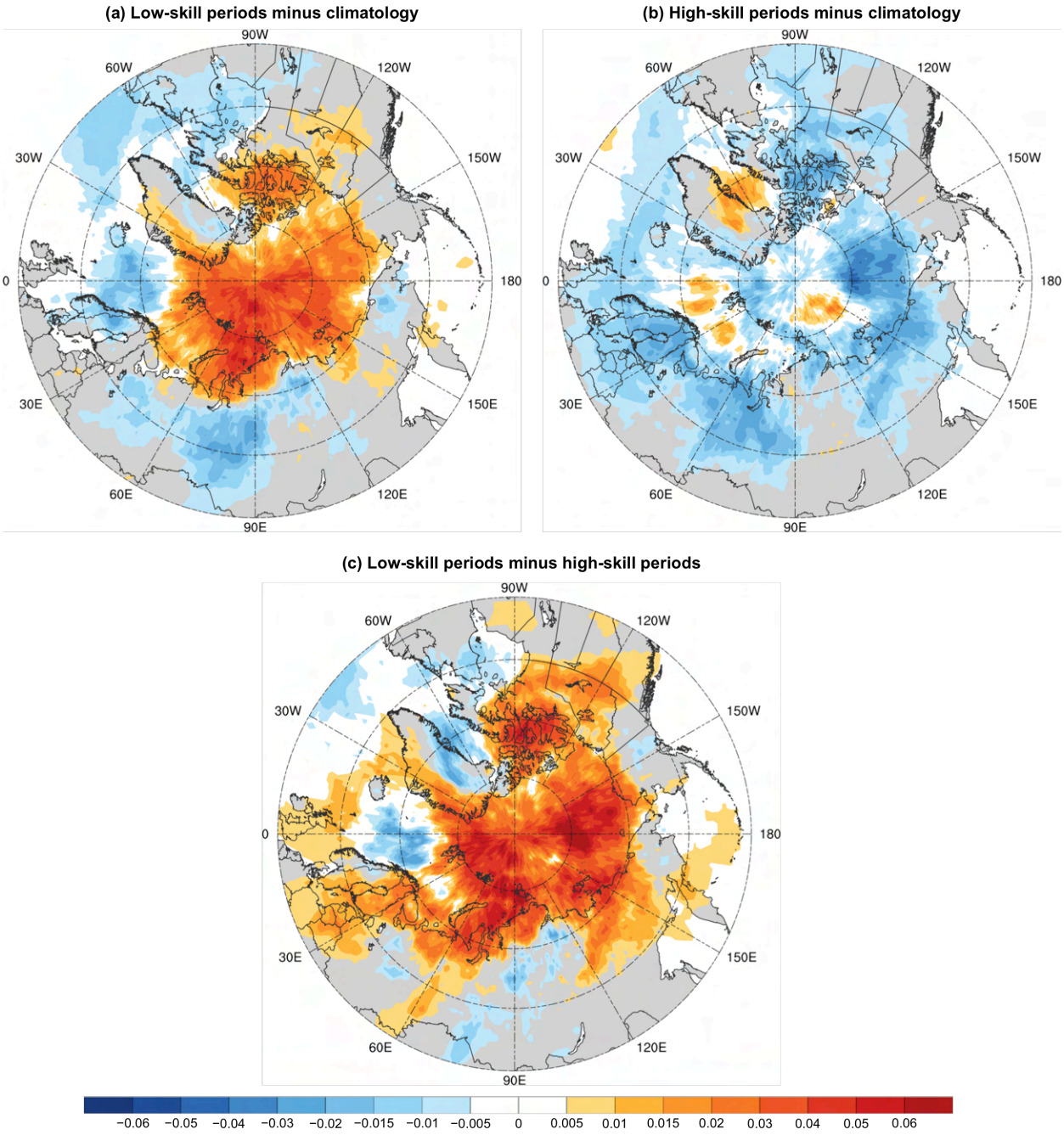

Fig. 2.6. Difference in track frequency between (a) ACs during low-skill periods and ACs during climatology (Fig. 2.5b minus Fig. 2.5a), (b) ACs during high-skill periods and ACs during climatology (Fig. 2.5c minus Fig. 2.5a), and (c) ACs during low-skill periods and ACs during high-skill periods (Fig. 2.5b minus Fig. 2.5c). Units: number of ACs day^{-1}.

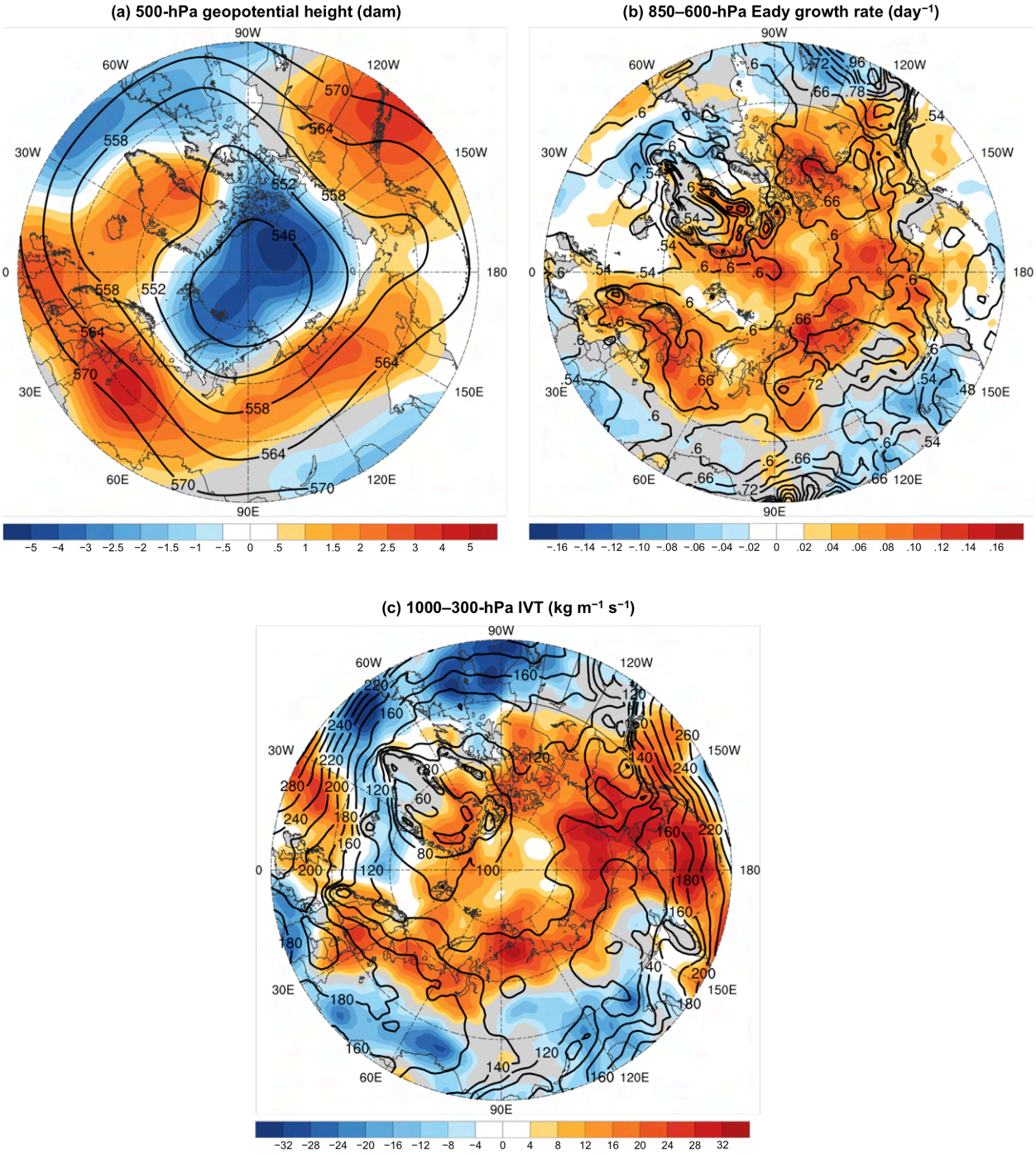

Fig. 2.7. (a) Mean 500-hPa geopotential height during low-skill periods (black contours, every 6 dam), (b) mean 850–600-hPa Eady growth rate during low-skill periods (black contours, every 0.06 day^{-1}), and (c) mean 1000–300-hPa IVT during low-skill periods (black contours, every 20 kg m^{-1} s^{-1}). Shading shows differences of (a) mean 500-hPa geopotential height (dam), (b) mean 850–600-hPa Eady growth rate (day^{-1}), and (c) mean 1000–300-hPa IVT (kg m^{-1} s^{-1}) between low-skill periods and high-skill periods (low-skill periods minus high-skill periods).

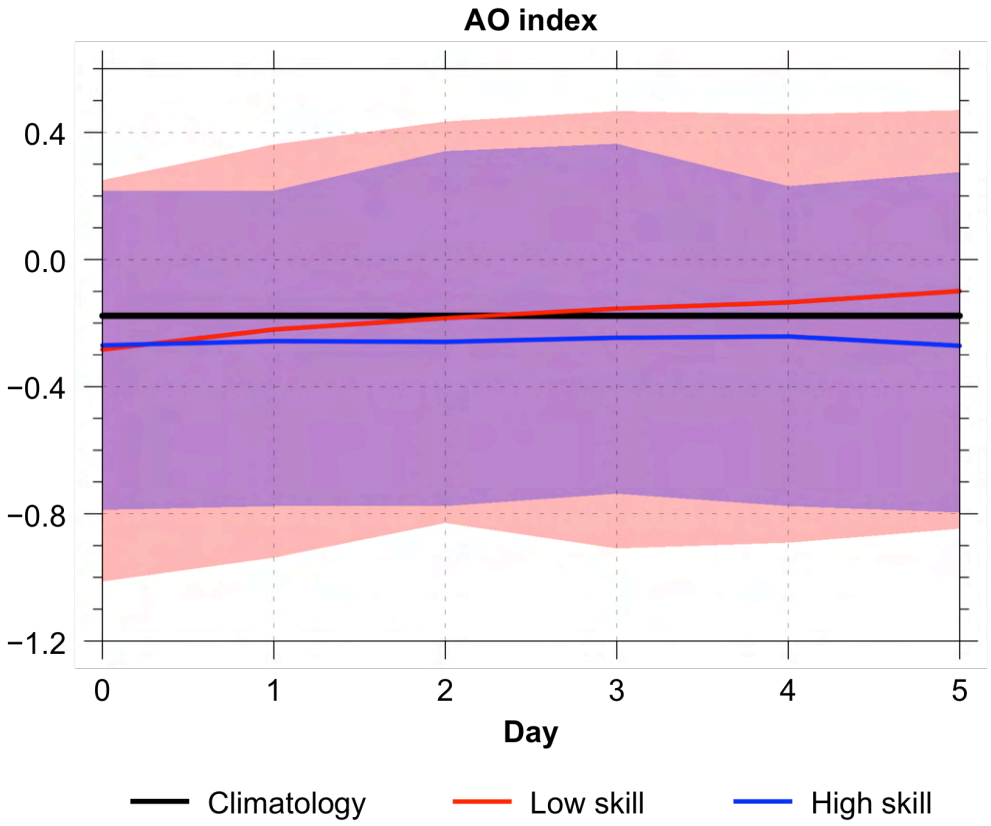

Fig. 2.8. Distributions of the AO index at days 0–5, every 1 day, for low-skill forecasts (red) and high-skill forecasts (blue), with solid lines indicating the mean values and shading indicating the IQR. Black line indicates the mean AO index across all days during the 2007–2017 climatology.

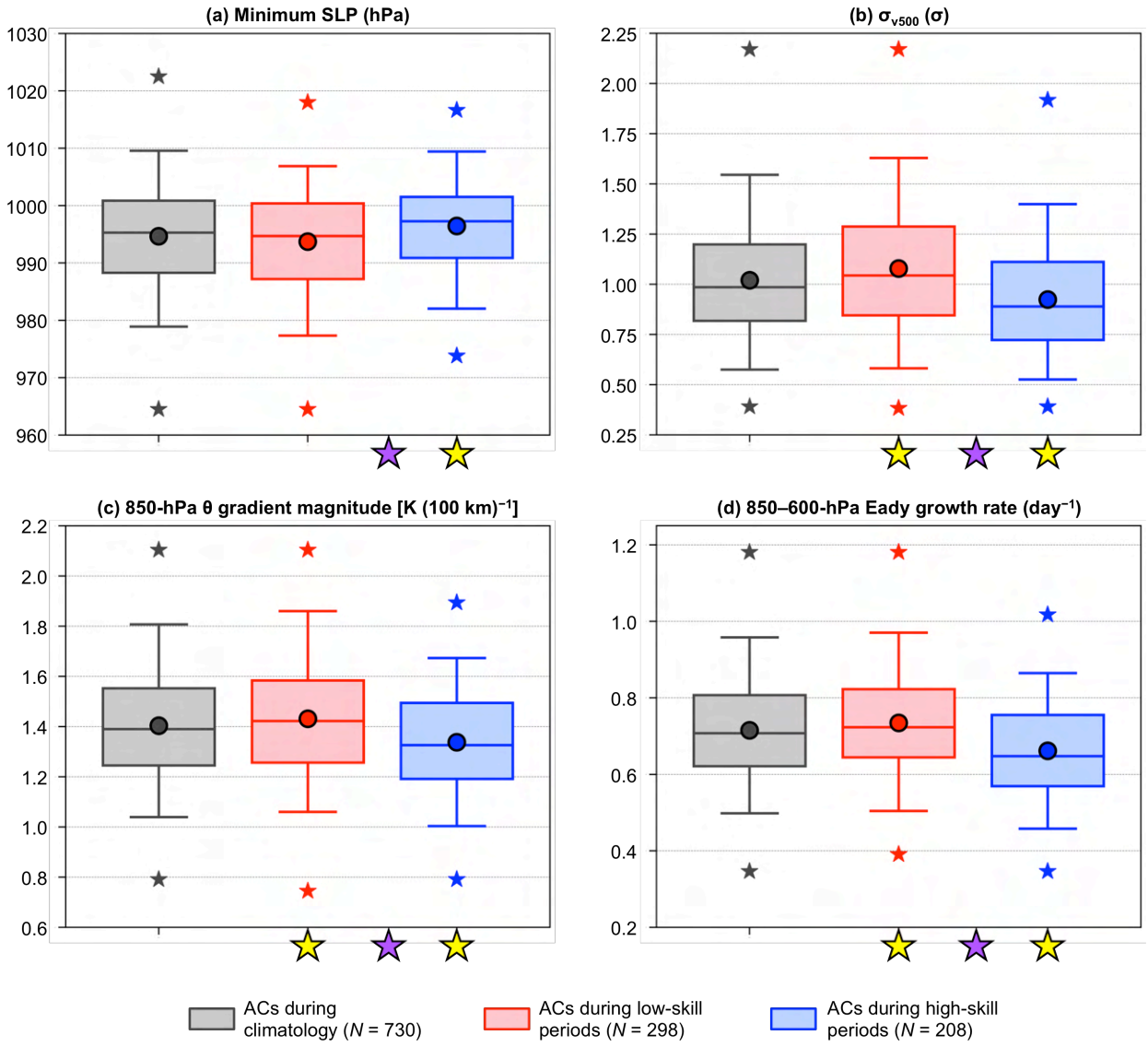

Fig. 2.9. Distributions of the most extreme value of quantities characterizing ACs during climatology (gray), ACs during low-skill periods (red), and ACs during high-skill periods (blue) when located in the Arctic during the respective periods. The selected quantities are (a) minimum SLP (hPa), (b) area-averaged σ_{v500} (σ), (c) area-averaged 850-hPa θ gradient magnitude [K (100 km)$^{-1}$], and (d) area-averaged 850–600-hPa Eady growth rate (day^{-1}). The quantities in (b)–(d) are area-averaged within a 1000-km radius from the centers of the ACs. Dots indicate the mean values, boxes indicate the IQR, and whiskers extend to the 5th and 95th percentiles. Gray, red, and blue stars indicate the minimum and maximum values of the distributions. Yellow stars indicate statistical significance at the 95% confidence level of the mean values of the quantities for ACs during low-skill periods and for ACs during high-skill periods with respect to the mean values of the quantities for ACs during climatology. Purple stars indicate statistical significance at the 95% confidence level between the mean values of the quantities for ACs during low-skill periods and the mean values of the quantities for ACs during high-skill periods.

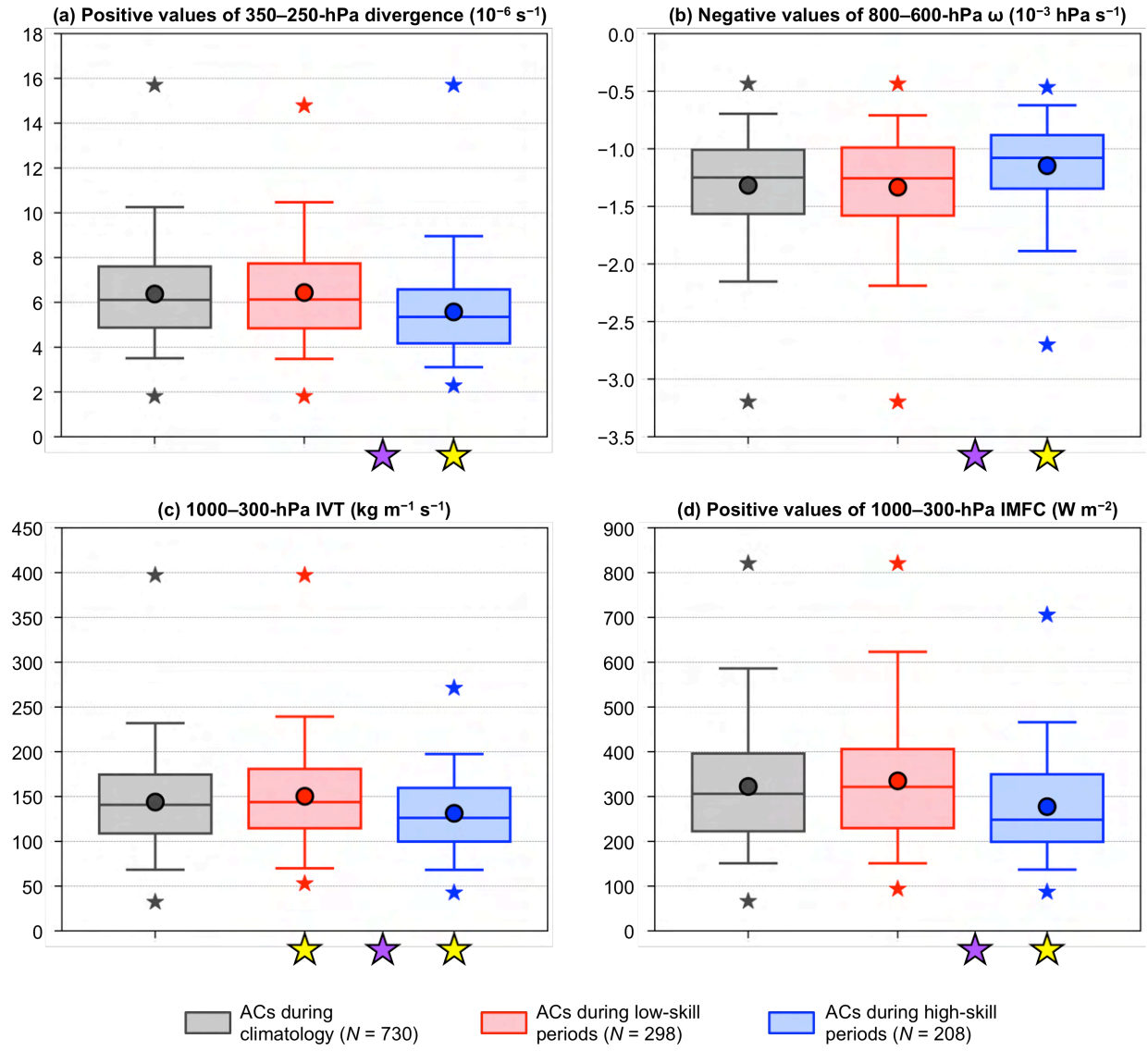

Fig. 2.10. As in Fig. 2.9, but for (a) area-averaged positive values of 350–250-hPa divergence (10^{-6} s^{-1}), (b) area-averaged negative values of 800–600-hPa ω (10^{-3} hPa s^{-1}), (c) area-averaged 1000–300-hPa IVT (kg m^{-1} s^{-1}), and (d) area-averaged positive values of 1000–300-hPa IMFC (W m^{-2}). The quantities in (a)–(d) are area-averaged within a 1000-km radius from the centers of the ACs.

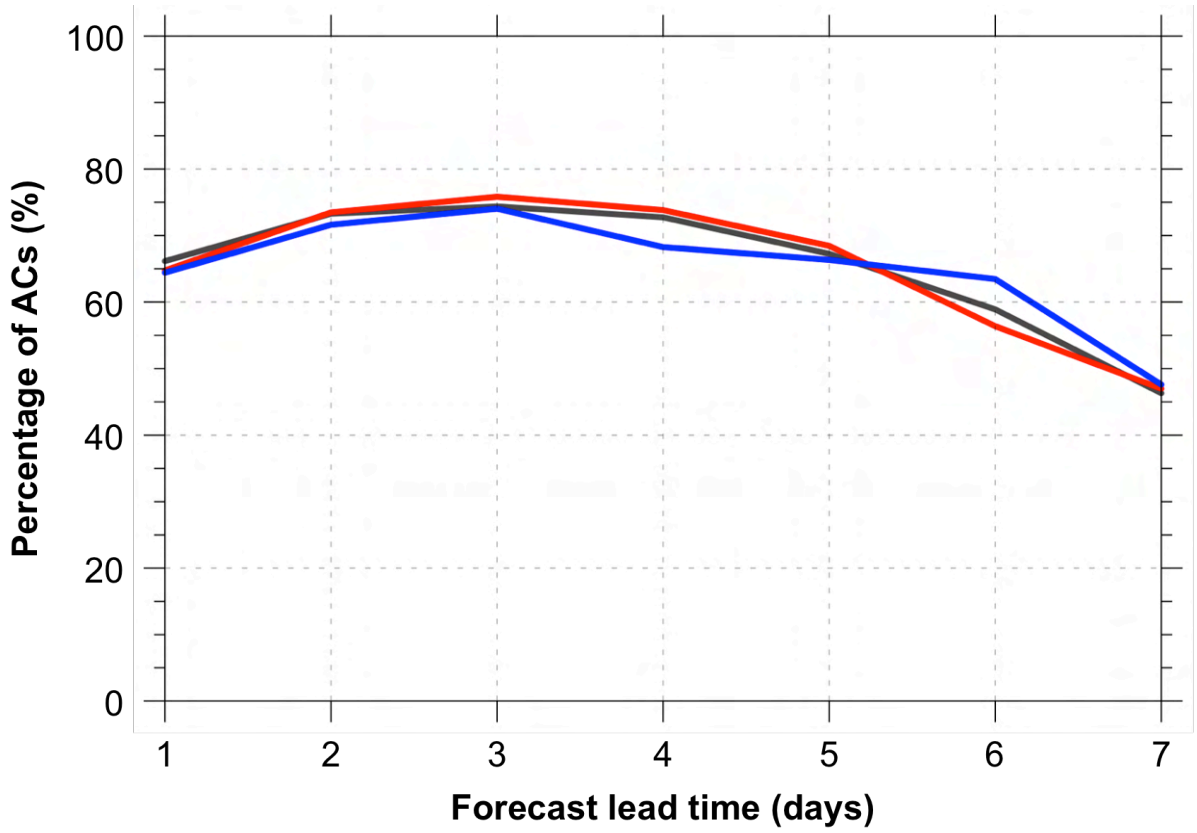

Fig. 2.11. Percentage of ACs during climatology (gray), ACs during low-skill periods (red), and ACs during high-skill periods (blue) for which forecast skill can be evaluated at forecast lead times of 1–7 days, every 1 day.

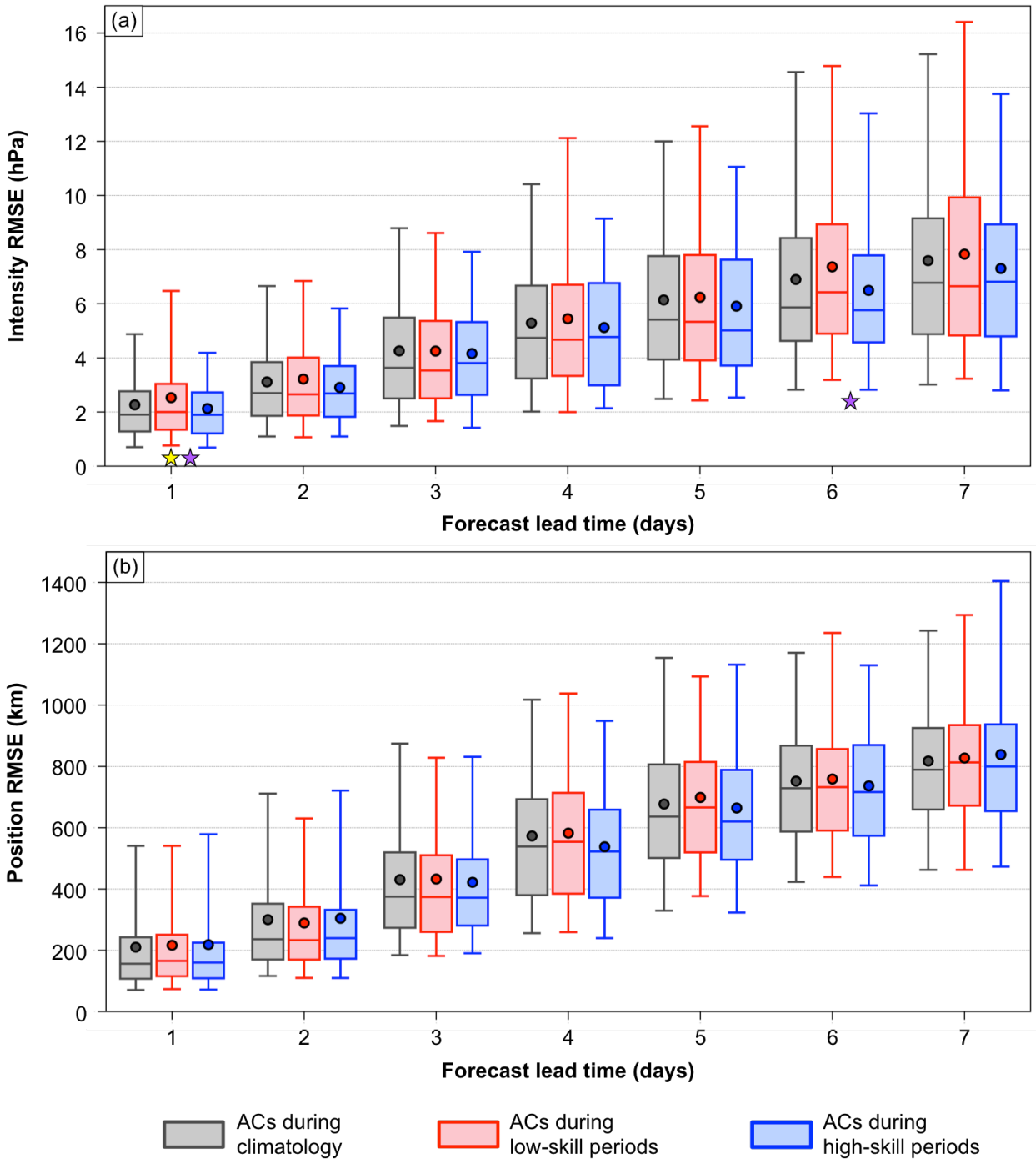

Fig. 2.12. Distributions of (a) intensity RMSE (hPa) and (b) position RMSE (km) of ACs during climatology (gray), ACs during low-skill periods (red), and ACs during high-skill periods (blue) for which forecast skill can be evaluated at forecast lead times of 1–7 days, every 1 day. The number of ACs for each forecast lead time are given in Table 2.2. Dots indicate the mean values, boxes indicate the IQR, and whiskers extend to the 5th and 95th percentiles. Yellow star indicates statistical significance at the 95% confidence level of the mean value of intensity RMSE for ACs during low-skill periods with respect to the mean value of intensity RMSE for

ACs during climatology for the 1-day lead time. Purple stars indicate statistical significance at the 95% confidence level between the mean value of intensity RMSE for ACs during low-skill periods and the mean value of intensity RMSE for ACs during high-skill periods for the 1-day and 6-day lead times.

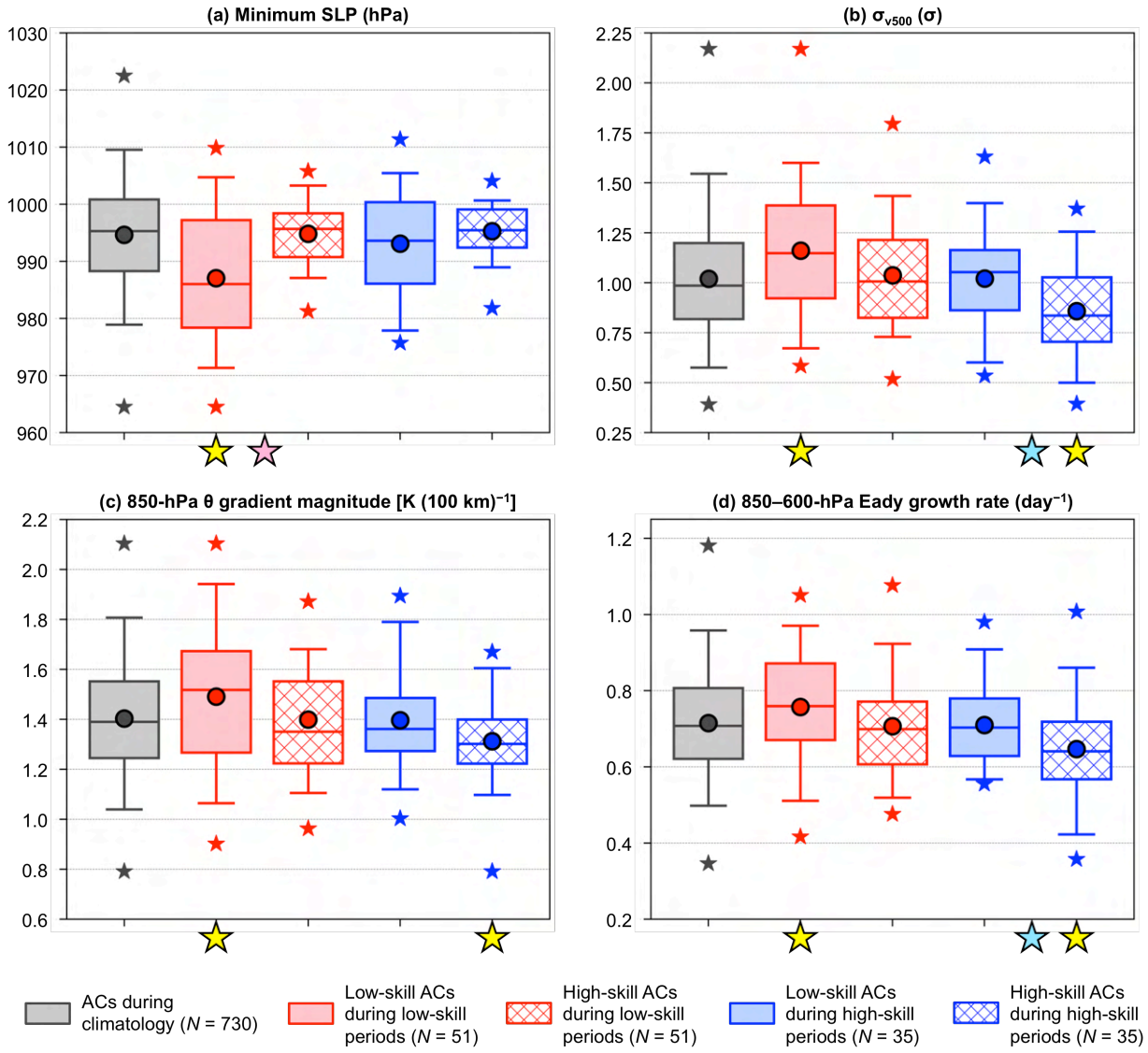

Fig. 2.13. Distributions of the most extreme value of quantities characterizing ACs during climatology (gray), low-skill ACs during low-skill periods (red solid), high-skill ACs during low-skill periods (red hatched), low-skill ACs during high-skill periods (blue solid), and high-skill ACs during high-skill periods (hatched blue) when located in the Arctic during the respective periods. The selected quantities are (a) minimum SLP (hPa), (b) area-averaged σ_{v500} (σ), (c) area-averaged 850-hPa θ gradient magnitude [K (100 km)$^{-1}$], and (d) area-averaged 850–600-hPa Eady growth rate (day^{-1}). The quantities in (b)–(d) are area-averaged within a 1000-km radius from the centers of the ACs. Dots indicate the mean values, boxes indicate the IQR, and whiskers extend to the 5th and 95th percentiles. Gray, red, and blue stars indicate the minimum and maximum values of the distributions. Yellow stars indicate statistical significance at the 95% confidence level of the mean values of the quantities for low-skill ACs during low-skill periods, high-skill ACs during low-skill periods, low-skill ACs during high-skill periods, and high-skill ACs during high-skill periods with respect to the mean values of the quantities for ACs during climatology. Pink stars indicate statistical significance at the 95% confidence level between the mean values of the quantities for low-skill ACs during low-skill periods and the mean values of

the quantities for high-skill ACs during low-skill periods. Light blue stars indicate statistical significance at the 95% confidence level between the mean values of the quantities for low-skill ACs during high-skill periods and the mean values of the quantities for high-skill ACs during high-skill periods.

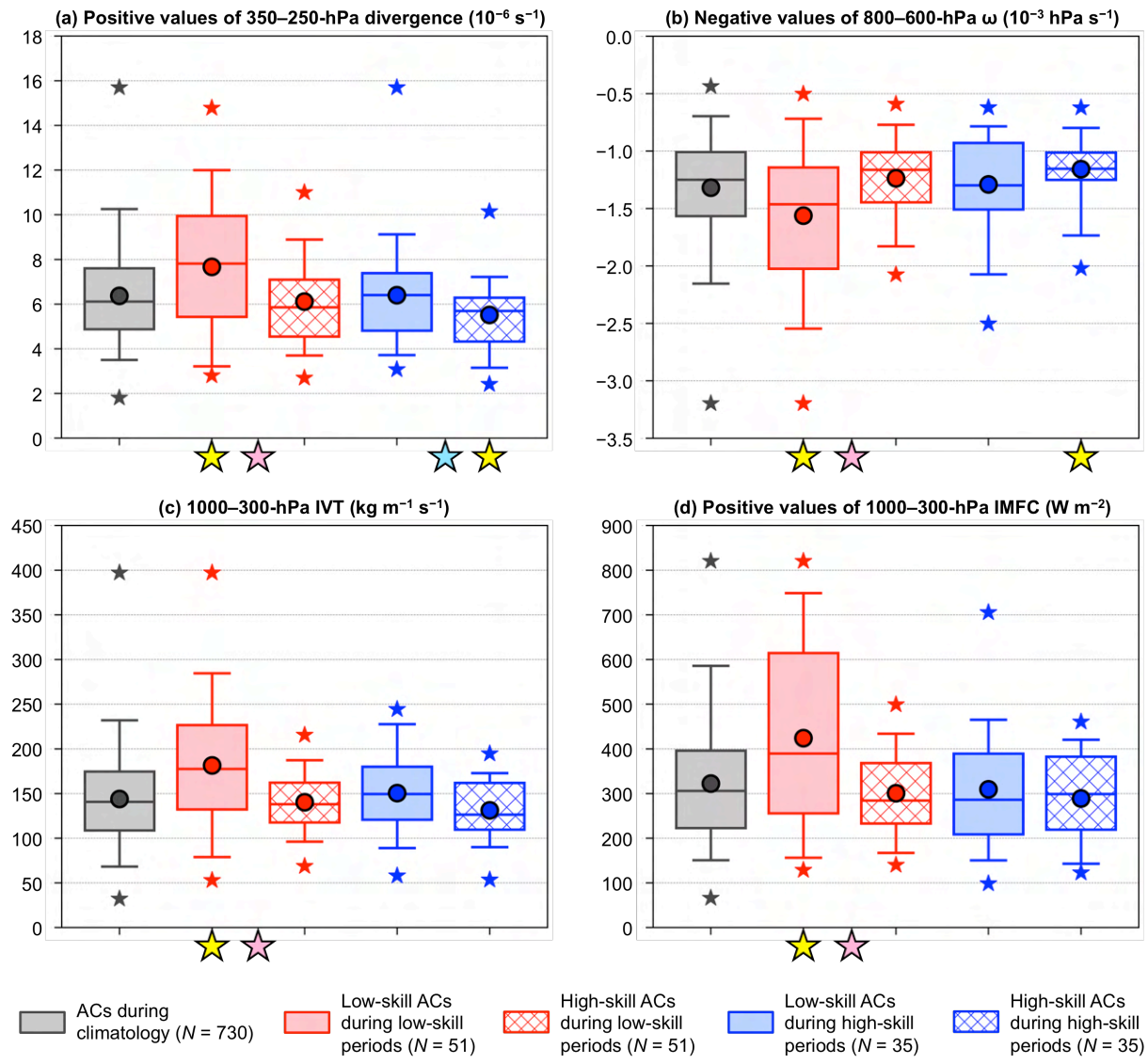

Fig. 2.14. As in Fig. 2.13, but for (a) area-averaged positive values of 350–250-hPa divergence (10^{-6} s^{-1}), (b) area-averaged negative values of 800–600-hPa ω (10^{-3} hPa s^{-1}), (c) area-averaged 1000–300-hPa IVT (kg m^{-1} s^{-1}), and (d) area-averaged positive values of 1000–300-hPa IMFC (W m^{-2}). The quantities in (a)–(d) are area-averaged within a 1000-km radius from the centers of the ACs.

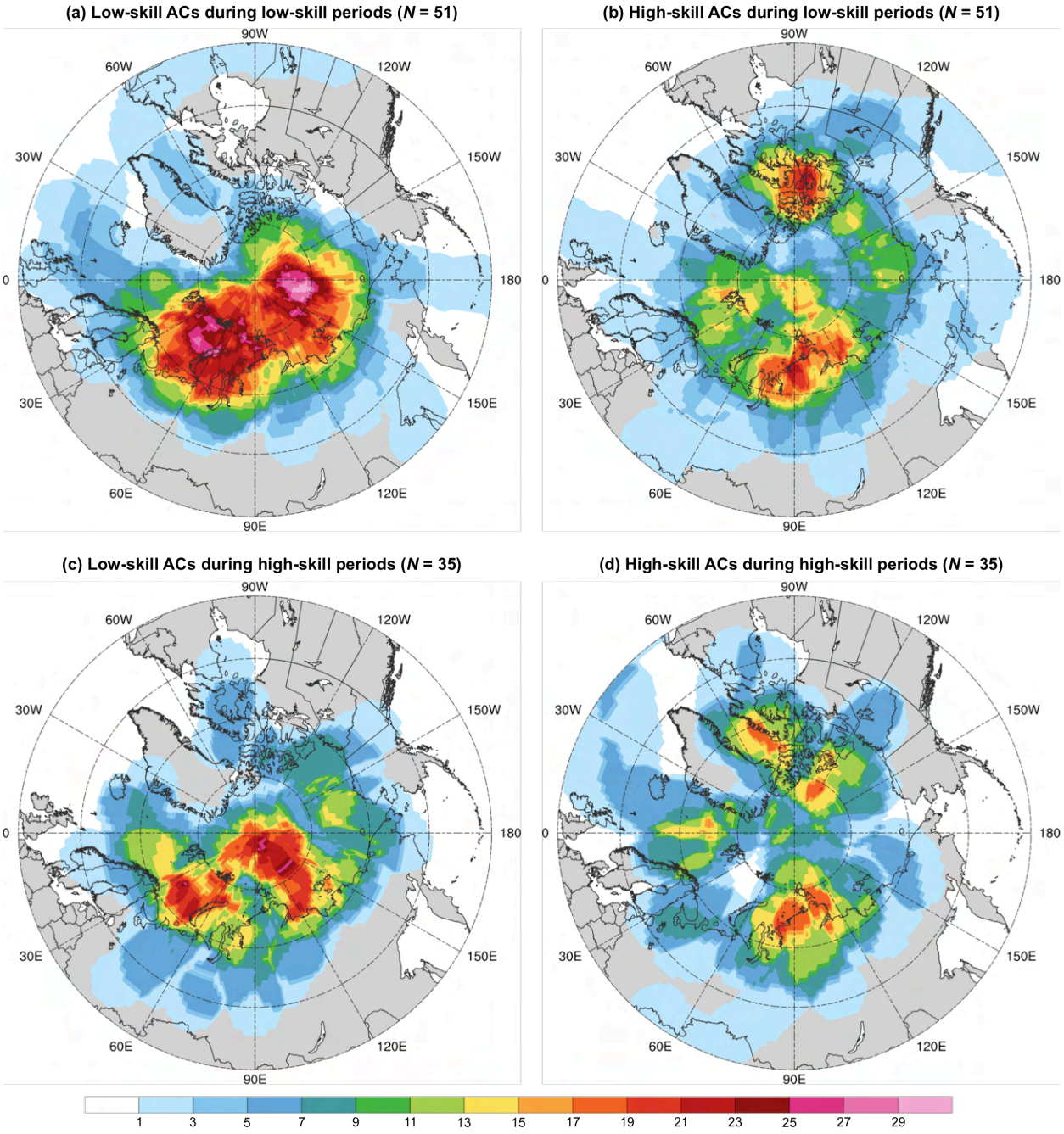

Fig. 2.15. Track density of (a) low-skill ACs during low-skill periods, (b) high-skill ACs during low-skill periods, (c) low-skill ACs during high-skill periods, and (d) high-skill ACs during high-skill periods, shaded according to the percentage of these respective ACs for which a given grid point (using a 1° grid) is located within 500 km of the center of these respective ACs.

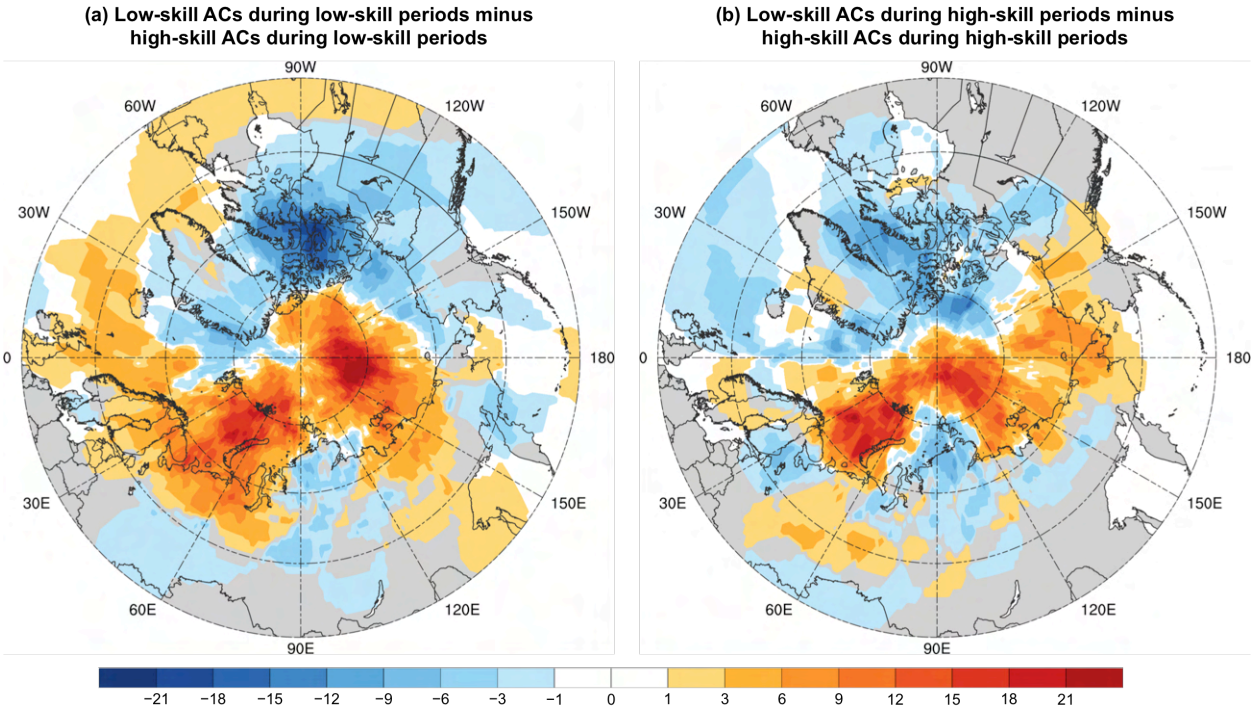

Fig. 2.16. Difference in track density between (a) low-skill ACs during low-skill periods and high-skill ACs during low-skill periods (Fig. 2.15a minus Fig. 2.15b), and (b) low-skill ACs during high-skill periods and high-skill ACs during high-skill periods (Fig. 2.15c minus Fig. 2.15d).

3. Features and processes influencing the evolution of strong low-skill ACs and strong high-skill ACs

a. Overview and objectives

In this chapter, hypothesis 4 is addressed. Hypothesis 4 states that TPVs, baroclinic zones, and WCBs, and TPV–AC interactions, baroclinic processes, and latent heating, influence the evolution of strong low-skill ACs during low-skill periods and strong high-skill ACs during low-skill periods. Hypothesis 4 further states that the aforementioned features and processes tend to be more robust for strong low-skill ACs during low-skill periods. Hypothesis 4 is addressed by constructing and comparing AC-centered composites for strong low-skill ACs during low-skill periods and strong high-skill ACs during low-skill periods, and by comparing characteristics of these respective categories of ACs.

b. Data and methods

The low-skill ACs during low-skill periods and high-skill ACs during low-skill periods that were identified based on intensity RMSE for the 5-day lead time and that were discussed in section 2c(3) are utilized. The top 25% strongest low-skill ACs during low-skill periods and top 25% strongest high-skill ACs during low-skill periods are identified based on the lowest SLP attained by these ACs when located in the Arctic (> 70°N) during low-skill periods. The top 25% strongest low-skill ACs during low-skill periods and top 25% strongest high-skill ACs during low-skill periods are hereafter referred to as strong low-skill ACs and strong high-skill ACs, respectively. The tracks of the strong low-skill ACs and strong high-skill ACs are based on 6-h SLP data from the ERA-Interim at 1° horizontal resolution, as discussed in section 2b(2). The strong low-skill ACs and strong high-skill ACs are now tracked using the higher-resolution

ERA5 dataset (Hersbach et al. 2020) at 0.25° horizontal resolution every 6 h. To track each AC in ERA5, the location of minimum SLP within a 200-km radius of each track point of the corresponding ERA-Interim track is identified in ERA5. The resulting ERA5 track for each AC is then manually analyzed to ensure it properly follows the location of minimum SLP of the AC. Also, if an AC is manually determined to undergo cyclogenesis earlier and/or cyclolysis later in ERA5, additional track points are added to the corresponding ERA5 track.

Features and processes influencing the evolution of the strong low-skill ACs and the strong high-skill ACs are examined by constructing AC-centered composites for these ACs at various lag times relative to the time of lowest SLP of these ACs when located in the Arctic (t_{low}). Lag times of t_{low}−48 h to t_{low}+12 h, every 12 h, are focused on to examine the evolution of the strong low-skill ACs and strong high-skill ACs when these ACs intensify and reach peak intensity. For each lag time and category of ACs, the mean latitude and mean longitude of the ACs are determined. ERA5 grids of selected dynamic and thermodynamic quantities at 0.25° horizontal resolution are shifted and rotated such that the center of each AC (i.e., location of minimum SLP) is positioned at the mean latitude and mean longitude of the ACs.

Since ERA5 data are on latitude–longitude grids, the area of grid cells over the Arctic varies. In order to shift ERA5 grids while preserving area, each ERA5 grid is projected onto a 25-km polar Equal-Area Scalable Earth 2.0 (EASE2) grid (Brodzik et al. 2012) by utilizing a portion of the cyclone tracking algorithm developed by Crawford et al. (2021) that projects latitude–longitude grids onto EASE2 grids. The EASE2 grid uses a polar Lambert azimuthal equal-area projection centered at 90°N, 0°E (Brodzik et al. 2012). Each ERA5 latitude–longitude grid is first rotated such that the AC center is located at 0°E, which lies along the y-axis of the EASE2 grid, before being projected onto the EASE2 grid. Doing this rotation allows both the

AC center and North Pole to lie along the y-axis of the EASE2 grid such that the y-axis corresponds to the meridional direction with respect to the AC center. Each EASE2 grid is then shifted north or south along the y-axis, such that the AC center is located at the grid point closest to the mean latitude of the ACs. Each shifted EASE2 grid is then projected back onto a 0.25° latitude–longitude grid and lastly rotated such that the AC center is located at the mean longitude of the ACs. The resulting grids are then composited for each lag time and category of ACs. Throughout this chapter, geography will be shown on composite maps for reference. Since the ACs in each category of ACs form over various locations, the geography is not representative of all ACs in each category of ACs. The influence of land–sea boundaries, ice–sea boundaries, and topographic features on the evolution of the ACs for each category of ACs will thus not be discussed, given that the locations of these boundaries and topographic features vary among the ACs.

Selected dynamic and thermodynamic quantities that are representative of features and processes influencing the evolution of the strong low-skill ACs and the strong high-skill ACs are area-averaged within a 1000-km radius from the centers of the individual ACs of these respective categories of ACs at each lag time. Area-averaging the selected quantities as described allows for the selected quantities to be compared between the strong low-skill ACs and the strong high-skill ACs without having to account for the impact of composite smoothing on the values of the selected quantities. The choice of a 1000-km radius is based on the discussion in section 2b(3) for examining characteristics of ACs in chapter 2.

c. Results

1) AC-centered composites for strong low-skill ACs

Table 3.1 shows that all 13 strong low-skill ACs attain a lowest SLP in the range of 962–979 hPa when located in the Arctic. Two notable strong low-skill ACs are AC12, which occurred during 2–12 August 2012 and attained a lowest SLP of 962.5 hPa when located in the Arctic (Table 3.1), and AC16, which occurred during 13–19 August 2016 and attained a lowest SLP of 968.3 hPa when located in the Arctic (Table 3.1). The majority of the strong low-skill ACs track east-northeastward while intensifying over the seas adjacent to Eurasia or over the central Arctic Ocean (Fig. 3.1a). The strong low-skill ACs intensify at varying rates between t_{low}−48 h and t_{low}, with the mean minimum SLP decreasing from 993.8 hPa at t_{low}−48 h to 970.6 hPa at t_{low} (Fig. 3.1b). The strong low-skill ACs generally weaken between t_{low} and t_{low}+36 h at rates that are smaller in magnitude compared to the rates at which the strong low-skill ACs intensify between t_{low}−48 h and t_{low} (Fig. 3.1b).

The role of baroclinic processes in the evolution of the strong low-skill ACs is first examined. Figure 3.2a shows that at t_{low}−48 h, the composite AC is located in a region of strong lower-to-midtropospheric baroclinicity, near the crest of a thickness ridge and downstream of a thickness trough. Corresponding to the region of strong lower-to-midtropospheric baroclinicity are dual upper-tropospheric jet streaks, which include a southern jet streak positioned southwest of the composite AC near the base of the thickness trough and a northern jet streak positioned northeast of the composite AC along the crest of the thickness ridge (Fig. 3.2a). The positions of the upper-tropospheric jet streaks suggest that at least some of the strong low-skill ACs may develop in a region of lateral jet coupling, a favorable region for cyclone development (e.g., Uccellini and Kocin 1987). Tao et al. (2017b) similarly indicate that AC12 is located between

two jet streaks during a portion of the intensification phase of AC12, with one jet streak located to the southwest of AC12 and another jet streak located to the northeast of AC12. A manual analysis indicates that 7 of the 13 strong low-skill ACs are associated with dual upper-tropospheric jet streaks (not shown). There is variability in the exact position and strength of upper-tropospheric jet streaks associated with the 13 strong low-skill ACs, including the dual upper-tropospheric jet streaks associated with the aforementioned 7 strong low-skill ACs, such that composite smoothing is occurring. Regardless of the composite smoothing, the dual upper-tropospheric jet streaks associated with the aforementioned 7 strong low-skill ACs likely contribute to the dual upper-tropospheric jet structure in Fig. 3.2a.

Between t_{low}−48 h and t_{low}−12 h, the two jet streaks evolve into a cyclonically curved jet streak between the thickness trough and ridge (Figs. 3.2a–d), which amplify during this period in the vicinity of the intensifying composite AC (Figs. 3.2a–d). At t_{low}−12 h, the composite AC is located in the poleward exit region of the cyclonically curved jet streak (Fig. 3.2d), a favorable region for continued intensification of the composite AC. Tao et al. (2017b) similarly show that the two jet streaks influencing AC12 evolve into a cyclonically curved jet streak, with AC12 becoming positioned in the poleward exit region of the cyclonically curved jet streak. At t_{low} and t_{low}+12 h, lower-to-midtropospheric baroclinicity weakens considerably in the vicinity of the composite AC as the composite AC reaches peak intensity and begins to weaken (Figs. 3.2e,f). The composite AC also becomes embedded in a lower-to-midtropospheric pool of cold air at t_{low}+12 h (Fig. 3.2f), suggesting that the composite AC becomes equivalent barotropic in structure. Several studies have shown that ACs become equivalent barotropic in structure at or around the time the ACs reach peak intensity (e.g., Aizawa and Tanaka 2016; Tao et al. 2017a,b; Yamagami et al. 2017).

Figures 3.3a–d indicate that there are regions of relatively large lower-to-midtropospheric Eady growth rates in the vicinity of the composite AC during t_{low}−48 h through t_{low}−12 h that are associated with the regions of strong lower-to-midtropospheric baroclinicity shown in Figs. 3.2a–d. Regions of relatively large lower-to-midtropospheric Eady growth rates extending northeast and southwest from the composite AC at t_{low}−48 h (Fig. 3.3a) are indicative of warm and cold frontal zones, respectively, associated with the strong low-skill ACs. The warm and cold frontal zones are also suggested in the thickness field in Fig. 3.2a and in the 850-hPa temperature field (not shown). The regions of relatively large lower-to-midtropospheric Eady growth rates extending northeast and southwest from the composite AC at t_{low}−48 h rotate cyclonically about the composite AC during t_{low}−48 h through t_{low}−12 h (Figs. 3.3a–d). This rotation accompanies a reconfiguration of the warm and cold frontal zones (Figs. 3.2a–d). Figures 3.2a–d and Figs. 3.3a–d suggest that baroclinic processes likely play an important role in the development and intensification of the strong low-skill ACs. The importance of baroclinic processes in the development and intensification of strong low-skill ACs is also shown by Simmonds and Rudeva (2012) and Tao et al. (2017b) for AC12, and by Yamagami et al. (2017) for AC16. Simmonds and Rudeva (2012) and Yamagami et al. (2017) similarly show that there are relatively large lower-to-midtropospheric Eady growth rates in the vicinity of AC12 and AC16, respectively, as these ACs develop and intensify.

During and shortly after the composite AC reaches peak intensity, regions of relatively large lower-to-midtropospheric Eady growth rates wrap cyclonically around much of the composite AC and become increasingly separated from the composite AC center (Figs. 3.3e,f). Concomitantly, the composite AC becomes increasingly separated from the warm sector of the composite AC (Figs. 3.2e,f), suggesting that the strong low-skill ACs become occluded and

equivalent barotropic in structure. Simmonds and Rudeva (2012), Tao et al. (2017a), and Yamagami et al. (2017) similarly show a large decrease in lower-to-midtropospheric Eady growth rates in the vicinity of the ACs in their studies as the ACs reach peak intensity and become equivalent barotropic in structure.

TPVs have been shown to play an important role in the evolution of ACs (e.g., Simmonds and Rudeva 2012; Aizawa and Tanaka 2016; Tao et al. 2017a,b; Yamagami et al. 2017). The role of upper-tropospheric TPVs and other, mid-to-upper-tropospheric features in the evolution of the strong low-skill ACs is now examined. Figure 3.4a shows that at t_{low}−48 h, the composite AC is positioned downstream of a 500-hPa short-wave trough and embedded 500-hPa relative vorticity maximum, and to the south of a broad 500-hPa vortex. The 500-hPa short-wave trough and embedded 500-hPa relative vorticity maximum (Fig. 3.4a), and the broad 500-hPa vortex (Fig. 3.4a), are associated with regions of relatively high upper-tropospheric PV (Fig. 3.5a). The 500-hPa relative vorticity maximum upstream of the composite AC and associated region of relatively high upper-tropospheric PV are likely signatures of TPVs upstream of the strong low-skill ACs. A 500-hPa relative vorticity maximum embedded within the broad 500-hPa vortex north of the composite AC (Fig. 3.4a) and an associated region of relatively high upper-tropospheric PV (Fig. 3.5a) may also be signatures of TPVs north of the strong low-skill ACs.

During t_{low}−36 h through t_{low}−12 h, the 500-hPa relative vorticity maximum upstream of the composite AC and the 500-hPa relative vorticity maximum within the broad 500-hPa vortex appear to interact with each other and gradually merge (Figs. 3.4b–d). The merger of the 500-hPa relative vorticity maxima may reflect the merger of TPVs. Yamagami et al. (2017) similarly show that AC16 intensifies as a TPV embedded within an upper-tropospheric short-wave trough

upstream of AC16 interacts and merges with a TPV embedded within an upper-tropospheric vortex initially located north of AC16.

The 500-hPa relative vorticity maximum upstream of the composite AC (Figs. 3.4b–d) and the associated region of relatively high upper-tropospheric PV (Figs. 3.5b–d) gradually approach the intensifying composite AC during t_{low}−36 h through t_{low}−12 h, suggesting that there is interaction between TPVs and the strong low-skill ACs. Tao et al. (2017b) similarly show that a TPV interacting with AC12 approaches AC12 while AC12 intensifies. At t_{low} and t_{low}+12 h, the 500-hPa relative vorticity maximum (Figs. 3.4e,f) and an associated upper-tropospheric PV maximum (Figs. 3.5e,f) become positioned over the composite AC, suggesting that TPVs become vertically superposed with the strong low-skill ACs. Several studies similarly show that TPVs become vertically superposed with ACs while the ACs intensify and reach peak intensity (e.g., Aizawa et al. 2014; Aizawa and Tanaka 2016; Tao et al. 2017a,b; Yamagami et al. 2017). Associated with the vertical superposition is the formation of a tropospheric-deep cyclone (Figs. 3.4e,f and Figs. 3.5e,f), as similarly shown by Tao et al. (2017b) for AC12. The tropospheric-deep cyclone exhibits an equivalent barotropic structure, a structure that was suggested earlier in Fig. 3.2f. TPVs and TPV–AC interactions likely play important roles in the evolution of the strong low-skill ACs.

The role of latent heating in the evolution of the strong low-skill ACs is lastly examined. Figures 3.5a–d show that there are regions of lower-to-midtropospheric ascent, upper-tropospheric divergence, and upper-tropospheric irrotational outflow in the immediate vicinity of the composite AC during t_{low}−48 h through t_{low}−12 h. The regions of lower-to-midtropospheric ascent, upper-tropospheric divergence, and upper-tropospheric irrotational outflow (Figs. 3.5a–d) are found just downstream of the TPV (Figs. 3.4a–d and Figs. 3.5a–d) during t_{low}−48 h through

t_{low}−12 h. The regions of lower-to-midtropospheric ascent, upper-tropospheric divergence, and upper-tropospheric irrotational outflow (Figs. 3.5a–d) are also found in the suggested region of upper-tropospheric jet coupling at t_{low}−48 h (Fig. 3.2a), and in and near the poleward exit region of a cyclonically curved upper-tropospheric jet streak during t_{low}−36 h through t_{low}−12 h (Figs. 3.2b–d). A well-defined IVT corridor also gradually wraps cyclonically from the southern to northern flank of the composite AC during t_{low}−48 h through t_{low}−12 h (Figs. 3.6a–d). The IVT corridor may be a manifestation of WCBs and/or ARs associated with the strong low-skill ACs. There is an abrupt decrease in IVT just northeast of the composite AC center during t_{low}−48 h through t_{low}−12 h (Figs. 3.6a–d) that corresponds to a well-defined region of IMFC (Figs. 3.6a–d). The region of IMFC implies that latent heating is occurring in the vicinity of the strong low-skill ACs and is likely contributing to the development and intensification of the strong low-skill ACs. The regions of lower-to-midtropospheric ascent, upper-tropospheric divergence, and upper-tropospheric irrotational outflow during t_{low}−48 h through t_{low}−12 h (Figs. 3.5a–d) are likely signatures of the latent heating. During t_{low} through t_{low}+12 h, the IVT corridor wraps around the composite AC (Figs. 3.6e,f), with the magnitudes of IVT and IMFC decreasing substantially (Figs. 3.6e,f) as the composite AC reaches peak intensity and begins to weaken.

The evolution of the strong low-skill ACs is consistent with the evolution of midlatitude cyclones according to quasigeostrophic (QG) theory. QG theory indicates that midlatitude cyclones develop downstream of a mid-to-upper-tropospheric relative vorticity maximum, in a region of vertically differential cyclonic vorticity advection that is associated with upper-tropospheric divergence and tropospheric-deep ascent (e.g., Martin 2006, section 8.4). Similarly, there is a region of upper-tropospheric divergence and lower-to-midtropospheric ascent in the immediate vicinity of the composite AC (Figs. 3.5a–d), just downstream of a 500-hPa relative

vorticity maximum (Figs. 3.4a–d) during t_{low}−48 h through t_{low}−12 h. QG theory indicates that the vertical tilt between midlatitude cyclones and the mid-to-upper-tropospheric relative vorticity maximum decreases as midlatitude cyclones intensify (e.g., Martin 2006, section 8.8), as similarly shown for the strong low-skill ACs in Figs. 3.4a–d during t_{low}−48 h through t_{low}−12 h. Midlatitude cyclones are then shown to reach peak intensity and weaken as they become vertically stacked with the mid-to-upper-tropospheric relative vorticity maximum (e.g., Martin 2006, section 8.8), which is similarly shown for the strong low-skill ACs in Figs. 3.4e,f during t_{low} through t_{low}+12 h.

The composite analysis for the strong low-skill ACs suggests that these ACs interact with TPVs in a region of strong lower-to-midtropospheric baroclinicity and relatively large lower-to-midtropospheric Eady growth rates, and that these ACs are associated with a well-defined IVT corridor and a well-defined region of IMFC that implies latent heating. The composite analysis for the strong low-skill ACs suggests that a combination of TPV–AC interactions, baroclinic processes, and latent heating likely contribute to the development and intensification of these ACs. The hypothesis (part of hypothesis 4) that TPVs, baroclinic zones, and WCBs, and TPV–AC interactions, baroclinic processes, and latent heating, influence the evolution of strong low-skill ACs during low-skill periods is supported. A composite analysis for strong high-skill ACs will next be examined in order to determine how features and processes influencing the evolution of strong high-skill ACs compare to the features and processes influencing the evolution of strong low-skill ACs.

2) AC-centered composites for strong high-skill ACs

Table 3.2 shows that all 13 strong high-skill ACs attain a lowest SLP in the range of 967–991 hPa when located in the Arctic. The strong high-skill ACs generally track east-northeastward or northeastward while intensifying, with the majority of the strong high-skill ACs tracking over northern Eurasia or the central Arctic Ocean (Fig. 3.7a). The strong high-skill ACs intensify at varying rates between t_{low}−48 h and t_{low}, with the mean minimum SLP decreasing from 996.5 hPa at t_{low}−48 h to 984.5 hPa at t_{low} (Fig. 3.7b). The large majority of the strong high-skill ACs (Fig. 3.7b) intensify at slower rates compared to the strong low-skill ACs (Fig. 3.1b) between t_{low}−48 h and t_{low}. The strong high-skill ACs generally weaken between t_{low} and t_{low}+36 h at rates that are comparable in magnitude to the rates at which the strong high-skill ACs intensify between t_{low}−48 h and t_{low} (Fig. 3.7b).

The role of baroclinic processes in the evolution of the strong high-skill ACs is first examined. Figure 3.8a shows that at t_{low}−48 h, the composite AC is located in a region of moderate lower-to-midtropospheric baroclinicity between a thickness trough and ridge. During t_{low}−36 h through t_{low}−12 h, the region of moderate lower-to-midtropospheric baroclinicity remains, while the thickness trough and ridge slowly amplify (Figs. 3.8b–d). By t_{low} and t_{low}+12 h, lower-to-midtropospheric baroclinicity decreases near the composite AC center as the composite AC begins to weaken (Figs. 3.8e,f). There are no coherent upper-tropospheric jet structures during t_{low}−48 h through t_{low}−24 h (Figs. 3.8a–c), and there is only a weak signature of a jet streak to the southeast of the composite AC during t_{low}−12 h through t_{low}+12 h (Figs. 3.8d–f).

There are regions of moderate lower-to-midtropospheric Eady growth rates in the vicinity of the composite AC during t_{low}−48 h through t_{low}−12 h (Figs. 3.9a–d). Regions of moderate

lower-to-midtropospheric Eady growth rates just north and northeast of the composite AC during t_{low}−48 h through t_{low}−12 h (Figs. 3.9a–d) suggest that there is a warm frontal zone associated with the strong high-skill ACs. Regions of moderate lower-to-midtropospheric Eady growth rates extending southwest from the composite AC during t_{low}−48 h through t_{low}−36 h (Figs. 3.9a,b) and south from the composite AC during t_{low}−24 h through t_{low}−12 h (Figs. 3.9c,d) suggest that there is a cold frontal zone associated with the strong high-skill ACs. The warm and cold frontal zones are also suggested in the thickness field during t_{low}−48 h through t_{low}−12 h (Figs. 3.8a–d). During t_{low} through t_{low}+12 h, regions of moderate lower-to-midtropospheric Eady growth rates (Figs. 3.9e,f), and the warm sector of the composite AC that is indicated by the thickness field (Figs. 3.8e,f), become increasingly separated from the composite AC center, suggesting that the strong high-skill ACs become occluded.

Upper-tropospheric jet structures during t_{low}−48 h through t_{low}+12 h for the strong high-skill ACs (Figs. 3.8a–f) are much weaker and less coherent than those for the strong low-skill ACs (Figs. 3.2a–f). Regions of lower-to-midtropospheric Eady growth rate during t_{low}−48 h through t_{low}+12 h for the strong high-skill ACs (Figs. 3.9a–f) are smaller and weaker than those for the strong low-skill ACs (Figs. 3.3a–f). There is greater variability in the positions of upper-tropospheric jet structures and in the positions of regions of lower-to-midtropospheric Eady growth rate among the composite members for the strong high-skill ACs than among the composite members for the strong low-skill ACs during t_{low}−48 h through t_{low}+12 h (not shown). Therefore, composite smoothing is hypothesized to be a contributing factor to the weaker and less coherent upper-tropospheric jet structures, and to the smaller and weaker regions of lower-to-midtropospheric Eady growth rate, for the strong high-skill ACs. Area-averaged upper-tropospheric wind speed and area-averaged lower-to-midtropospheric Eady growth rate in the

vicinity of the strong low-skill ACs and the strong high-skill ACs will now be examined to determine how upper-tropospheric wind speed and lower-to-midtropospheric Eady growth rate compare between these respective categories of ACs without needing to account for composite smoothing.

The mean values of area-averaged upper-tropospheric wind speed during t_{low}−48 h through t_{low}+12 h are lower (by 5.0–5.9 m s^{-1}) for the strong high-skill ACs compared to the strong low-skill ACs (Fig. 3.10a), indicating that there tends to be weaker upper-tropospheric jet structures in the vicinity of the strong high-skill ACs. To exemplify differences in area-averaged upper-tropospheric wind speed and subsequent area-averaged quantities between the strong low-skill ACs and the strong high-skill ACs, the interquartile range (IQR) will be compared between the respective categories of ACs for a representative lag time at which differences in the IQR are large. As an example of differences in area-averaged upper-tropospheric wind speed, the IQR at t_{low}−24 h ranges from 24.1 to 27.6 m s^{-1} for the strong low-skill ACs and from 18.6 to 21.9 m s^{-1} for the strong high-skill ACs (Fig. 3.10a). The mean values of area-averaged lower-to-midtropospheric Eady growth rate during t_{low}−48 h through t_{low}+12 h are smaller (by 0.09–0.14 day^{-1}) for the strong high-skill ACs compared to the strong low-skill ACs (Fig. 3.10b). As an example of differences in area-averaged lower-to-midtropospheric Eady growth rate, the IQR at t_{low}−24 h ranges from 0.77 to 0.88 day^{-1} for the strong low-skill ACs and from 0.62 to 0.77 day^{-1} for the strong high-skill ACs (Fig. 3.10b). Weaker upper-tropospheric jet structures and smaller lower-to-midtropospheric Eady growth rates for the strong high-skill ACs compared to the strong low-skill ACs suggest that baroclinic processes tend to be less robust for the strong high-skill ACs compared to the strong low-skill ACs.

The role of upper-tropospheric TPVs and other, mid-to-upper-tropospheric features in the evolution of the strong high-skill ACs is now examined. At t_{low}−48 h, there is a signature of a 500-hPa short-wave trough over the composite AC, and a 500-hPa short-wave trough upstream of the composite AC over the Kara Sea (Fig. 3.11a). The aforementioned 500-hPa short-wave troughs in Fig. 3.11a reflect variability in the positions of 500-hPa short-wave troughs influencing the strong high-skill ACs at t_{low}−48 h (not shown). Some strong high-skill ACs are associated with a 500-hPa short-wave trough over the AC at t_{low}−48 h, while other strong high-skill ACs are associated with a 500-hPa short-wave trough upstream of the AC at t_{low}−48 h. The 500-hPa short-wave trough upstream of the composite AC over the Kara Sea at t_{low}−48 h (Fig. 3.11a) gradually becomes the dominant 500-hPa short-wave trough from t_{low}−36 h through t_{low}−12 h (Figs. 3.11b–d), which partially reflects decreasing variability in the positions of 500-hPa short-wave troughs influencing the composite members (not shown). Concomitantly, a 500-hPa relative vorticity maximum just upstream of the composite AC appears to strengthen during t_{low}−24 h through t_{low}−12 h (Figs. 3.11c,d), which partially reflects decreasing variability in the positions of 500-hPa relative vorticity maxima influencing the composite members (not shown). The 500-hPa relative vorticity maximum may be a signature of TPVs interacting with the strong high-skill ACs. The aforementioned 500-hPa features discussed for Figs. 3.11a–d are associated with regions of relatively moderate-to-high upper-tropospheric PV (Figs. 3.12a–d). At t_{low} and t_{low}+12 h, the 500-hPa relative vorticity maximum (Figs. 3.11e,f) and an associated upper-tropospheric PV maximum (Figs. 3.12e,f) become positioned over the composite AC, suggesting that TPVs become vertically superposed with the strong high-skill ACs.

The 500-hPa relative vorticity maxima in the vicinity of strong high-skill ACs (Figs. 3.11a–d) appear to be weaker and exhibit less temporal continuity in structure compared to the

500-hPa relative vorticity maxima in the vicinity of the strong low-skill ACs (Figs. 3.4a–d) during t_{low}−48 h through t_{low}−12 h. There is greater variability in the positions of 500-hPa relative vorticity maxima among the composite members for the strong high-skill ACs than among the composite members for the strong low-skill ACs during t_{low}−48 h through t_{low}−12 h (not shown). Therefore, composite smoothing is hypothesized to be a contributing factor to 500-hPa relative vorticity maxima that are weaker and that exhibit less temporal continuity in structure in the vicinity of the strong high-skill ACs. Regardless of the composite smoothing, the mean values of area-averaged 500-hPa relative vorticity during t_{low}−48 h through t_{low}+12 h are smaller (by 0.9–1.9 × 10^{-5} s^{-1}) for the strong high-skill ACs compared to the strong low-skill ACs (Fig. 3.13a). As an example of differences in area-averaged 500-hPa relative vorticity, the IQR at t_{low}−12 h ranges from 6.3 to 7.2 × 10^{-5} s^{-1} for the strong low-skill ACs and from 4.7 to 5.7 × 10^{-5} s^{-1} for the strong high-skill ACs (Fig. 3.13a). Similarly, the mean values of area-averaged upper-tropospheric PV during t_{low}−48 h through t_{low}+12 h are smaller (by 0.8–1.1 PVU) for the strong high-skill ACs compared to the strong low-skill ACs (Fig. 3.13b). As an example of differences in area-averaged upper-tropospheric PV, the IQR at t_{low}−12 h ranges from 5.8 to 6.3 PVU for the strong low-skill ACs and from 4.5 to 5.3 PVU for the strong high-skill ACs (Fig. 3.13b). The smaller area-averaged 500-hPa relative vorticity and smaller area-averaged upper-tropospheric PV in the vicinity of the strong high-skill ACs compared to in the vicinity of the strong low-skill ACs suggest that there tend to be weaker TPVs in the vicinity of the strong high-skill ACs compared to in the vicinity of the strong low-skill ACs.

The possible role of latent heating in the evolution of the strong high-skill ACs is lastly examined. There are regions lower-to-midtropospheric ascent, upper-tropospheric divergence, and upper-tropospheric irrotational outflow in the immediate vicinity of the composite AC

during t_{low}−48 h through t_{low}−12 h (Figs. 3.12a–d). An IVT corridor is also found wrapping cyclonically from the southern to the northern flank of the composite AC during t_{low}−48 h through t_{low}−12 h (Figs. 3.14a–d). The IVT corridor may be a manifestation of WCBs and/or ARs associated with the strong high-skill ACs. There are regions of moderate IMFC northeast of the composite AC center during t_{low}−48 h through t_{low}−12 h (Figs. 3.14a–d), which imply that moderate latent heating occurs in the vicinity of the strong high-skill ACs. During t_{low} through t_{low}+12 h, the magnitude of IVT and IMFC decrease (Figs. 3.14e,f) as the composite AC reaches peak intensity and begins to weaken.

The regions of lower-to-midtropospheric ascent, upper-tropospheric divergence, and upper-tropospheric irrotational outflow are less robust for the strong high-skill ACs (Figs. 3.12a–d) compared to the strong low-skill ACs (Figs. 3.5a–d) during t_{low}−48 h through t_{low}−12 h. The mean values of area-averaged upper-tropospheric divergence during t_{low}−48 h through t_{low}+12 h are smaller (by 0.7–2.2 × 10^{-6} s^{-1}) for the strong high-skill ACs compared to the strong low-skill ACs (Fig. 3.15a). The mean values of area-averaged lower-to-midtropospheric ascent during t_{low}−48 h through t_{low}+12 h are smaller in magnitude (by 0.09–0.46 10^{-3} hPa s^{-1}) for the strong high-skill ACs compared to the strong low-skill ACs (Fig. 3.15b).

The IVT corridor and regions of IMFC are also weaker for the strong high-skill ACs (Figs. 3.14a–d) compared to the strong low-skill ACs (Figs. 3.6a–d) during t_{low}−48 h through t_{low}−12 h. The mean values of area-averaged IVT during t_{low}−48 h through t_{low}+12 h are smaller (by 36–81 kg m^{-1} s^{-1}) for the strong high-skill ACs compared to the strong low-skill ACs (Fig. 3.15c). The mean values of area-averaged IMFC during t_{low}−48 h through t_{low}+12 h are smaller (by 48–183 W m^{-2}) for the strong high-skill ACs compared to the strong low-skill ACs (Fig. 3.15d). Furthermore, the upper quartiles of the distributions shown in Figs. 3.15a,c,d, and the

lower quartiles of the distributions shown in Fig. 3.15b, are much higher in magnitude for the strong low-skill ACs compared to the strong high-skill ACs during t_{low}−36 h through t_{low}+12 h. For example, the upper quartile of area-averaged IVT at t_{low}−24 h ranges from 239 to 500 kg m^{-1} s^{-1} for the strong low-skill ACs and from only 170 to 198 kg m^{-1} s^{-1} for the strong high-skill ACs (Fig. 3.15c). Stronger upper-tropospheric jet structures, stronger TPVs, and larger moisture transport in the vicinity of the strong low-skill ACs compared to in the vicinity of the strong high-skill ACs likely support the stronger lower-to-midtropospheric ascent, stronger upper-tropospheric divergence, stronger upper-tropospheric irrotational outflow, and greater latent heating in the vicinity of the strong low-skill ACs.

The composite analysis for the strong high-skill ACs suggests that these ACs interact with TPVs in a region of moderate lower-to-midtropospheric baroclinicity and moderate lower-to-midtropospheric Eady growth rates, and that these ACs are associated with an IVT corridor and regions of moderate latent heating. The composite analysis for the strong high-skill ACs suggests that a combination of TPV–AC interactions, baroclinic processes, and latent heating may contribute to the development and intensification of the strong high-skill ACs. However, the features and processes influencing the evolution of the strong high-skill ACs tend to be less robust compared to the features and processes influencing the evolution of the strong low-skill ACs. The portion of hypothesis 4 stating that TPVs, baroclinic zones, and WCBs, and TPV–AC interactions, baroclinic processes, and latent heating, tend to be more robust for strong low-skill ACs during low-skill periods compared to strong high-skill ACs during low-skill periods is supported. The tendency for more robust features and processes influencing the strong low-skill ACs compared to the strong high-skill ACs likely contributes to the greater intensity of the strong low-skill ACs compared to the strong high-skill ACs. It is hypothesized that there may be

greater forecast errors associated with the more robust features and processes influencing the strong low-skill ACs compared to the strong high-skill ACs that may help explain the lower forecast skill of intensity of the strong low-skill ACs compared to the strong high-skill ACs.

d. Summary

In this chapter, AC-centered composite analyses of strong low-skill ACs during low-skill periods and strong high-skill ACs during low-skill periods were constructed and compared. The AC-centered composite analyses served as a basis to address hypothesis 4. Hypothesis 4 states that TPVs, baroclinic zones, and WCBs, and TPV–AC interactions, baroclinic processes, and latent heating, influence the evolution of strong low-skill ACs during low-skill periods and strong high-skill ACs during low-skill periods. Hypothesis 4 further states that the aforementioned features and processes tend to be more robust for strong low-skill ACs during low-skill periods. The composite analyses for the strong low-skill ACs and strong high-skill ACs, and a comparison of selected dynamic and thermodynamic quantities that are area-averaged in the vicinity of the strong low-skill ACs and strong high-skill ACs, support hypothesis 4. A summary of the most noteworthy findings is given below.

- Baroclinic processes likely support the development and intensification of the strong low-skill ACs and strong high-skill ACs, but to a larger extent for the strong low-skill ACs.
- TPVs and TPV–AC interactions likely support the development and intensification of the strong low-skill ACs and strong high-skill ACs, but to a larger extent for the strong low-skill ACs.

- Latent heating likely supports the development and intensification of the strong low-skill ACs. Latent heating may support the development and intensification of the strong high-skill ACs, but to a smaller extent compared to the strong low-skill ACs.
- The tendency for more robust features and processes influencing the strong low-skill ACs compared to the strong high-skill ACs likely contributes to the strong low-skill ACs being more intense. It is hypothesized that the more robust features and processes may be associated with larger forecast errors that may help explain the lower forecast skill of intensity of the strong low-skill ACs.

e. Tables

Table 3.1. Dates and lowest SLP attained in the Arctic (hPa) for the strong low-skill ACs.

Dates	Lowest SLP in Arctic (hPa)
21–25 July 2010	970.1
13–18 August 2010	968.3
2–12 August 2012	962.5
4–10 August 2013	977.1
18–21 June 2016	972.8
13–19 August 2016	968.3
17–21 August 2016	970.0
21–25 August 2016	972.0
25–27 August 2016	966.8
25–28 August 2016	978.1
31 July–4 August 2017	963.7
9–14 August 2017	975.6
6–16 August 2017	972.9

Table 3.2. Dates and lowest SLP attained in the Arctic (hPa) for the strong high-skill ACs.

Dates	Lowest SLP in Arctic (hPa)
31 May–3 June 2008	987.3
21–29 June 2008	967.9
14–20 August 2009	985.3
4–10 July 2010	982.8
6–18 July 2010	979.6
25–31 July 2010	981.5
28 July–3 August 2012	986.3
18–24 August 2012	987.9
24–25 June 2017	983.3
12–18 July 2017	987.9
25–30 August 2017	987.0
28 August–4 September 2017	990.8
31 August–7 September 2017	990.3

f. Figures

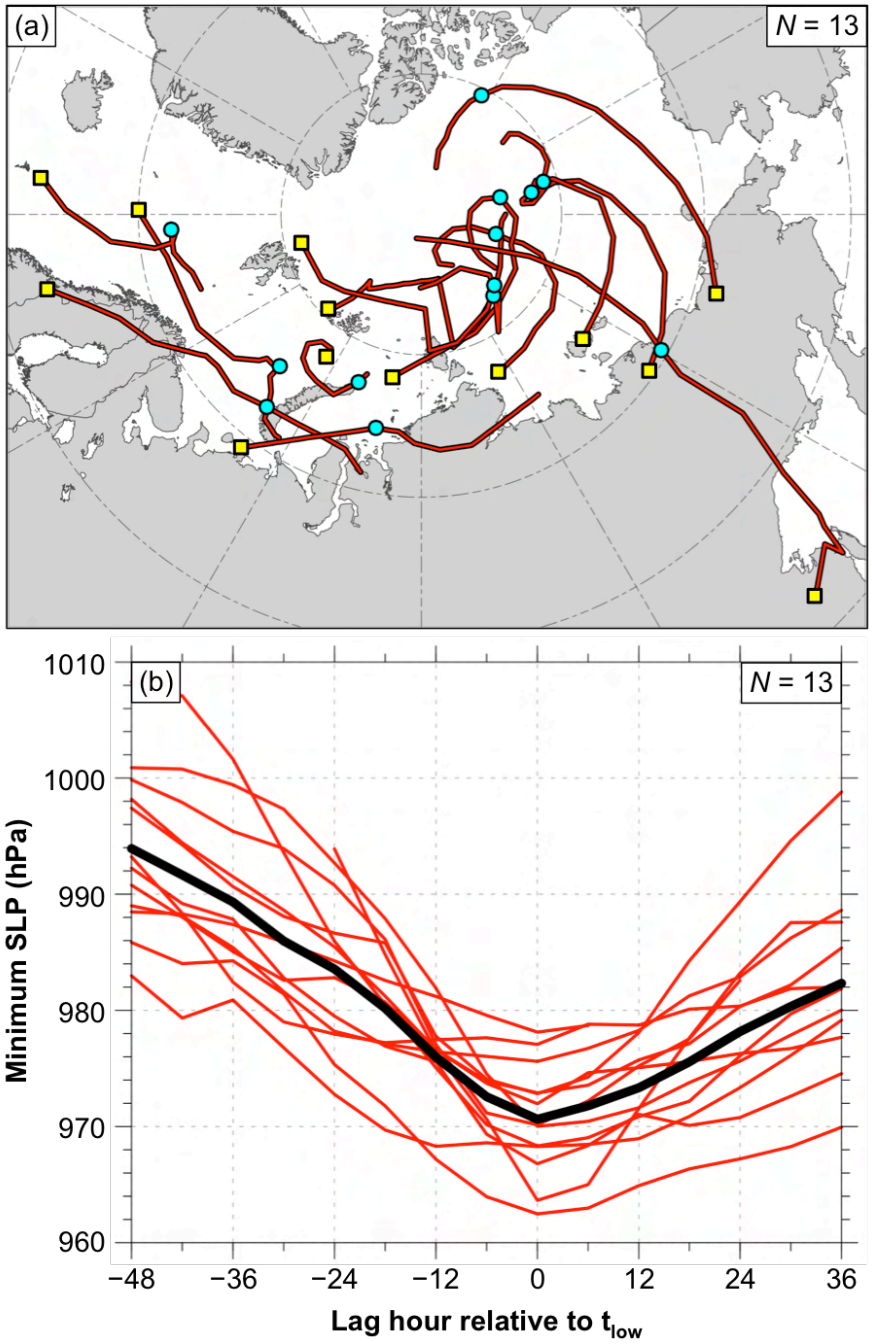

Fig. 3.1. (a) Red lines indicate tracks of the strong low-skill ACs during lag hours of −48 to +36 h, every 6 h, relative to t_{low} (i.e., time of lowest SLP of the ACs when located in the Arctic), when valid. Yellow squares indicate locations of the ACs at earliest valid lag hour, and cyan circles indicate locations of the ACs at t_{low}. (b) Red lines indicate minimum SLP (hPa) of the ACs during lag hours of −48 to +36 h, every 6 h, relative to t_{low}, when valid, and black line indicates mean minimum SLP (hPa) of the ACs during lag hours of −48 to +36 h, every 6 h, relative to t_{low}.

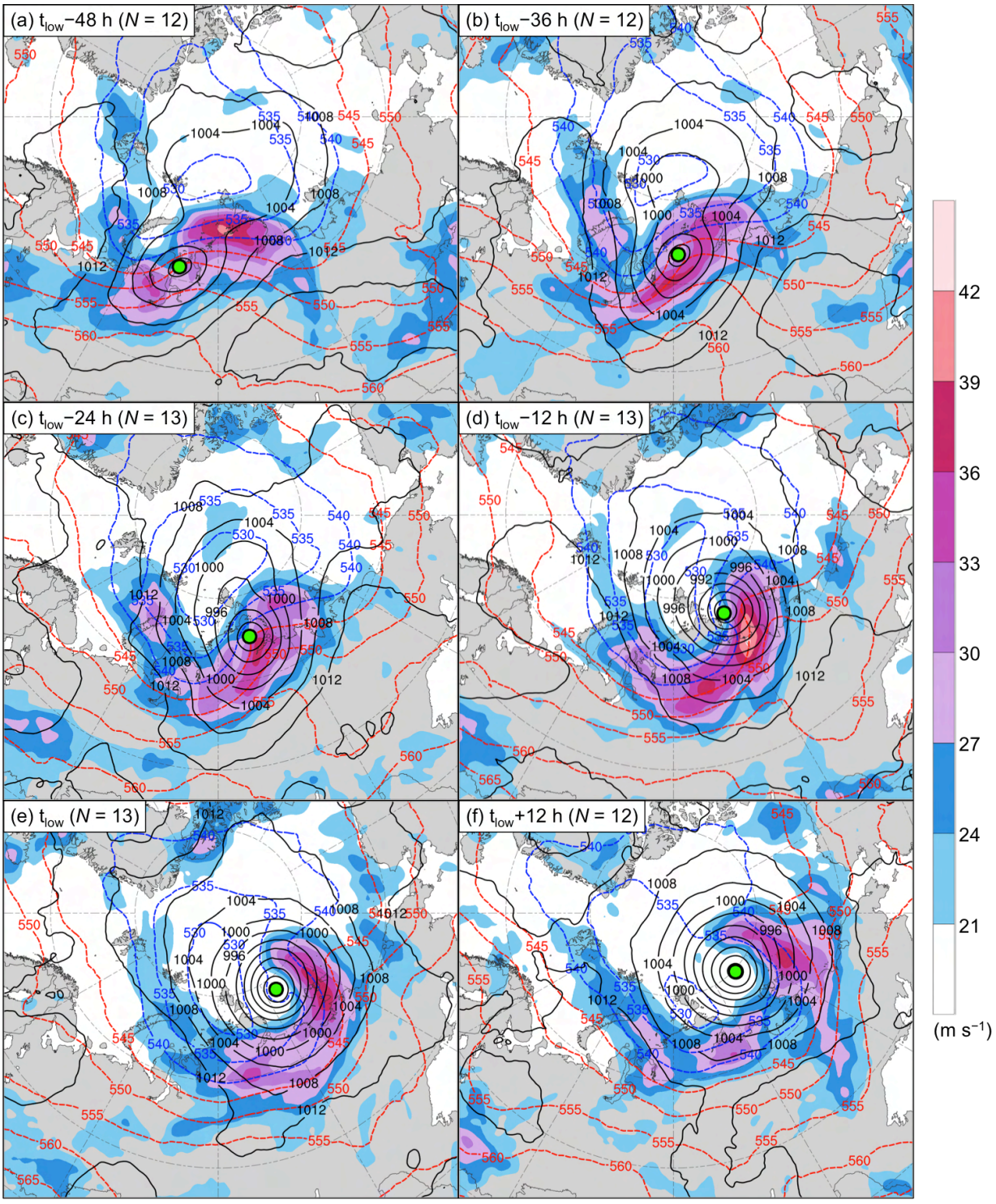

Fig. 3.2. AC-centered composites for the strong low-skill ACs of 300-hPa wind speed (m s^{-1}; shading), 1000–500-hPa thickness (dam; dashed red and blue contours), and SLP (hPa; black contours) at (a) t_{low}−48 h, (b) t_{low}−36 h, (c) t_{low}−24 h, (d) t_{low}−12 h, (e) t_{low}, and (f) t_{low}+12 h. The green dot shows the location of the composite AC.

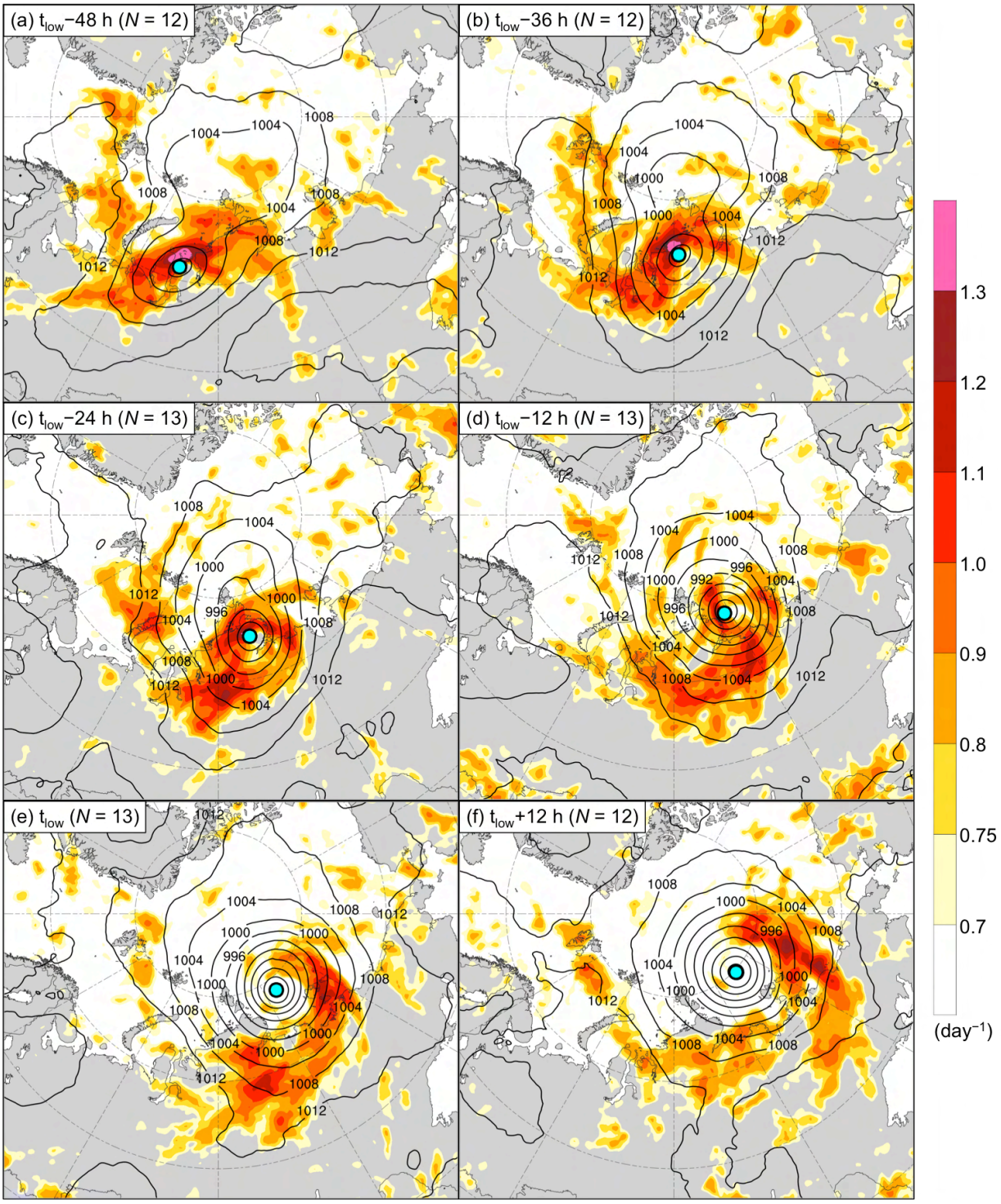

Fig. 3.3. AC-centered composites for the strong low-skill ACs of 850–600-hPa Eady growth rate (day^{-1}; shading) and SLP (hPa; black contours) at (a) t_{low}−48 h, (b) t_{low}−36 h, (c) t_{low}−24 h, (d) t_{low}−12 h, (e) t_{low}, and (f) t_{low}+12 h. The cyan dot shows the location of the composite AC.

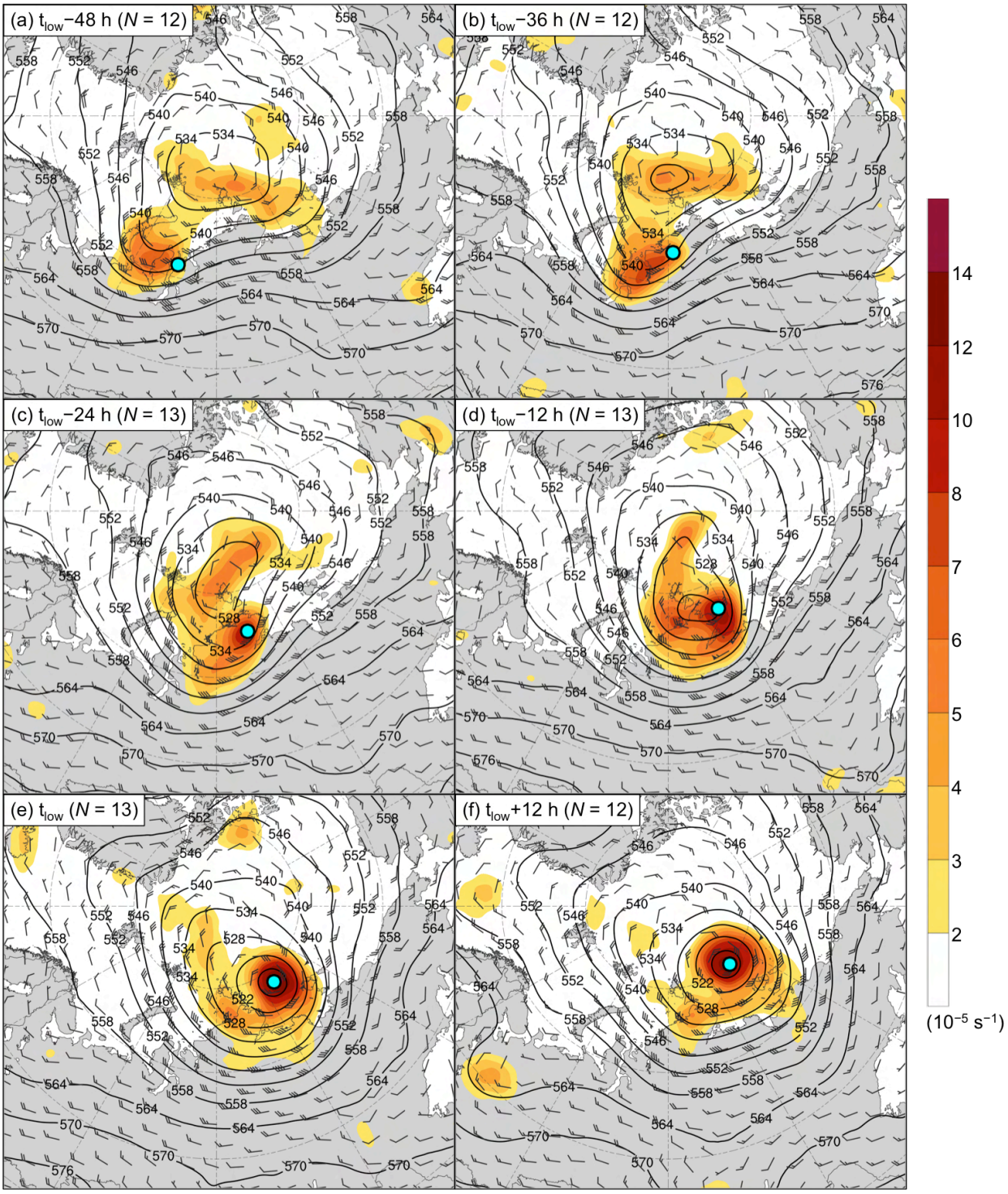

Fig. 3.4. AC-centered composites for the strong low-skill ACs of 500-hPa relative vorticity area averaged within 200 km of each grid point (10^{-5} s^{-1}; shading), 500-hPa geopotential height (dam; black contours), and 500-hPa wind (m s^{-1}; flags and barbs) at (a) t_{low}−48 h, (b) t_{low}−36 h, (c) t_{low}−24 h, (d) t_{low}−12 h, (e) t_{low}, and (f) t_{low}+12 h. The cyan dot shows the location of the composite AC.

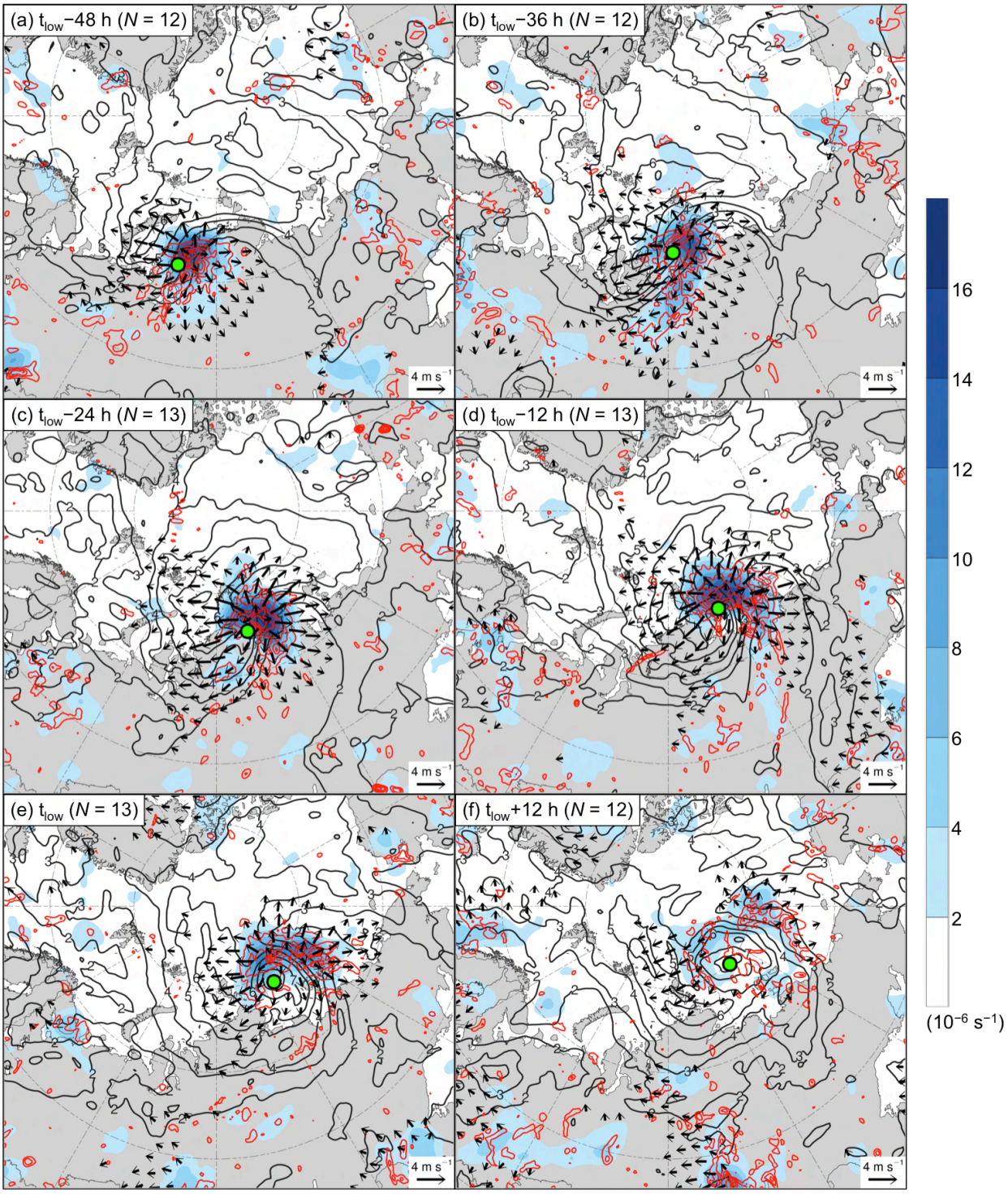

Fig. 3.5. AC-centered composites for the strong low-skill ACs of 350–250-hPa divergence area averaged within 200 km of each grid point (10^{-6} s^{-1}; shading), 350–250-hPa irrotational wind (m s^{-1}; vectors), 350–250-hPa PV (PVU; dark gray contours), and negative values of 800–600-hPa ω (every 1 × 10^{-3} hPa s^{-1}; red contours) at (a) t_{low}−48 h, (b) t_{low}−36 h, (c) t_{low}−24 h, (d) t_{low}−12 h, (e) t_{low}, and (f) t_{low}+12 h. The green dot shows the location of the composite AC.

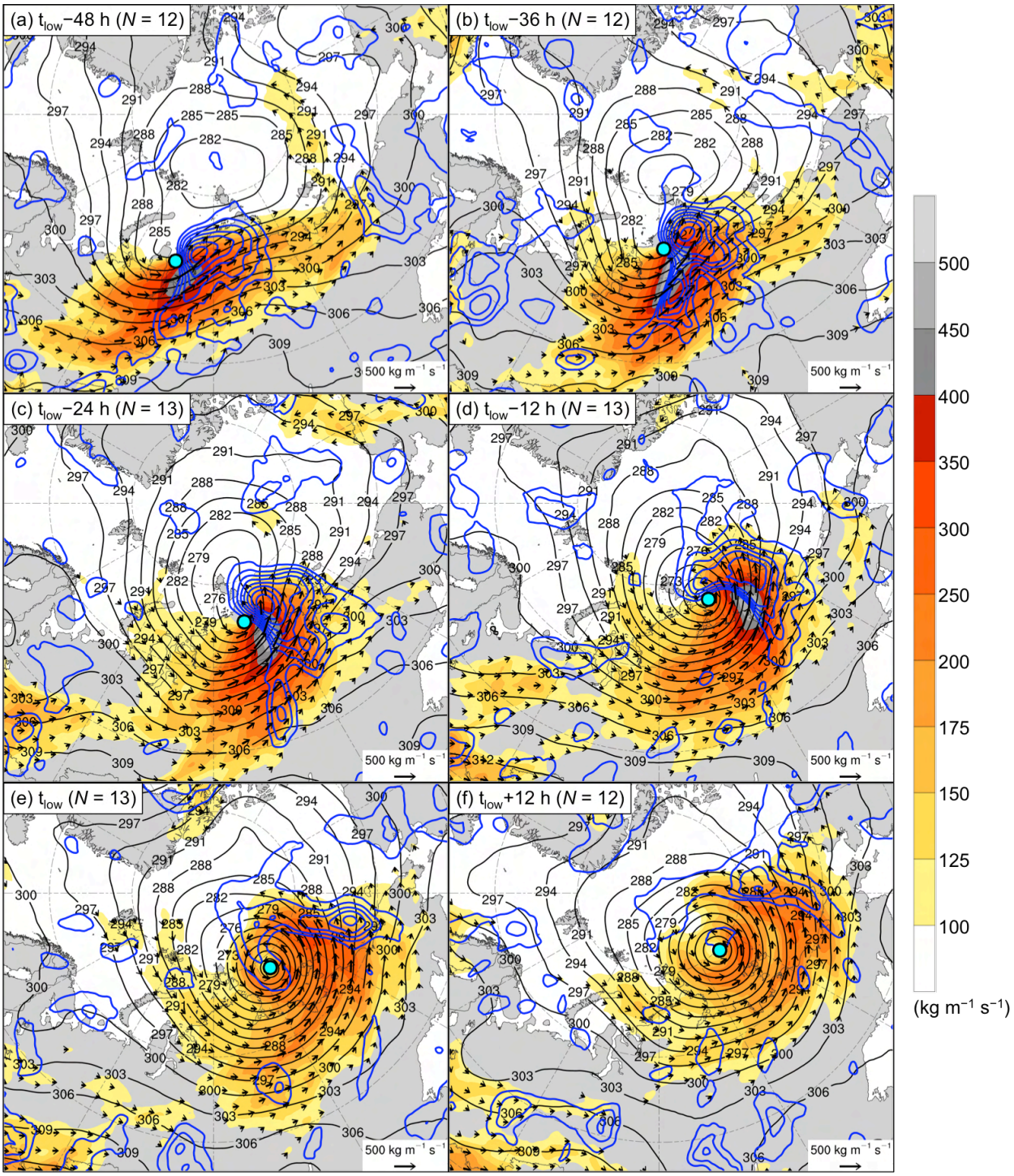

Fig. 3.6. AC-centered composites for the strong low-skill ACs of 1000–300-hPa IVT (kg m^{-1} s^{-1}; shading and vectors), positive values of 1000–300-hPa IMFC area averaged within 200 km of each grid point (every 100 W m^{-2}; blue contours), and 700-hPa geopotential height (dam; black contours) at (a) t_{low}−48 h, (b) t_{low}−36 h, (c) t_{low}−24 h, (d) t_{low}−12 h, (e) t_{low}, and (f) t_{low}+12 h. The cyan dot shows the location of the composite AC.

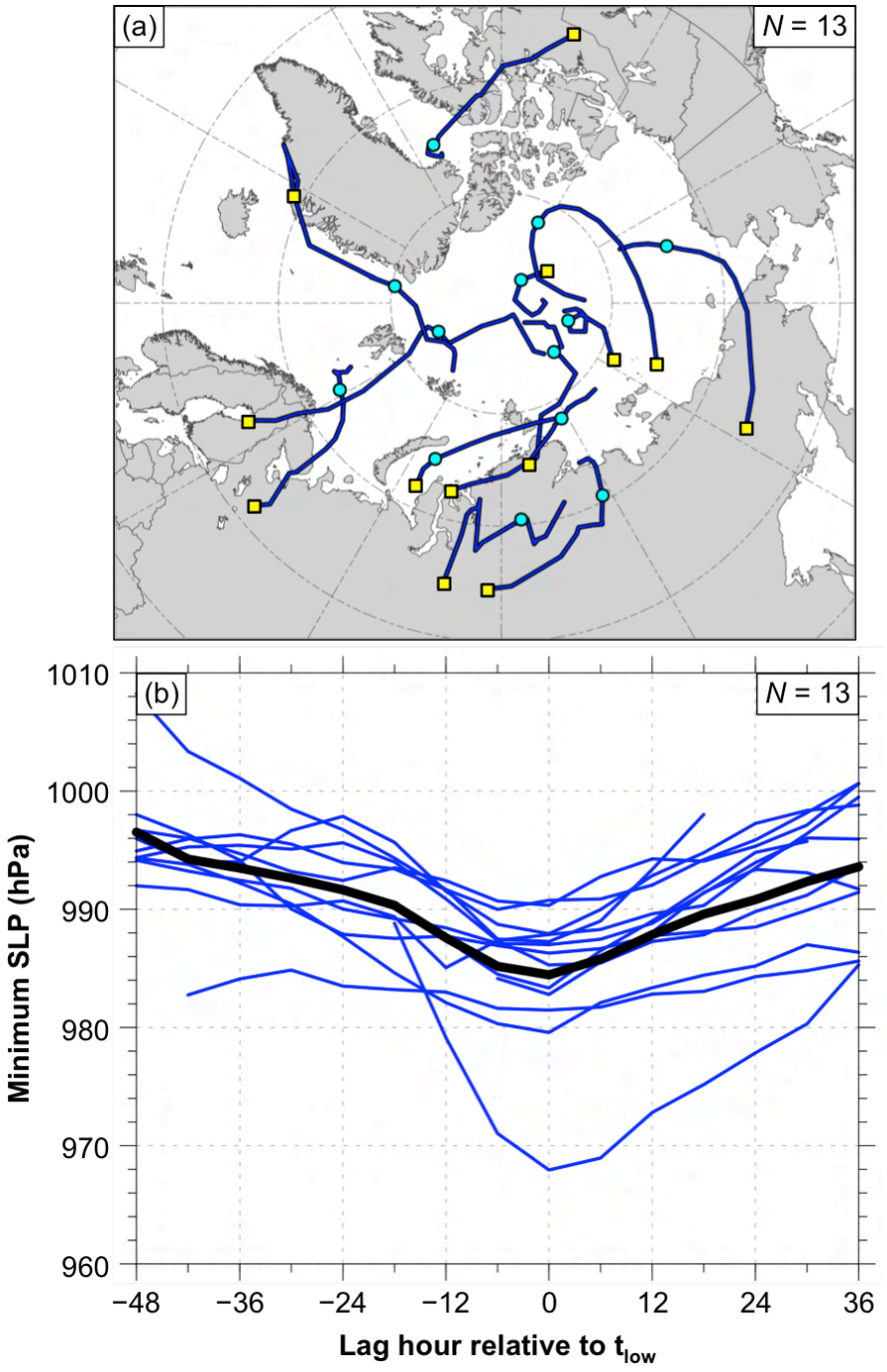

Fig. 3.7. (a) Blue lines indicate tracks of the strong high-skill ACs during lag hours of −48 to +36 h, every 6 h, relative to t_{low} (i.e., time of lowest SLP of the ACs when located in the Arctic), when valid. Yellow squares indicate locations of the ACs at earliest valid lag hour, and cyan circles indicate locations of the ACs at t_{low}. (b) Blue lines indicate minimum SLP (hPa) of the ACs during lag hours of −48 to +36 h, every 6 h, relative to t_{low}, when valid, and black line indicates mean minimum SLP (hPa) of the ACs during lag hours of −48 to +36 h, every 6 h, relative to t_{low}.

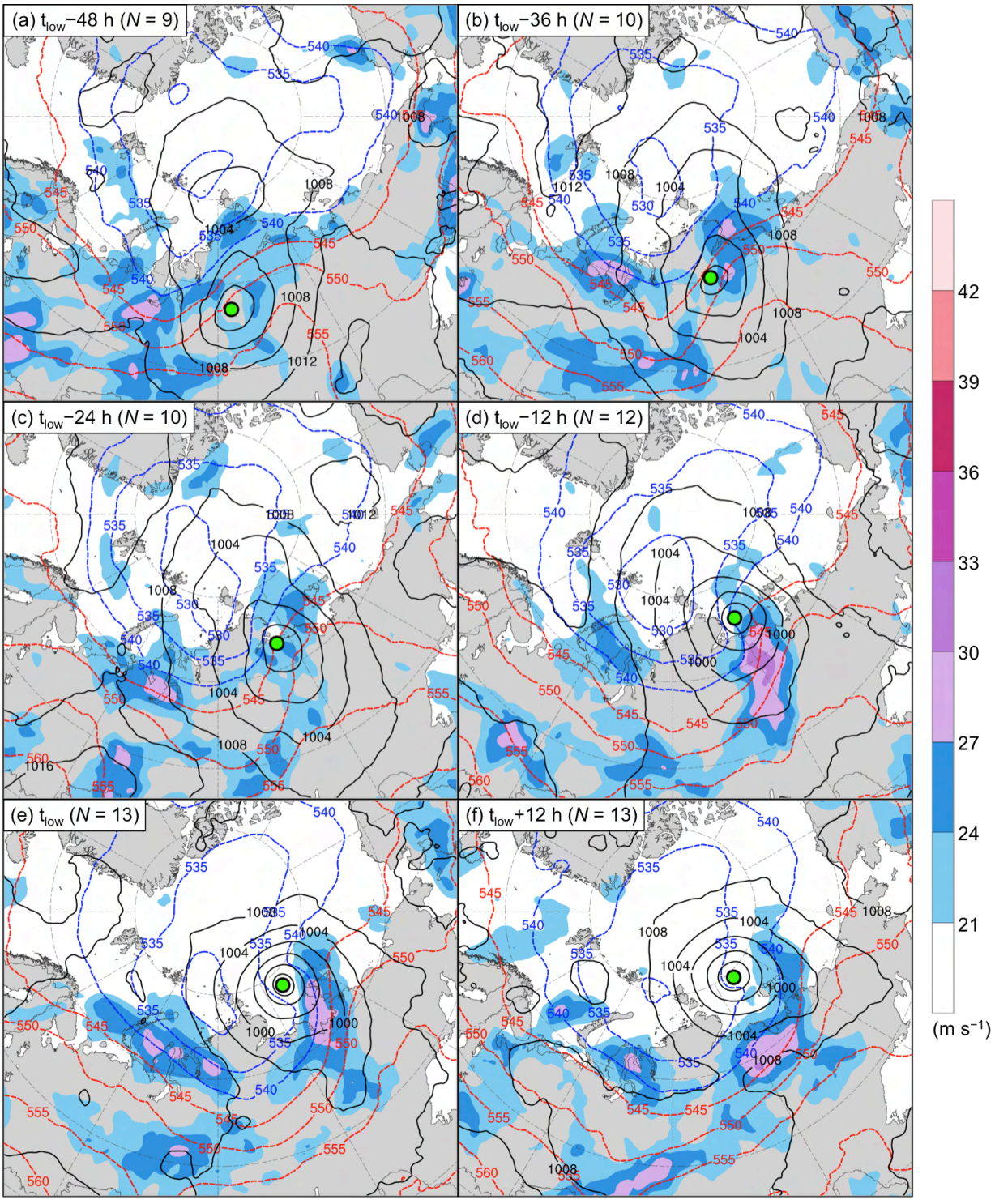

Fig. 3.8. As in Fig. 3.2, but for the strong high-skill ACs.

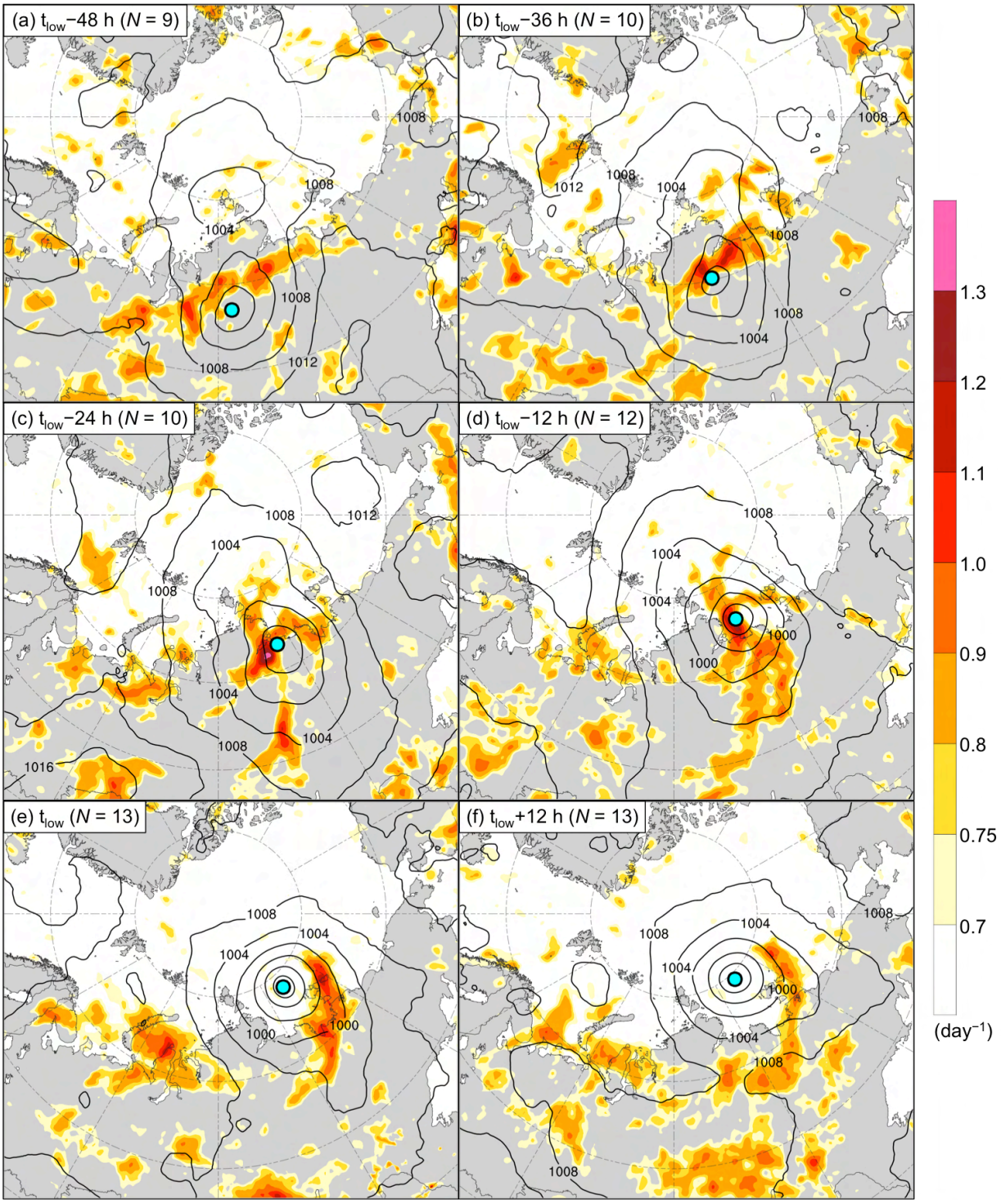

Fig. 3.9. As in Fig. 3.3, but for the strong high-skill ACs.

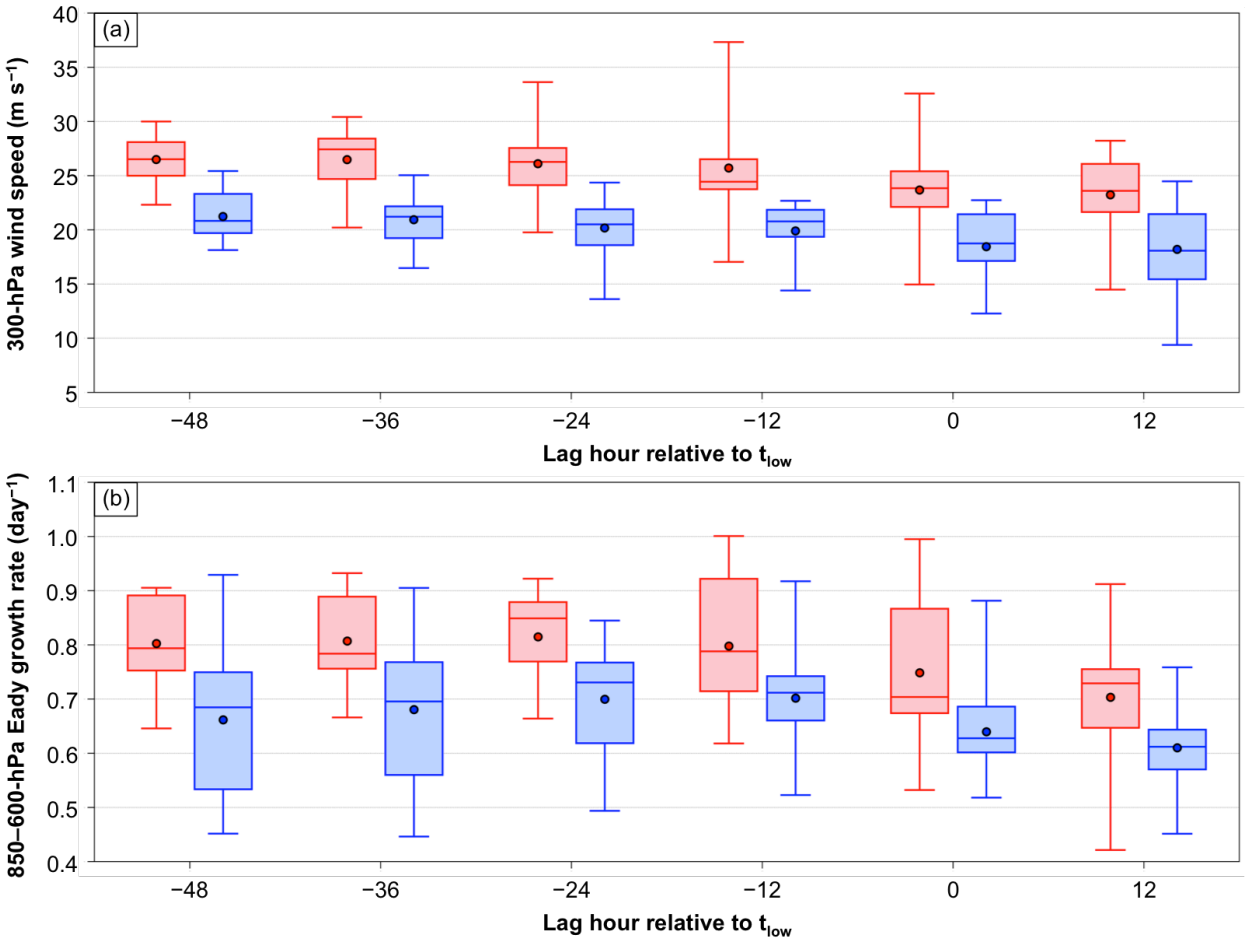

Fig. 3.10. Distributions of (a) area-averaged 300-hPa wind speed (m s^{-1}) and (b) area-averaged 850–600-hPa Eady growth rate (day^{-1}) for the strong low-skill ACs (red) and the strong high-skill ACs (blue) at lag hours of −48 to +12 h, every 12 h, relative to t_{low}. The quantities in (a) and (b) are area-averaged within a 1000-km radius from the centers of the ACs. Dots indicate the mean values, boxes indicate the IQR, and whiskers extend to the minimum and maximum values.

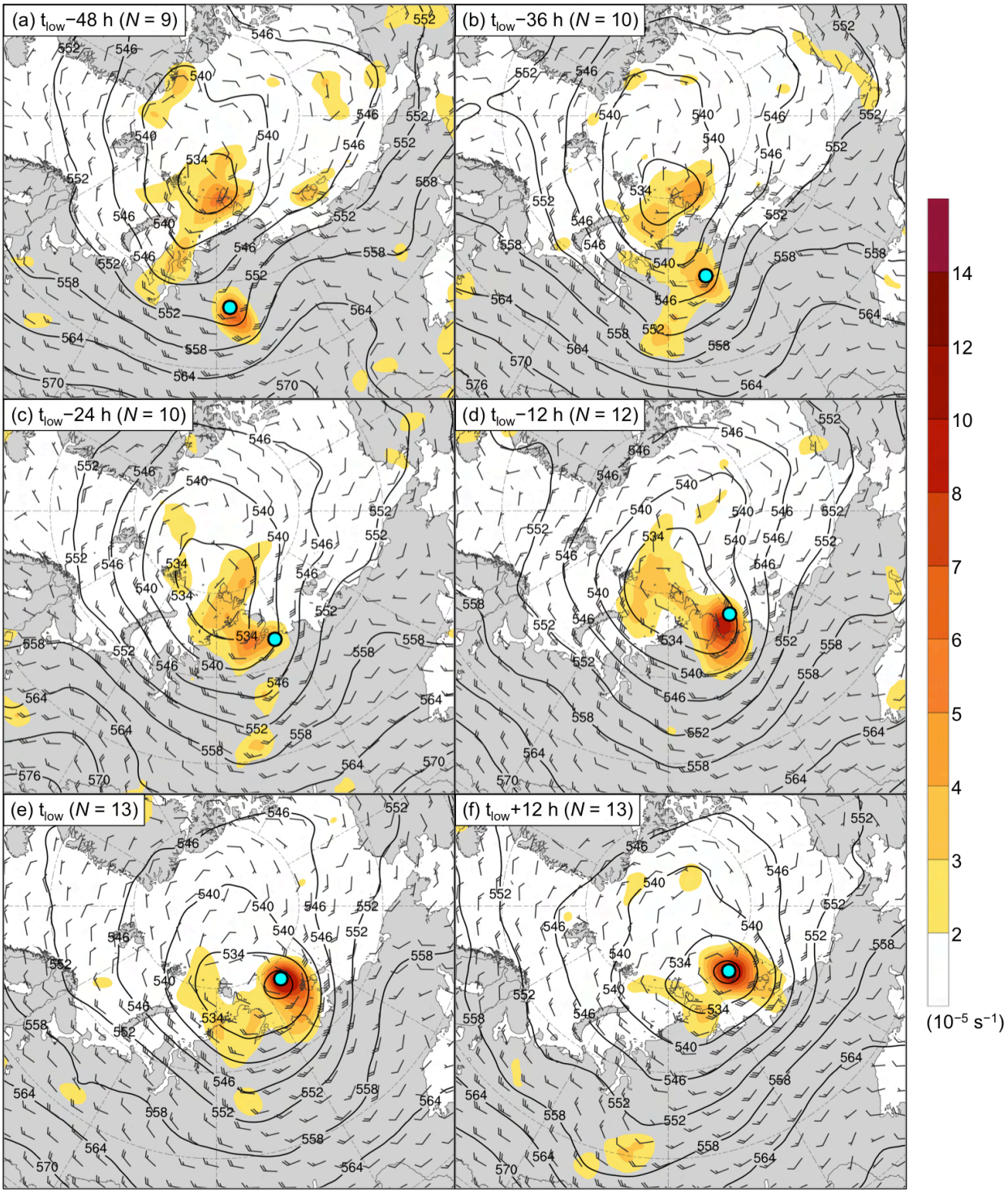

Fig. 3.11. As in Fig. 3.4, but for the strong high-skill ACs.

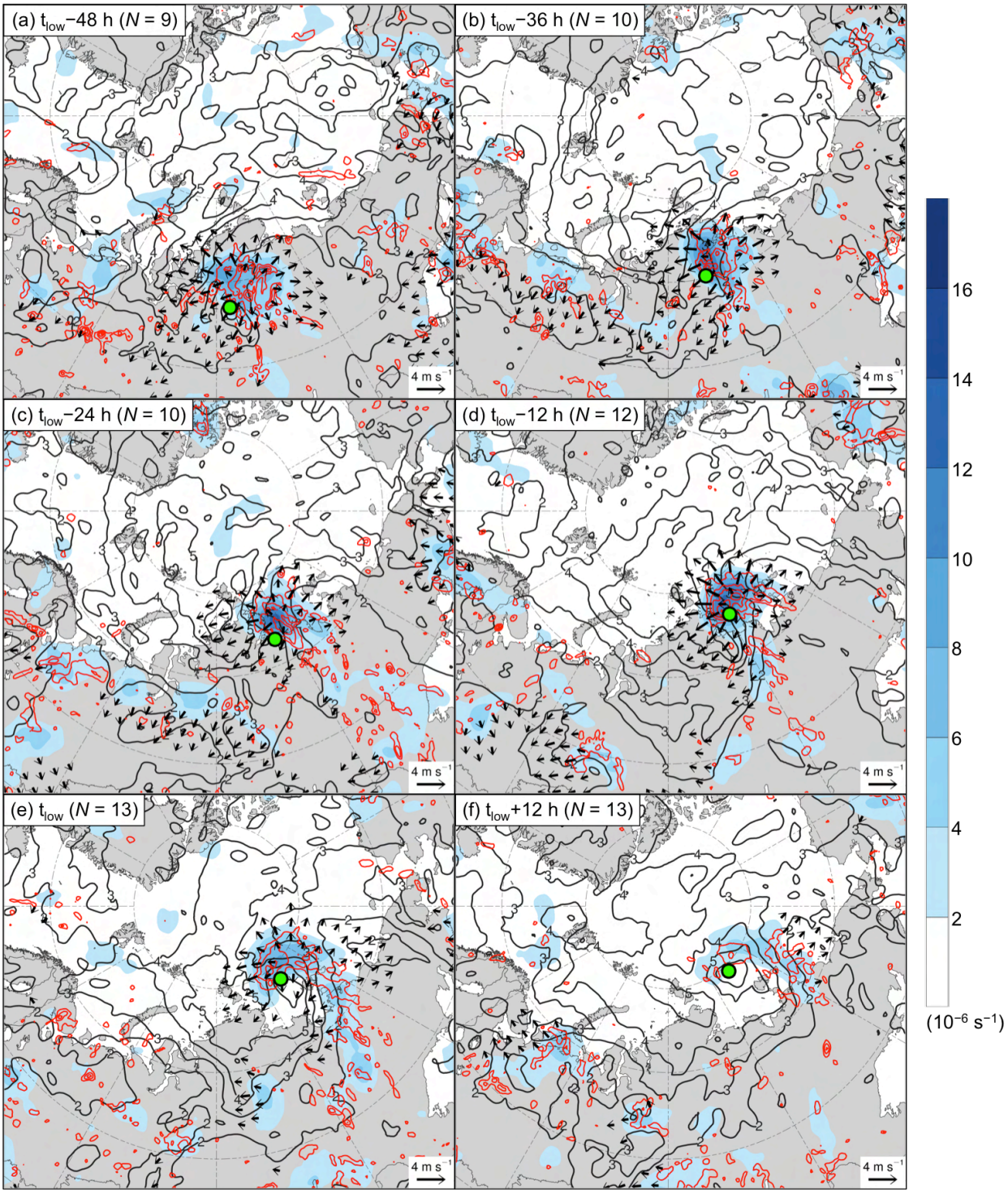

Fig. 3.12. As in Fig. 3.5, but for the strong high-skill ACs.

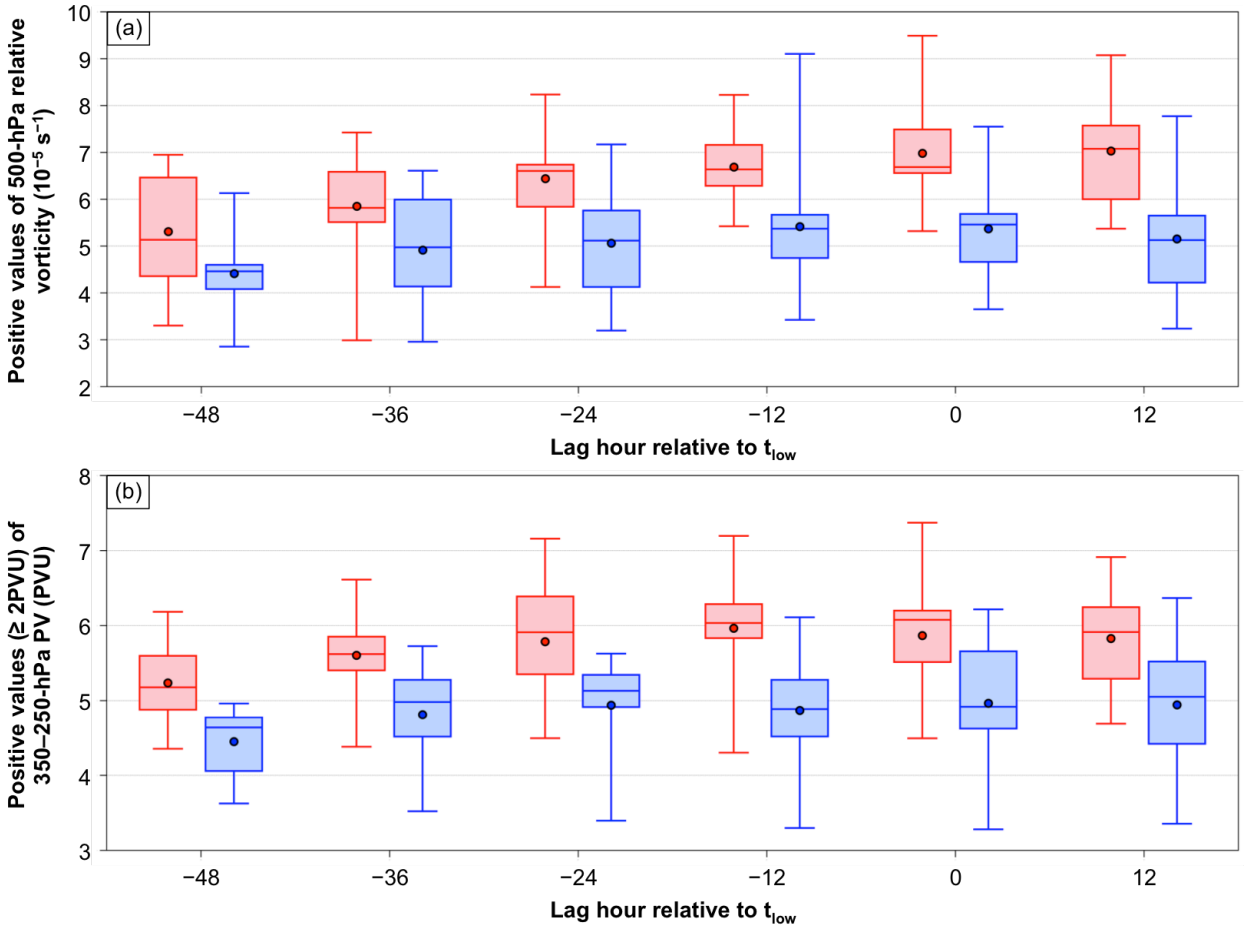

Fig. 3.13. As in Fig. 3.10, but for (a) area-averaged positive values of 500-hPa relative vorticity (10^{-5} s^{-1}) and (b) area-averaged positive values (≥ 2 PVU) of 350–250-hPa PV (PVU) for the strong low-skill ACs (red) and the strong high-skill ACs (blue) at lag hours of −48 to +12 h, every 12 h, relative to t_{low}. The quantities in (a) and (b) are area-averaged within a 1000-km radius from the centers of the ACs.

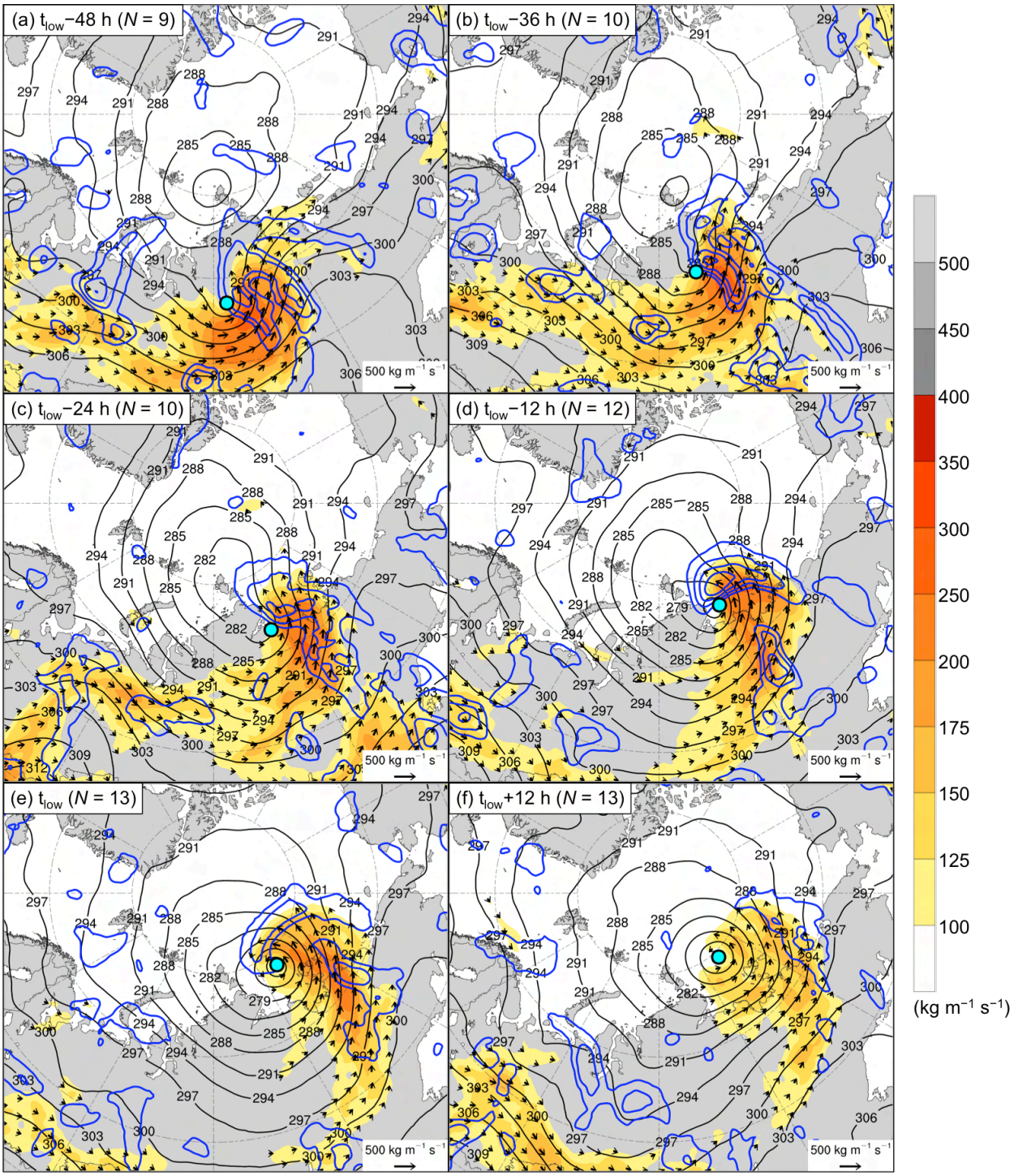

Fig. 3.14. As in Fig. 3.6, but for the strong high-skill ACs.

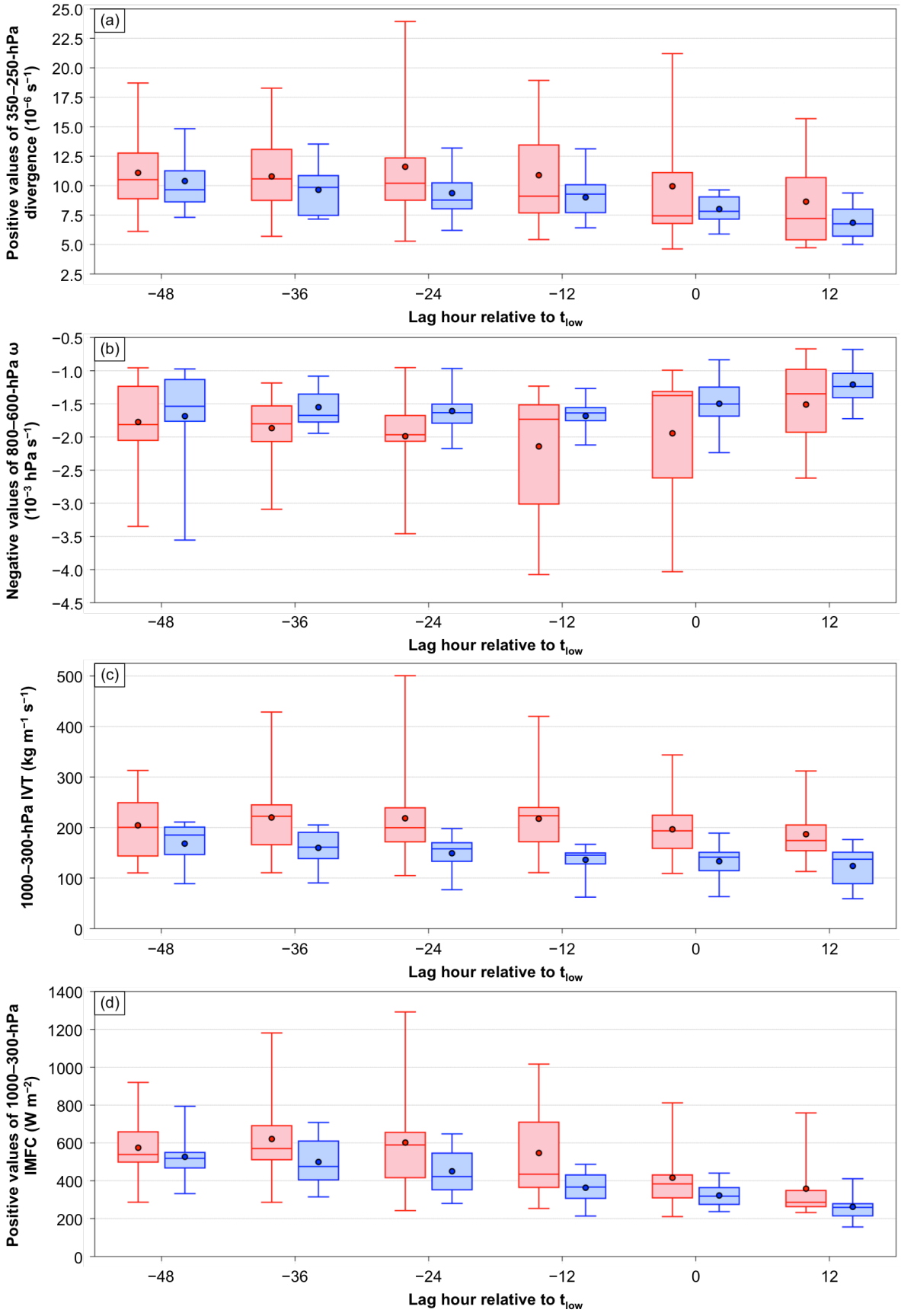
(a)
Positive values of 350–250-hPa divergence (10^{-6} s^{-1})
25.0
22.5
20.0
17.5
15.0
12.5
10.0
7.5
5.0
2.5
−48
−36
−24
−12
0
12
Lag hour relative to t_{low}
(b)
Negative values of 800–600-hPa ω (10^{-3} hPa s^{-1})
−0.5
−1.0
−1.5
−2.0
−2.5
−3.0
−3.5
−4.0
−4.5
−48
−36
−24
−12
0
12
Lag hour relative to t_{low}
(c)
1000–300-hPa IVT (kg m^{-1} s^{-1})
500
400
300
200
100
0
−48
−36
−24
−12
0
12
Lag hour relative to t_{low}
(d)
Positive values of 1000–300-hPa IMFC (W m^{-2})
1400
1200
1000
800
600
400
200
0
−48
−36
−24
−12
0
12
Lag hour relative to t_{low}

Fig. 3.15. As in Fig. 3.10, but for (a) area-averaged positive values of 350–250-hPa divergence (10^{-6} s^{-1}), (b) area-averaged negative values of 800–600-hPa ω (10^{-3} hPa s^{-1}), (c) area-averaged 1000–300-hPa IVT (kg m^{-1} s^{-1}), and (d) area-averaged positive values of 1000–300-hPa IMFC (W m^{-2}) for the strong low-skill ACs (red) and the strong high-skill ACs (blue) at lag hours of −48 to +12 h, every 12 h, relative to t_{low}. The quantities in (a)–(d) are area-averaged within a 1000-km radius from the centers of the ACs.

4. Features and processes influencing the forecast skill of a selected strong low-skill AC

a. Overview and objectives

In this chapter, hypothesis 5 is addressed. Hypothesis 5 states that forecast errors in TPVs, baroclinic zones, and WCBs, and forecast errors in TPV–AC interactions, baroclinic processes, and latent heating, contribute to forecast errors in strong low-skill ACs during low-skill periods. Hypothesis 5 is addressed by analyzing and comparing ensemble forecasts of a strong low-skill AC that occurred during 13–19 August 2016 (i.e., AC16), which is a representative member of the strong low-skill ACs during low-skill periods from section 3c(1). AC16 tracks east-northeastward north of Eurasia during 13–19 August in ERA5 (Fig. 4.1a). AC16 rapidly intensifies during 13–15 August, reaching a peak intensity of 968.5 hPa at 0000 UTC 16 August in ERA5 (Fig. 4.1b).

b. Data and methods

ERA5 is utilized to perform a synoptic-dynamic analysis of AC16 and to identify features and processes influencing the evolution of AC16. Forecasts from the 51-member ECMWF EPS that are extracted from The Observing System Research and Predictability Experiment (THORPEX) Interactive Grand Global Ensemble (TIGGE) (Bougeault et al. 2010) at 0.5° horizontal resolution are utilized to examine the forecast skill of the intensity and position of AC16. Ensemble forecasts of the intensity and position of AC16 from the ECMWF EPS initialized at 0000 UTC 10 August and verifying at 0000 UTC 15 August (120 h) are the focus of interest, as the corresponding ensemble forecasts of the intensity of AC16 in the GEFS reforecast dataset version 2 were determined in section 2b(4) to be characterized by low forecast skill during this period.

AC16 is tracked in the ensemble forecasts by utilizing the objective SLP-based cyclone tracking algorithm developed by Crawford et al. (2021). The cyclone matching procedure described in section 2b(4) is used to find the matching forecast AC track corresponding to AC16 in each ensemble forecast. If no matching forecast AC track is identified in an ensemble forecast, AC16 is manually identified and tracked in the ensemble forecast. The intensity error and position error of AC16 is calculated for each ensemble forecast at 0000 UTC 15 August (120 h). The intensity error of AC16 is calculated as the absolute difference in minimum SLP between AC16 in the ensemble forecast and AC16 in ERA5. The position error of AC16 is calculated as the great circle distance between the location of minimum SLP of AC16 in the ensemble forecast and the location of minimum SLP of AC16 in ERA5. Figure 4.2 shows the intensity and position of AC16 at 0000 UTC 15 August (120 h) in ERA5 and the ensemble forecasts. The ensemble forecasts show that there is large uncertainty in the intensity and position of AC16 at 0000 UTC 15 August (120 h) (Fig. 4.2). Intensity errors among the ensemble forecasts range from 0.2 to 29.0 hPa and position errors among the ensemble forecasts range from 83 to 1306 km. Ensembles with a more accurate intensity forecast of AC16 tend to have a more accurate position forecast of AC16 (Fig. 4.2). The correlation coefficient (r) between intensity error and position error is 0.72, indicating that intensity error and position error correlate fairly well with each other.

The ensemble-based sensitivity analysis (ESA) technique (e.g., Torn and Hakim 2008) is utilized to examine the sensitivity of the forecast skill of intensity and position of AC16 to selected dynamic and thermodynamic quantities at earlier forecast lead times. The sensitivity of a forecast metric of interest J to a model state variable x_i at an earlier forecast lead time for an ensemble of size M is calculated via

$$\frac{\partial J}{\partial x_i} = \frac{\mathrm{cov}(\mathbf{J}, \mathbf{x}_i)}{\mathrm{var}(\mathbf{x}_i)}, \tag{5}$$

where **J** denotes the $1 \times M$ ensemble estimate of the forecast metric, $\mathbf{x}_i$ denotes the $1 \times M$ ensemble estimate of the ith model state variable, cov denotes the covariance, and var denotes the variance (e.g., Torn and Hakim 2008). The values of x_i are normalized by the ensemble standard deviation of x_i following Torn and Romine (2015), such that all sensitivities have units of the forecast metric per standard deviation of the model state variable. This normalization allows various model state variables characterized by different units and different intrinsic variability to be quantitatively compared (e.g., Torn and Romine 2015). Sensitivity is determined to be statistically significant at the 95% confidence level by following the methodology of Torn and Hakim (2008).

A forecast metric J that is representative of both intensity error and position error of AC16 is determined. Average SLP within a circle surrounding the ERA5 position of AC16 at 0000 UTC 15 August (120 h) is used as a proxy for intensity error and position error of AC16, with lower average SLP within the circle anticipated to correspond to smaller intensity error and smaller position error of AC16. Circles with radii of 100–1200 km, every 100 km, were tested. A radius of 700 km was found to be optimal for correlating average SLP within the circle with intensity error and position error. The correlation coefficient (r) between average SLP within the 700-km circle and intensity error at 0000 UTC 15 August (120 h) (circle shown in Fig. 4.2) is 0.76, which is the highest value of all radii tested. The correlation coefficient (r) between average SLP within the 700-km circle and position error at 0000 UTC 15 August (120 h) is 0.87, which is the second highest value of all radii tested. Therefore, average SLP within the 700-km circle at 0000 UTC 15 August (120 h) is utilized as the forecast metric, which is hereafter referred to as J_{AC}.

In addition to utilizing the ESA technique, the most-accurate and least-accurate ensemble forecasts of AC16 are identified and compared to understand how features and processes influencing AC16 evolve differently between these respective categories of forecasts. The most-accurate and least-accurate ensemble forecasts of AC16 are determined by adopting the methodology used by Lamberson et al. (2016) to identify the most-accurate ensemble forecasts of a strong midlatitude cyclone. The ensemble forecasts initialized at 0000 UTC 10 August are utilized. At each forecast time from 1200 UTC 13 August (84 h) through 0000 UTC 16 August (144 h), every 12 h, the intensity error and position error of AC16 for each ensemble forecast are calculated as described earlier. The intensity errors and position errors are then averaged over time for each ensemble forecast. The ensemble forecasts are ranked 1 to 51 for average intensity error and for average position error. The intensity error ranks and position error ranks are then added together. The 10 ensemble forecasts with the lowest combined intensity and position error ranks are considered the most-accurate ensemble forecasts, and the 10 ensemble forecasts with the highest combined intensity and position error ranks are considered the least-accurate ensemble forecasts.

The tracks of AC16 for the most-accurate ensemble forecasts are located farther to the northwest and closer to the track of AC16 for ERA5 compared to the tracks of AC16 for the least-accurate ensemble forecasts (Fig. 4.3a). The intensity time series of AC16 for the most-accurate ensemble forecasts more closely resemble the intensity time series of AC16 for ERA5 compared to the intensity time series of AC16 for the least-accurate ensemble forecasts (Fig. 4.3b). At 0000 UTC 15 August, there are large differences in the intensity of AC16 between the most-accurate and least-accurate ensemble forecasts, with minimum SLP values of AC16

ranging from 968 to 981 hPa for the most-accurate ensemble forecasts and from 989 to 1002 hPa for the least-accurate ensemble forecasts (Fig. 4.3b).

c. Results

1) ERA5 synoptic-dynamic overview

At 1200 UTC 13 August, shortly after AC16 forms, AC16 is positioned in a region of strong lower-to-midtropospheric baroclinicity, between a thickness trough and ridge and beneath a strong upper-tropospheric jet streak (Fig. 4.4a). By 0000 UTC 14 August, the strong upper-tropospheric jet streak splits into dual upper-tropospheric jet streaks (Fig. 4.4b), with AC16 intensifying in a region of apparent upper-tropospheric jet coupling. During 0000 UTC 14–0000 UTC 15 August, the thickness trough and ridge amplify, the dual upper-tropospheric jet streaks gradually evolve into a cyclonically curved upper-tropospheric jet streak, and AC16 continues to intensify in a region of strong lower-to-midtropospheric baroclinicity (Figs. 4.4b–d). Regions of strong lower-to-midtropospheric baroclinicity extending east and south from AC16 during 1200 UTC 13–0000 UTC 15 August (Figs. 4.4a–d) are indicative of warm and cold frontal zones, respectively, associated with AC16. During 1200 UTC 15–0000 UTC 16 August, AC16 reaches peak intensity and lower-to-midtropospheric baroclinicity decreases near the center of AC16 (Figs. 4.4e,f), suggesting that AC16 becomes occluded. Figures 4.4a–d suggest that baroclinic processes play an important role in the development and intensification of AC16, which is in agreement with the findings of Yamagami et al. (2017).

TPVs that may influence AC16 are identified in terms of maxima in upper-tropospheric PV. TPVs could be identified in terms of minima of dynamic tropopause potential temperature in future work. Figures 4.5a–d show that AC16 intensifies downstream of an upper-tropospheric

PV maximum that gradually approaches AC16 during 1200 UTC 13–0000 UTC 15 August. The upper-tropospheric PV maximum corresponds to a TPV that interacts with AC16. There is also a second upper-tropospheric PV maximum corresponding to a TPV located to the northeast of AC16 over the Arctic during 1200 UTC 13–1200 UTC 14 August (Figs. 4.5a–c). At 0000 UTC 14 August, enhanced upper-tropospheric PV gradients are established between an amplifying upper-tropospheric ridge downstream of AC16 and the TPV northeast of AC16 (Fig. 4.5b), and between the aforementioned upper-tropospheric ridge and the TPV upstream of AC16 (Fig. 4.5b). The establishment of the enhanced upper-tropospheric PV gradients likely is associated with the formation of the dual upper-tropospheric jet streaks at 0000 UTC 14 August (Fig. 4.4b). There is a decrease in the vertical tilt between the upstream TPV and AC16 during 1200 UTC 13–0000 UTC 15 August (Figs. 4.5a–d) as AC16 intensifies, which is reproduced by QG theory for midlatitude cyclones (e.g., Martin 2006, section 8.8). The upstream TPV becomes vertically superposed with AC16 during 1200 UTC 15–0000 UTC 16 August (Figs. 4.5e,f) as AC16 reaches peak intensity, suggesting that AC16 becomes equivalent barotropic in structure. Yamagami et al. (2017) similarly show that a TPV upstream of AC16 gradually approaches AC16 and becomes vertically superposed with AC16. The upstream TPV likely plays an important role in the development and intensification of AC16.

Figures 4.5a–d also show that there are regions of lower-to-midtropospheric ascent and upper-tropospheric divergence in the vicinity of AC16 during 1200 UTC 13–0000 UTC 15 August. Furthermore, there is a “starburst” irrotational wind pattern during 1200 UTC 13–0000 UTC 15 August (Figs. 4.5a–d), which is especially well-defined at 0000 UTC 14 August (Fig. 4.5b). The “starburst” irrotational wind pattern may be a manifestation of latent heating. Figure 4.6a indicates that there is an IVT corridor southeast of AC16 at 1200 UTC 13 August. The IVT

corridor may be a manifestation of a WCB associated with AC16. Associated with the IVT corridor are regions of IMFC indicative of latent heating southeast and east of AC16 (Fig. 4.6a). By 0000 UTC 14 August, the IVT corridor strengthens east of AC16 and IMFC increases markedly northeast of AC16 (Fig. 4.6b). The region of IMFC northeast of AC16 at 0000 UTC 14 August (Fig. 4.6b) coincides with well-defined regions of lower-to-midtropospheric accent and upper-tropospheric divergence (Fig. 4.5b), and with the well-defined "starburst" irrotational wind pattern (Fig. 4.5b), at this time. The latent heating likely contributes to the development and intensification of AC16. The IVT corridor and associated regions of IMFC persist and gradually weaken during 1200 UTC 14–0000 UTC 16 August (Figs. 4.6c–f).

The development and intensification of AC16 appear to be influenced by a TPV, TPV–AC interactions, baroclinic processes, an IVT corridor, and latent heating. The sensitivity of the forecast skill of the intensity and position of AC16 to selected dynamic and thermodynamic quantities will next be examined to help determine what features and processes may influence the forecast skill of the intensity and position of AC16.

2) ESA results

In this section, the sensitivity of J_{AC} to selected dynamic and thermodynamic quantities is presented. All sensitivity values are multiplied by −1, such that positive sensitivity values indicate that increasing the value of the quantity is associated with a decrease in J_{AC}. Since J_{AC} is correlated with the intensity error and position error of AC16 at 0000 UTC 15 August (120 h), lower values of J_{AC} are associated with a more accurate prediction of the intensity and position of AC16 at 0000 UTC 15 August (120 h). Negative sensitivity values indicate that decreasing the value of the quantity is associated with a decrease in J_{AC} and thus associated with a more

accurate prediction of the intensity and position of AC16 at 0000 UTC 15 August (120 h). Accordingly, a more accurate prediction of the intensity and position of AC16 at 0000 UTC 15 August (120 h) is associated with increasing the value of the quantity for positive sensitivity values and with decreasing the value of the quantity for negative sensitivity values. Refer to Fig. 1.1 for a map of geographic features that are discussed throughout the rest of this chapter.

The sensitivity of the prediction of AC16 to upper-tropospheric features is first determined by examining the sensitivity of J_{AC} to upper-tropospheric PV. During 0000 UTC 10–1200 UTC 11 August (0–36 h), a region of negative sensitivity of J_{AC} to upper-tropospheric PV propagates southeastward from just northeast of Iceland to southwestern Scandinavia, between an upper-tropospheric ridge (R1) over the North Atlantic and an upper-tropospheric trough (T1) over the Norwegian Sea and western Eurasia (Figs. 4.7a–d). The region of negative sensitivity of J_{AC} to upper-tropospheric PV suggests that shifting R1 slightly farther east during 0000 UTC 10–1200 UTC 11 August (0–36 h) is associated with a more accurate prediction of AC16.

At 0000 UTC 12 August (48 h), the region of negative sensitivity of J_{AC} to upper-tropospheric PV persists between R1 and T1 over northern Europe (Fig. 4.8a). Also at 0000 UTC 12 August (48 h), a region of positive sensitivity of J_{AC} to upper-tropospheric PV becomes established over portions of Scandinavia and northwestern Russia, within and on the eastern side of T1 (Fig. 4.8a). By 1200 UTC 12 August (60 h), the aforementioned regions of negative and positive sensitivity of J_{AC} to upper-tropospheric PV grow in size and magnitude (Fig. 4.8b). The aforementioned region of positive sensitivity of J_{AC} to upper-tropospheric PV during 0000–1200 UTC 12 August (48–60 h) suggests that a slightly stronger and slightly more amplified T1 over Scandinavia and northwestern Russia during this period is associated with a more accurate prediction of AC16. Embedded within T1 is the TPV located upstream of AC16 that was

discussed in section 4c(1). The TPV is suggested by the high values of upper-tropospheric PV within T1 in Figs. 4.8a,b, though the TPV is not directly identifiable in Figs. 4.8a,b due to composite smoothing. A slightly stronger T1 is likely associated with a slightly stronger TPV. A new region of negative sensitivity of J_{AC} to upper-tropospheric PV becomes established during 0000–1200 UTC 12 August (48–60 h) near the crest of an upper-tropospheric ridge (R2) located downstream of T1 (Figs. 4.8a,b). The new region of negative sensitivity of J_{AC} to upper-tropospheric PV suggests that a slightly more amplified R2 during 0000–1200 UTC 12 August (48–60 h) is associated with a more accurate prediction of AC16.

During 0000 UTC 13–1200 UTC 14 August (72–108 h), the aforementioned region of positive sensitivity of J_{AC} to upper-tropospheric PV increases in size and becomes relatively large in magnitude within and on southeastern side of T1, which propagates east-northeastward from Scandinavia (Figs. 4.8c–f). Also during 0000 UTC 13–1200 UTC 14 August (72–108 h), the region of negative sensitivity of J_{AC} to upper-tropospheric PV at the crest of R2 grows in size and magnitude as R2 amplifies (Figs. 4.8c–f). The aforementioned regions of positive and negative sensitivity of J_{AC} to upper-tropospheric PV during 0000 UTC 13–1200 UTC 14 Aug (72–108 h) suggest that a farther southeastward positioned and more amplified T1, and a more amplified R2, are associated with a more accurate prediction of AC16.

Since upper-tropospheric features can have a large influence on surface features, the sensitivity of J_{AC} to SLP will now be examined. During 0000–1200 UTC 12 Aug (48–60 h), a region of negative sensitivity of J_{AC} to SLP increases rapidly in magnitude over Scandinavia and northwestern Russia, in a broad region of relatively low SLP (Figs. 4.9a,b). The region of negative sensitivity of J_{AC} to SLP increases in magnitude and size during 0000 UTC 13–1200 UTC 14 August (72–108 h) in a region of low SLP that corresponds to AC16 (Figs. 4.9c–f). The

region of negative sensitivity of J_{AC} to SLP during 0000 UTC 13–1200 UTC 14 August (72–108 h) (Figs. 4.9c–f) suggests that a stronger AC16 during this period is associated with a more accurate prediction of AC16. The region of negative sensitivity of J_{AC} to SLP during 0000 UTC 13–1200 UTC 14 August (72–108 h) (Figs. 4.9c–f) is positioned between the regions of positive and negative sensitivity of J_{AC} to upper-tropospheric PV associated with T1 and R2, respectively, during this period (Figs. 4.8c–f). It is speculated from the aforementioned sensitivity patterns in Figs. 4.8c–f and Figs. 4.9c–f that a more amplified T1 and R2 may be associated with a stronger AC16 during 0000 UTC 13–1200 UTC 14 August (72–108 h).

As discussed in section 4c(1), latent heating likely contributes to the development and intensification of AC16. The sensitivity of J_{AC} to 850-hPa specific humidity and to lower-tropospheric IMFC indicative of latent heating will now be examined. At 0000 UTC 13 August (72 h), there is a small region of positive sensitivity of J_{AC} to 850-hPa specific humidity over and near Novaya Zemlya, on the northwestern flank of a moisture corridor extending from western Russia into the Kara Sea (Fig. 4.10a). There is also a region of lower-tropospheric IMFC indicative of latent heating on the northern flank of this moisture corridor (Fig. 4.11a), with a small region of positive sensitivity of J_{AC} to lower-tropospheric IMFC coinciding with a region of lower-tropospheric IMFC over and near Novaya Zemlya (Fig. 4.11a). During 1200 UTC 13–1200 UTC 14 August (84–108 h), the moisture corridor shifts northeastward (Figs. 4.10b–d), and the region of positive sensitivity of J_{AC} to 850-hPa specific humidity increases in size and magnitude on the northwestern flank of the moisture corridor (Figs. 4.10b–d). The region of positive sensitivity of J_{AC} to lower-tropospheric IMFC concomitantly increases in size and magnitude on the northwestern flank of a region of lower-to-midtropospheric IMFC during 1200 UTC 13–1200 UTC 14 August (84–108 h) (Figs. 4.11b–d).

The aforementioned region of positive sensitivity of J_{AC} to 850-hPa specific humidity during 0000 UTC 13–1200 UTC 14 August (72–108 h) (Figs. 4.10a–d) is located on the northwestern flank of the moisture corridor during this period and does not coincide with areas of relatively high values of 850-hPa specific humidity associated with the moisture corridor during this period. Therefore, the aforementioned region of positive sensitivity of J_{AC} to 850-hPa specific humidity during 0000 UTC 13–1200 UTC 14 August (72–108 h) (Figs. 4.10a–d) suggests that a northwestward shift of the moisture corridor during this period is associated with a more accurate prediction of AC16, but does not suggest that an increase in the amount of moisture within the moisture corridor during this period is associated with a more accurate prediction of AC16.

The aforementioned region of positive sensitivity of J_{AC} to lower-tropospheric IMFC at 0000 UTC 13 August (72 h) (Fig. 4.11a) coincides with areas of relatively high values of latent heating associated with the region of latent heating over and near Novaya Zemlya at this time, suggesting that increasing the magnitude of latent heating at this time is associated with a more accurate prediction of AC16. However, the aforementioned region of positive sensitivity of J_{AC} to lower-tropospheric IMFC during 1200 UTC 13–1200 UTC 14 August (84–108 h) (Figs. 4.11b–d) is located on the northwestern flank of the region of latent heating during this period and does not coincide with areas of relatively high values of latent heating associated with the region of latent heating during this period. Therefore, the aforementioned region of positive sensitivity of J_{AC} to lower-tropospheric IMFC during 1200 UTC 13–1200 UTC 14 August (84–108 h) (Figs. 4.11b–d) suggests that a northwestward shift in the region of latent heating during this period is associated with a more accurate prediction of AC16, but does not suggest that an increase in the magnitude of latent heating during this period is associated with a more accurate

prediction of AC16. It is speculated that the position of the moisture corridor and the position of the region of latent heating may matter more to the predictability of AC16 than the amount of moisture in the moisture corridor and the magnitude of latent heating.

The following discussion is conjecture based on the ESA results. Future work is needed to validate the points made in the following discussion. A slightly more eastward shifted R1 building into western Eurasia during 0000 UTC 10–0000 UTC 12 August (0–48 h) may be associated with a more amplified and stronger T1, and a stronger embedded TPV, over Scandinavia and northwestern Russia by 1200 UTC 12 August (60 h). The more amplified and stronger T1, and the stronger embedded TPV, may be associated with greater development of AC16 and greater downstream upper-tropospheric flow amplification by 0000 UTC 13 August (72 h). There then may be a positive feedback between the intensification of AC16 and the amplification of the downstream upper-tropospheric flow during 0000 UTC 13–1200 UTC 14 August (72–108 h), with an increasingly stronger AC16 being associated with an increasingly amplified downstream upper-tropospheric flow during this period. A stronger lower-tropospheric circulation associated with a stronger AC16 during 0000 UTC 13–1200 UTC 14 August (72–108 h) may contribute to a northwestward shift in the moisture corridor and region of latent heating in the vicinity of AC16.

It is speculated that forecasts errors in T1 and the embedded TPV, and forecast errors in other upper-tropospheric features, may contribute to forecast errors in AC16. Previous studies, including Yamagami et al. (2018a) and Johnson and Wang (2021), suggest that forecast errors in TPVs and other upper-tropospheric features can contribute to forecast errors in ACs. Yamagami et al. (2018a) show via a composite comparison between most-accurate and least-accurate ensemble forecasts of AC12 that accurate prediction of AC12 depends on accurate prediction of

TPVs, an upper-tropospheric trough, and an upper-tropospheric ridge, in the vicinity of AC12. Johnson and Wang (2021) find that track error and intensity error of an AC occurring during July 2018 are sensitive to the position and intensity of TPVs, and to the amplitude of a midtropospheric ridge downstream of the AC. Johnson and Wang (2021) also find that intensity error of the AC occurring during July 2018 is sensitive to the amount of midtropospheric moisture within a moisture corridor associated with the AC. In the present study, it is speculated that the predictability of AC16 may be more sensitive to the position of the moisture corridor influencing AC16 than to the amount of moisture within the moisture corridor influencing AC16.

Past studies of midlatitude cyclones have shown that forecast errors in the intensity and position of midlatitude cyclones can be linked to forecast errors in upper-tropospheric features, such as upper-tropospheric troughs and ridges (e.g., Sanders 1986, 1992; Kuo and Reed 1988; Sanders et al. 2000; Langland et al. 2002; Chang et al. 2013; Zheng et al. 2013; Lamberson et al. 2016). Furthermore, previous studies including Langland et al. (2002), Chang et al. (2013), and Lamberson et al. (2016) show that upper-tropospheric forecast errors influencing the forecast skill of midlatitude cyclones can propagate downstream as structures resembling wave packets. The propagation of coherent regions of sensitivity of J_{AC} to upper-tropospheric PV from the North Atlantic, across Eurasia, and into the Arctic during 0000 UTC 10–1200 UTC 14 August (Figs. 4.7a–d and Figs. 4.8a–f) suggests that upper-tropospheric forecast errors influencing the forecast skill of AC16 may similarly propagate downstream as structures resembling wave packets. The aforementioned hypothesized propagation of upper-tropospheric forecast errors in Figs. 4.7a–d and Figs. 4.8a–f suggests that upper-tropospheric forecast errors influencing the forecast skill of ACs like AC16 may originate well upstream of the ACs.

3) Comparison between most-accurate and least-accurate ensemble forecasts

Earth-relative composites of selected dynamic and thermodynamic quantities are constructed for the most-accurate and least-accurate ensemble forecasts for AC16 (forecasts shown in Figs. 4.3a,b) to compare the evolution of features and processes influencing AC16 between these respective categories of forecasts and to expand upon the ESA results. There is variability in the positions of AC16 among the most-accurate ensemble forecasts and among the least-accurate ensemble forecasts (Fig. 4.3a), such that composite smoothing occurs. Therefore, selected dynamic and thermodynamic quantities that are representative of features and processes influencing AC16 are area-averaged within a 1000-km radius from the center of AC16 for each forecast in order to compare these quantities between the most-accurate and least-accurate ensemble forecasts without needing to account for composite smoothing. A bootstrap resampling without replacement test following the second procedure described in section 2b(5) is used to determine whether there are statistically significant differences in the area-averaged quantities between the most-accurate and least-accurate ensemble forecasts.

The influence of baroclinic processes on the development and intensification of AC16 for the most-accurate and least-accurate ensemble forecasts is first examined. At 0000 UTC 13 August (72 h), an area of low SLP corresponding to AC16 is found over the Barents Sea within a region of strong lower-to-midtropospheric baroclinicity and beneath a strong upper-tropospheric jet streak in both the most-accurate ensemble forecasts (Fig. 4.12a) and least-accurate ensemble forecasts (Fig. 4.12b). The strength of the lower-to-midtropospheric baroclinicity appears to be comparable between the most-accurate ensemble forecasts (Fig. 4.12a) and least-accurate ensemble forecasts (Fig. 4.12b). In contrast, the area of low SLP corresponding to AC16 is

stronger and found between a more amplified thickness trough and ridge in the most-accurate ensemble forecasts (Fig. 4.12a) compared to the least-accurate ensemble forecasts (Fig. 4.12b).

At 0000 UTC 14 August (96 h), the area of low SLP corresponding to AC16 intensifies rapidly between an amplifying thickness trough and ridge in the most-accurate ensemble forecasts (Fig. 4.12c). Furthermore, the strong upper-tropospheric jet streak at 0000 UTC 13 August (72 h) (Fig. 4.12a) appears to evolve into dual upper-tropospheric jet streaks by 0000 UTC 14 August (96 h) (Fig. 4.12c) in the most-accurate ensemble forecasts, with AC16 intensifying in a region of apparent upper-tropospheric jet coupling. The formation of the dual upper-tropospheric jet streaks is likely related to the reconfiguration of the region of strong lower-to-midtropospheric baroclinicity in the vicinity of AC16 during 0000 UTC 13–0000 UTC 14 August (72–96 h) (Figs. 4.12a,c), which likely occurs partly in response to lower-to-midtropospheric thermal advection in the vicinity of AC16. There is no coherent area of low SLP corresponding to AC16 at 0000 UTC 14 August (96 h) in the least-accurate ensemble forecasts (Fig. 4.12d), which is partially due to composite smoothing associated with the variability of the positions of AC16 among the least-accurate ensemble forecasts. The strength of the lower-to-midtropospheric baroclinicity still appears to be comparable between the most-accurate ensemble forecasts (Fig. 4.12c) and least-accurate ensemble forecasts (Fig. 4.12d) at 0000 UTC 14 August (96 h). However, there is only a low-amplitude thickness trough and ridge over and near northern Eurasia, and a relatively flat upper-tropospheric jet streak over and near the northern Eurasian coast, in the least-accurate ensemble forecasts at 0000 UTC 14 August (96 h) (Fig. 4.12d).

Based on Sutcliffe development theory, cyclogenesis is favored between a thickness trough and ridge, in response to the advection of thermal vorticity by the thermal wind (e.g., Carlson 1998, section 8.1). Given that there is a more amplified thickness trough and ridge in the

vicinity of AC16 in the most-accurate ensemble forecasts (Fig. 4.12c) compared to the least-accurate ensemble forecasts (Fig. 4.12d), it is hypothesized that there may be greater advection of thermal vorticity by the thermal wind between the thickness trough and ridge that contributes to the greater intensification of AC16 in the most-accurate ensemble forecasts. At 0000 UTC 15 August (120 h), the area of low SLP corresponding to AC16 is found in the poleward exit region of a cyclonically curved upper-tropospheric jet streak in the most-accurate ensemble forecasts (Fig. 4.12e), and there continues to be no coherent area of low SLP corresponding to AC16 in the least-accurate ensemble forecasts (Fig. 4.12f).

The ESA suggested that a more amplified T1 and a more amplified R2 are associated with a more accurate prediction of AC16. At 0000 UTC 13 August (72 h), T1 and R2 are more amplified over northwestern Eurasia and the adjacent Arctic in the most-accurate ensemble forecasts (Fig. 4.13a) compared to the least-accurate ensemble forecasts (Fig. 4.13b). Embedded within T1 is the TPV located upstream of AC16 that was discussed in section 4c(1). The TPV is suggested by the high values of upper-tropospheric PV within T1 in Figs. 4.13a,b, though the TPV is not directly identifiable in Figs. 4.13a,b due to composite smoothing. T1 is characterized by higher values of upper-tropospheric PV in the most-accurate ensemble forecasts (Fig. 4.13a) compared to the least-accurate ensemble forecasts (Fig. 4.13b), suggesting that there may be a stronger TPV embedded in T1 in the most-accurate ensemble forecasts. Between the more amplified T1 and R2 is a region of much stronger upper-tropospheric divergence and irrotational outflow in the most-accurate ensemble forecasts (Fig. 4.13a) compared to the least-accurate ensemble forecasts (Fig. 4.13b). The much stronger upper-tropospheric divergence and irrotational outflow likely contribute to the greater development and intensification of AC16 in the most-accurate ensemble forecasts.

By 0000 UTC 14 August (96 h), R2 amplifies over Eurasia and the adjacent Arctic in the most-accurate ensemble forecasts (Fig. 4.13c), but is relatively flat over Eurasia in the least-accurate ensemble forecasts (Fig. 4.13d). There continues to be a region of much stronger upper-tropospheric divergence and irrotational outflow in the most-accurate ensemble forecasts (Fig. 4.13c) compared to the least-accurate ensemble forecasts (Fig. 4.13d). By 0000 UTC 15 August (120 h), R2 remains more amplified in the most-accurate ensemble forecasts (Fig. 4.13e) compared to the least-accurate ensemble forecasts (Fig. 4.13f).

The stronger upper-tropospheric irrotational outflow in the most-accurate ensemble forecasts suggests that there is greater latent heating in the most-accurate ensemble forecasts. At 0000 UTC 13 August (72 h), there is a lower-tropospheric IVT corridor over western Russia that is of comparable magnitude between the most-accurate ensemble forecasts (Fig. 4.14a) and least-accurate ensemble forecasts (Fig. 4.14b). However, the lower-tropospheric IVT corridor is more poleward directed in the most-accurate ensemble forecasts (Fig. 4.14a) compared to the least-accurate ensemble forecasts (Fig. 4.14b). There is also greater lower-tropospheric IMFC indicative of greater latent heating over and near Novaya Zemlya, near the developing AC16, in the most-accurate ensemble forecasts (Fig. 4.14a) compared to the least-accurate ensemble forecasts (Fig. 4.14b). The greater lower-tropospheric IMFC over and near Novaya Zemlya in the most-accurate ensemble forecasts likely relates to the stronger lower-tropospheric IVT over and near Novaya Zemlya in the most-accurate ensemble forecasts (Fig. 4.14a) compared to the least-accurate ensemble forecasts (Fig. 4.14b). The greater lower-tropospheric IMFC over and near Novaya Zemlya in the most-accurate ensemble forecasts may also relate to greater upper-tropospheric dynamical forcing that may be associated with the stronger TPV embedded in T1 in

the most-accurate ensemble forecasts (Fig. 4.13a) compared to the least-accurate ensemble forecasts (Fig. 4.13b).

By 0000 UTC 14 August (96 h), there is a stronger and more northwestward positioned corridor of IVT, and a region of larger lower-tropospheric IMFC indicative of greater latent heating, in the most-accurate ensemble forecasts (Fig. 4.14c) compared to the least-accurate ensemble forecasts (Fig. 4.14d). By 0000 UTC 15 August (120 h), the lower-tropospheric IVT corridor and associated regions of lower-tropospheric IMFC weaken considerably in both the most-accurate ensemble forecasts (Fig. 4.14e) and least-accurate ensemble forecasts (Fig. 4.14f).

Figure 4.15a shows that the mean value of area-averaged lower-to-midtropospheric Eady growth rate at 0000 UTC 14 August (96 h) is larger for the most-accurate ensemble forecasts ($0.85\ \text{day}^{-1}$) compared to the least-accurate ensemble forecasts ($0.81\ \text{day}^{-1}$), but that the difference between these mean values is not statistically significant. Therefore, AC16 intensifies in regions of comparable lower-to-midtropospheric Eady growth rates in the most-accurate and least-accurate ensemble forecasts. The comparable lower-to-midtropospheric Eady growth rates are likely related to the comparable strength of lower-to-midtropospheric baroclinicity between the most-accurate ensemble forecasts (Fig. 4.12c) and least-accurate ensemble forecasts (Fig. 4.12d) at 0000 UTC 14 August (96 h). Figure 4.15b indicates that the mean value of area-averaged upper-tropospheric PV at 0000 UTC 14 August (96 h) is statistically significantly larger for the most-accurate ensemble forecasts (8.6 PVU) compared to the least-accurate ensemble forecasts (8.0 PVU). Similarly, Fig. 4.15c indicates that the mean value of area-averaged 500-hPa relative vorticity at 0000 UTC 14 August (96 h) is statistically significantly larger for the most-accurate ensemble forecasts ($6.0 \times 10^{-5}\ \text{s}^{-1}$) compared to the least-accurate ensemble forecasts ($5.0 \times 10^{-5}\ \text{s}^{-1}$). The statistically significantly larger area-averaged upper-

tropospheric PV and statistically significantly larger area-averaged 500-hPa relative vorticity for the most-accurate ensemble forecasts suggest that the TPV embedded in T1 is stronger for the most-accurate ensemble forecasts. A stronger TPV embedded in T1 in the most-accurate ensemble forecasts may be associated with stronger TPV–AC interactions that support the greater intensification of AC16 in the most-accurate ensemble forecasts.

Figure 4.15d shows that the mean value of area-averaged 300-hPa irrotational wind speed at 0000 UTC 14 August (96 h) is statistically significantly larger for the most-accurate ensemble forecasts (3.0 m s^{-1}) compared to the least-accurate ensemble forecasts (2.3 m s^{-1}). The mean value of area-averaged lower-tropospheric IVT at 0000 UTC 14 August (96 h) is also statistically significantly larger for the most-accurate ensemble forecasts (97 kg m^{-1} s^{-1}) compared to the least-accurate ensemble forecasts (84 kg m^{-1} s^{-1}) (Fig. 4.15e). The statistically significantly larger area-averaged 300-hPa irrotational wind speed and statistically significantly larger area-averaged lower-tropospheric IVT for the most-accurate ensemble forecasts suggest that there may be statistically significantly greater latent heating for the most-accurate ensemble forecasts. However, the mean value of area-averaged lower-tropospheric IMFC at 0000 UTC 14 August (96 h) is only slightly larger for the most-accurate ensemble forecasts (465 W m^{-2}) compared to the least-accurate ensemble forecasts (433 W m^{-2}), suggesting that latent heating is comparable between the most-accurate and least-accurate ensemble forecasts. Therefore, there are mixed signals as to whether there are statistically significant differences in latent heating between the most-accurate and least-accurate ensemble forecasts.

It is possible that area-averaged IVT may be larger for the most-accurate ensemble forecasts due to the presence of a more widespread region of relatively high values of IVT in the vicinity of AC16 in the most-accurate ensemble forecasts. It is possible that the maximum

magnitude of IVT may be comparable between the most-accurate and least-accurate ensemble forecasts. The maximum value of IVT within a 1000-km radius from the center of AC16 for each of the most-accurate and least-accurate ensemble forecasts is determined at 0000 UTC 14 August (96 h). The mean maximum value of IVT is only slightly larger for the most-accurate ensemble forecasts (322 kg m^{-1} s^{-1}) compared to the least-accurate ensemble forecasts (304 kg m^{-1} s^{-1}) (not shown), and the difference between the mean values are not statistically significant. IVT being of comparable maximum magnitude between the most-accurate and least-accurate ensemble forecasts may help explain the comparable lower-tropospheric IMFC between the most-accurate and least-accurate ensemble forecasts.

It is hypothesized from the foregoing analyses of the most-accurate and least-accurate ensemble forecasts that the amplitude and strength of T1, and the strength of an embedded TPV, upstream of AC16 may be an important distinction between these respective categories of forecasts. There are comparable lower-to-midtropospheric baroclinicity and comparable lower-to-midtropospheric Eady growth rates in the vicinity of AC16 between the most-accurate and least-accurate ensemble forecasts. However, it is speculated that the more amplified and stronger T1, and stronger embedded TPV, in the most-accurate ensemble forecasts may contribute to greater baroclinic growth of AC16 and to greater downstream upper-tropospheric flow amplification in the most-accurate ensemble forecasts. It is also speculated that large differences in the amplitude and position of the thickness trough and ridge in the vicinity of AC16 between the most-accurate and least-accurate ensemble forecasts may be indicative of large differences in the positions of warm and cold frontal zones associated with AC16 between these respective categories of forecasts.

Although there are mixed signals as to whether there is greater latent heating in the vicinity of AC16 in the most-accurate ensemble forecasts, there is a more poleward directed and more northwestward positioned lower-tropospheric IVT corridor, and much stronger upper-tropospheric irrotational outflow, in the vicinity of AC16 in the most-accurate ensemble forecasts. The stronger lower-tropospheric circulation associated with the more intense AC16 helps transport moisture farther northwestward in the most-accurate ensemble forecasts. The stronger upper-tropospheric irrotational outflow likely contributes to the greater intensification of AC16 in the most-accurate ensemble forecasts.

d. Summary

In this chapter, features and processes influencing the forecast skill of AC16 were determined by conducting an ESA of AC16 and by comparing the most-accurate and least-accurate ensemble forecasts of AC16. The ESA and the comparison of forecasts served as a basis to address hypothesis 5. Hypothesis 5 states that forecast errors in TPVs, baroclinic zones, and WCBs, and forecast errors in TPV–AC interactions, baroclinic processes, and latent heating, contribute to forecast errors in strong low-skill ACs during low-skill periods. Based on the ESA and the comparison of forecasts, the extent to which hypothesis 5 may be supported is unknown, such that future work is required to address hypothesis 5. A summary of the most noteworthy findings is given below.

- The ESA suggests that the prediction of AC16 is sensitive to the amplitude and strength of T1, and to the strength of an embedded TPV, upstream of AC16. It is speculated from the ESA and the comparison of forecasts that a more amplified and stronger T1, and a

stronger embedded TPV, upstream of AC16 are associated with greater downstream upper-tropospheric flow amplification and greater intensification of AC16.

- The comparison of forecasts suggests that there are comparable lower-to-midtropospheric baroclinicity and comparable lower-to-midtropospheric Eady growth rates in the vicinity of AC16 between the most-accurate and least-accurate ensemble forecasts. However, there are large differences in the amplitude and position of a thickness trough and ridge in the vicinity of AC16 between the most-accurate and least-accurate ensemble forecasts. Given that there is a more amplified thickness trough and ridge in the vicinity of AC16 in the most-accurate ensemble forecasts compared to the least-accurate ensemble forecasts, it is hypothesized that there may be greater advection of thermal vorticity by the thermal wind between the thickness trough and ridge that contributes to the greater intensification of AC16 in the most-accurate ensemble forecasts.
- The ESA and the comparison of forecasts suggest that a northwestward shift in a moisture corridor and region of latent heating in the vicinity of AC16 is associated with a more accurate prediction of AC16. There are mixed signals as to whether greater latent heating is associated with a more accurate prediction of AC16.

e. Figures

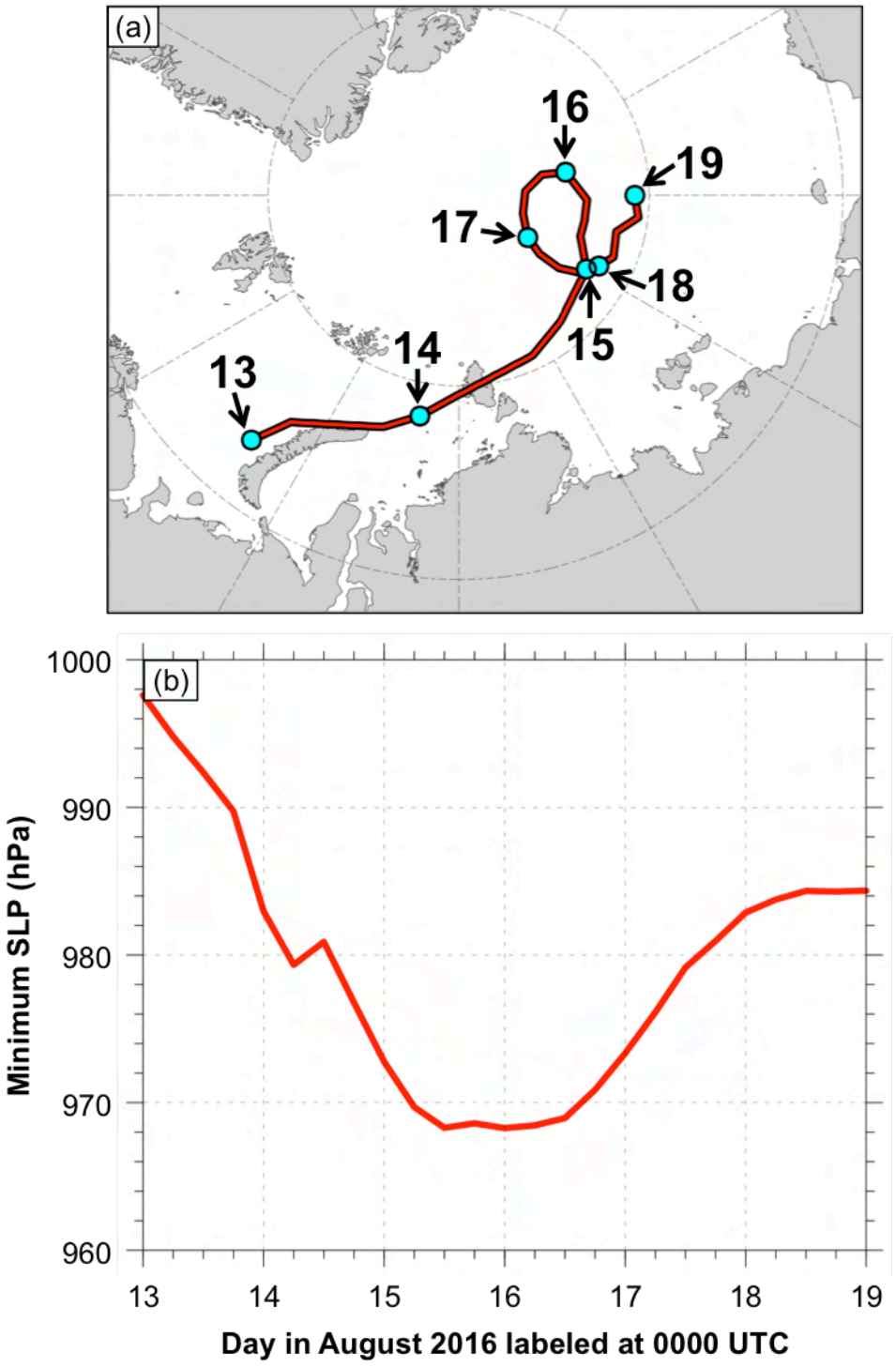

Fig. 4.1. (a) Track (red line) and (b) minimum SLP (red line) of AC16 during 0000 UTC 13–0000 UTC 19 August 2016, every 6 h. Cyan dots in (a) indicate 0000 UTC positions of AC16.

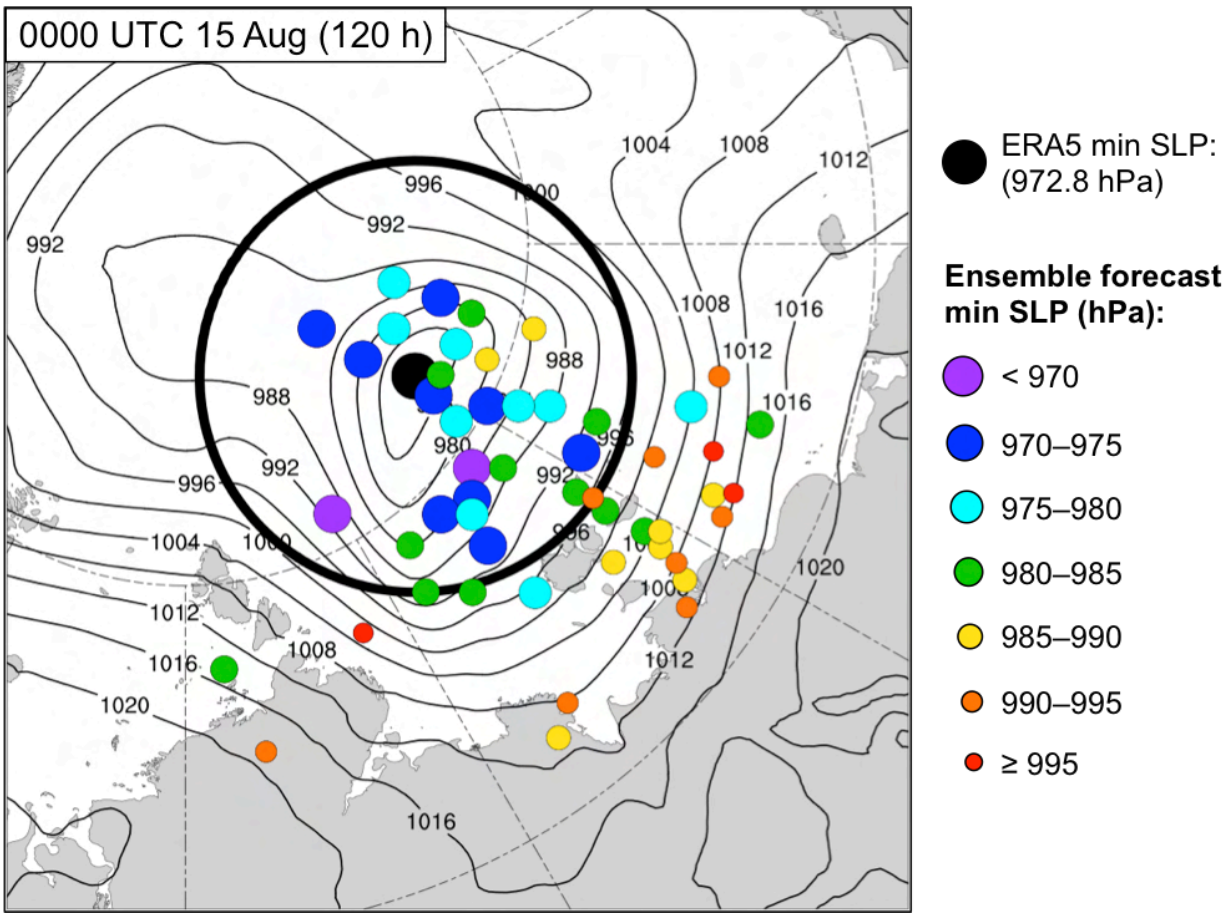

Fig. 4.2. Positions of AC16 for the ensemble forecasts (colored dots; $N = 51$) at 0000 UTC 15 August (120 h). Dots are colored and sized by minimum SLP (hPa) at 0000 UTC 15 August (120 h) according to the legend. The position of AC16 for ERA5 at 0000 UTC 15 August is given by the black dot. The corresponding minimum SLP of AC16 for ERA5 is 972.8 hPa. Black contours denote SLP (hPa) from ERA5 at 0000 UTC 15 August. Black circle of 700-km radius denotes region over which J_{AC} is calculated.

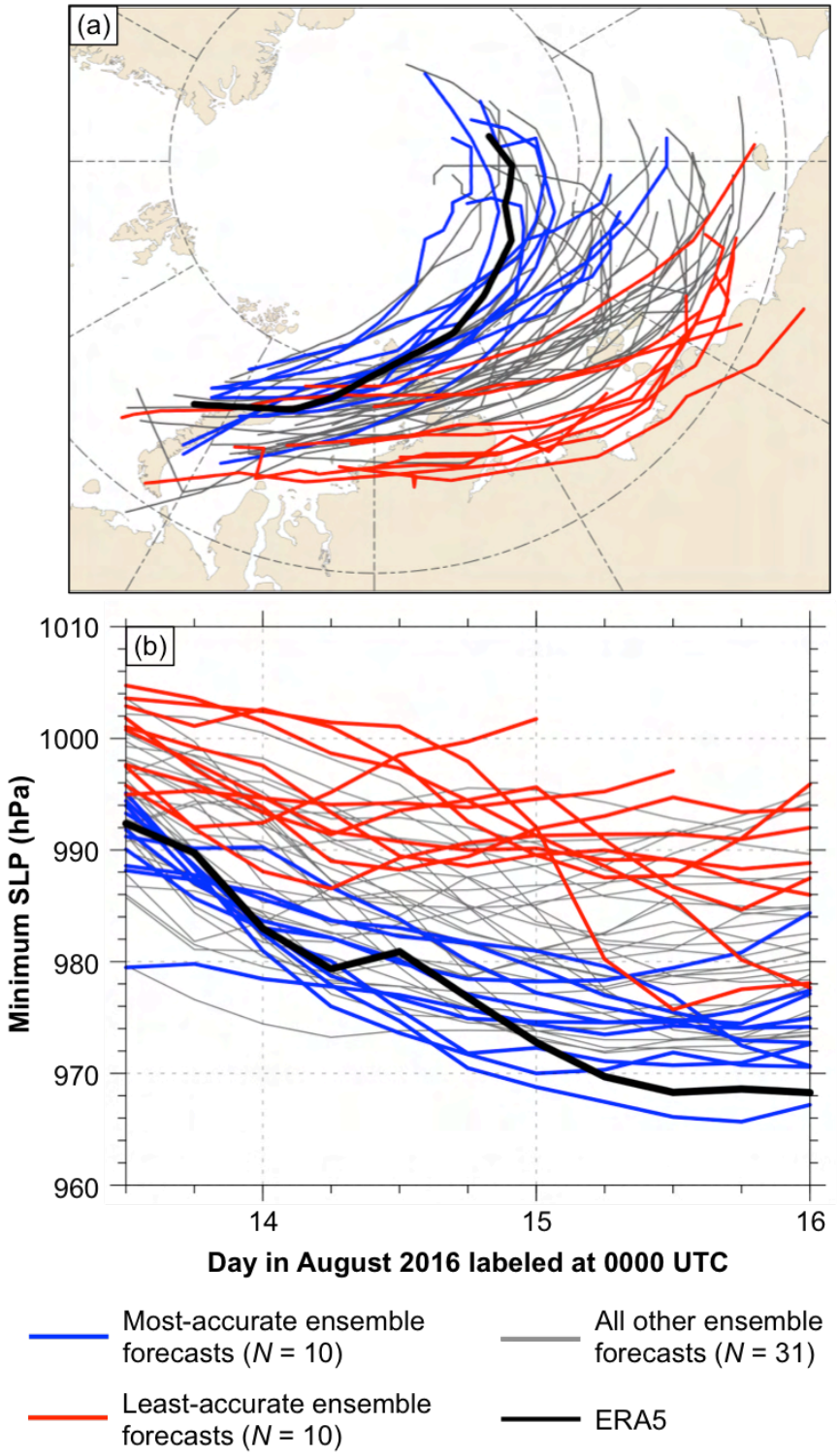

Fig. 4.3. (a) Tracks and (b) minimum SLP (hPa) during 1200 UTC 13–0000 UTC 16 August, every 6 h, for most-accurate ensemble forecasts (blue), least-accurate ensemble forecasts (red), all other ensemble forecasts (gray), and ERA5 (black).

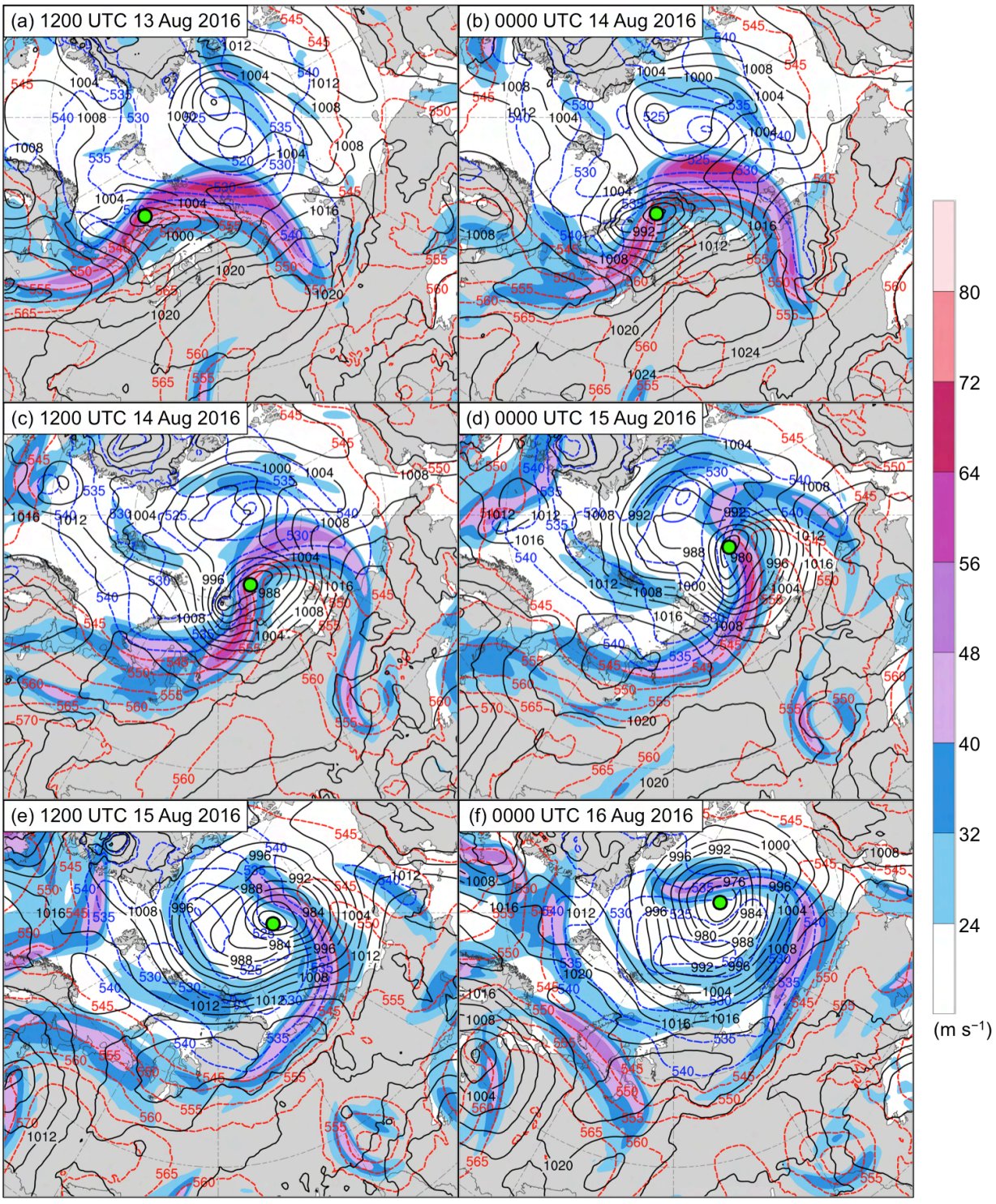

Fig. 4.4. ERA5 analyses of 300-hPa wind speed (m s^{-1}; shading), 1000–500-hPa thickness (dam; dashed red and blue contours), and SLP (hPa; black contours) at (a) 1200 UTC 13 August, (b) 0000 UTC 14 August, (c) 1200 UTC 14 August, (d) 0000 UTC 15 August, (e) 1200 UTC 15 August, and (f) 0000 UTC 16 August. The green dot shows the location of AC16.

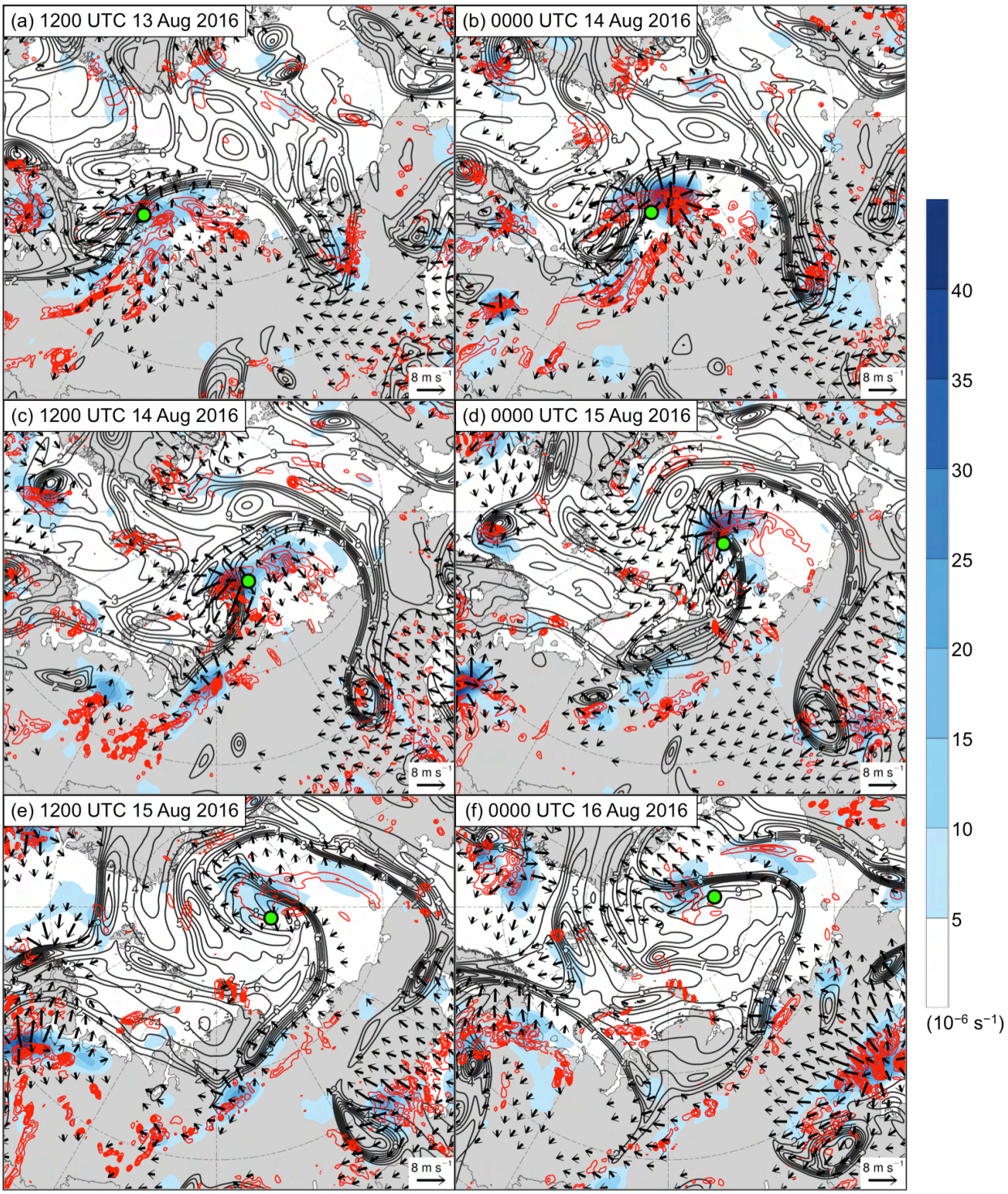

Fig. 4.5. As in Fig. 4.4, but for ERA5 analyses of 350–250-hPa divergence area averaged within 200 km of each grid point (10^{-6} s^{-1}; shading), 350–250-hPa irrotational wind (m s^{-1}; vectors), 350–250-hPa PV (PVU; dark gray contours), and negative values of 800–600-hPa ω (every 1 × 10^{-3} hPa s^{-1}; red contours). The green dot shows the location of AC16.

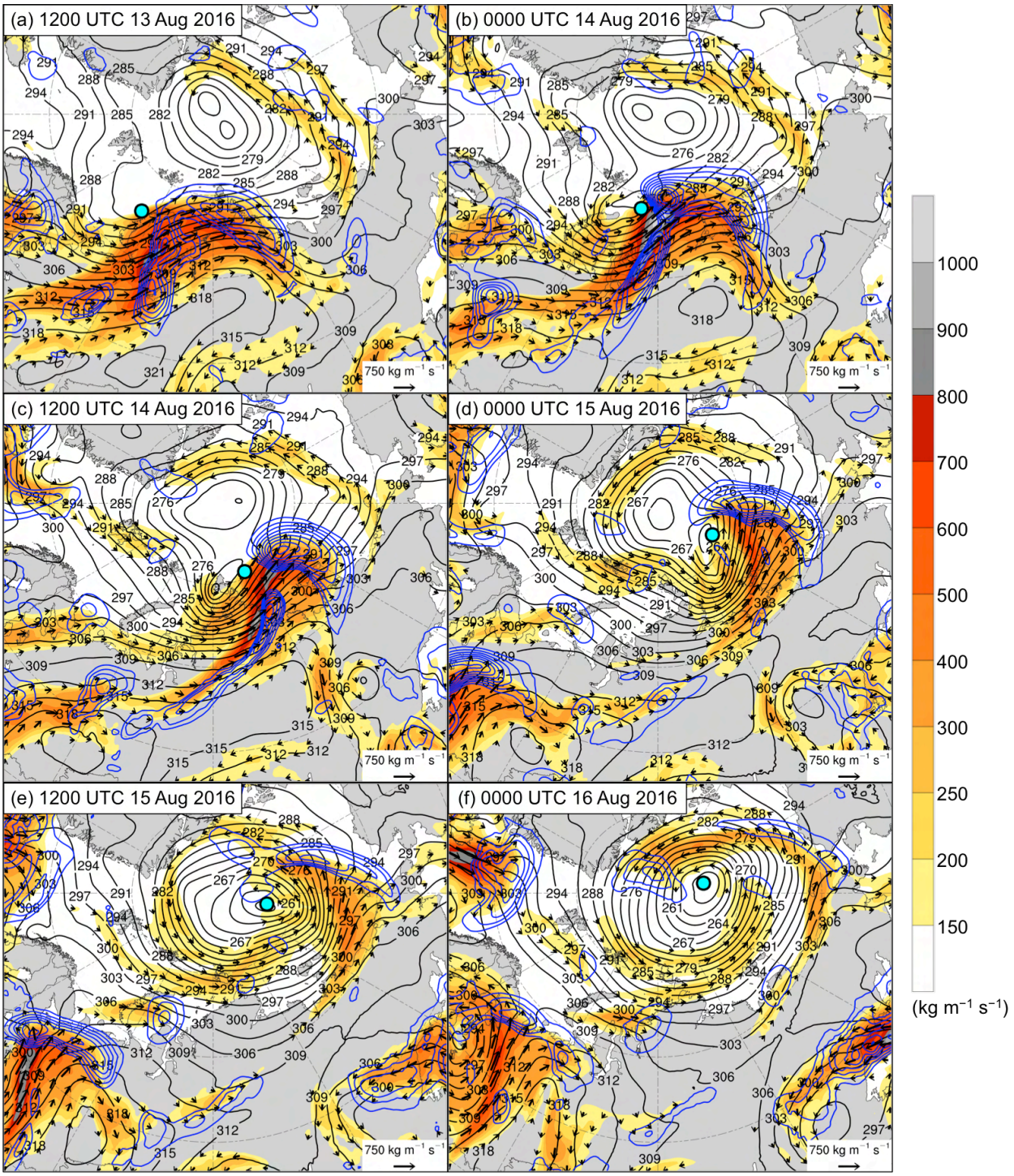

Fig. 4.6. As in Fig. 4.4, but for ERA5 analyses of 1000–300-hPa IVT (kg m^{-1} s^{-1}; shading and vectors), positive values of 1000–300-hPa IMFC area averaged within 200 km of each grid point (every 250 W m^{-2}; blue contours), and 700-hPa geopotential height (dam; black contours). The cyan dot shows the location of AC16.

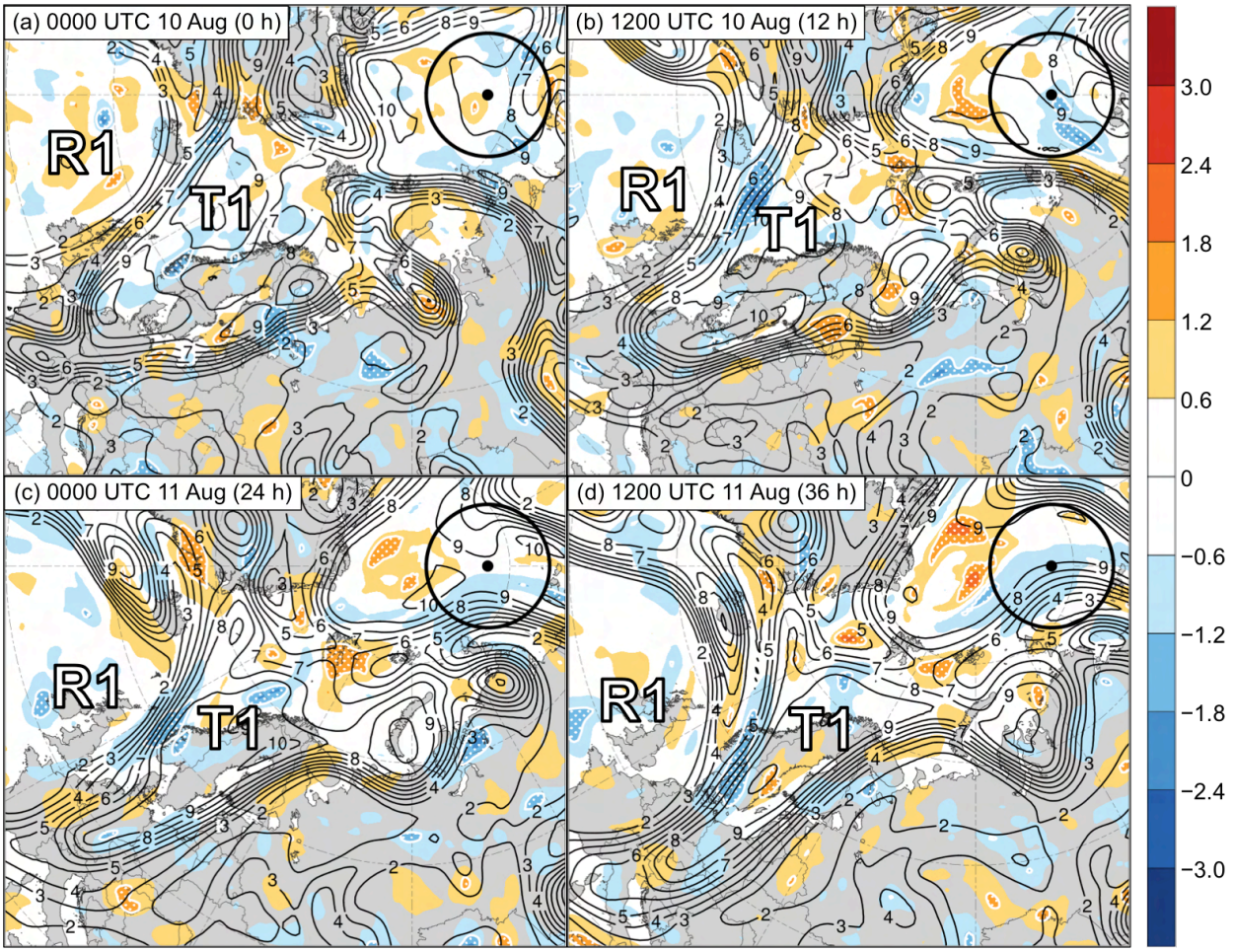

Fig. 4.7. Sensitivity of J_{AC} to 250-hPa PV area averaged within 200 km of each grid point (hPa; shading) and ensemble mean 250-hPa PV area averaged within 200 km of each grid point (PVU; dark gray contours) at (a) 0000 UTC 10 August (0 h), (b) 1200 UTC 10 August (12 h), (c) 0000 UTC 11 August (24 h), and (d) 1200 UTC 11 August (36 h). Regions of white stippling enclosed by white contours indicate where sensitivity is statistically significant at the 95% confidence level. Black dot indicates ERA5 position of AC16 at 0000 UTC 15 August 2016. Black circle indicates region over which J_{AC} is calculated. Labels "R1" and "T1" indicate the positions of these respective features, which are defined in the text. Positive values of sensitivity given by warm colors indicate that increasing 250-hPa PV area averaged within 200 km of each grid point is associated with a decrease in J_{AC} and thus associated with a more accurate prediction of AC16. Negative values of sensitivity given by cool colors indicate that decreasing 250-hPa PV area averaged within 200 km of each grid point is associated with a decrease in J_{AC} and thus associated with a more accurate prediction of AC16.

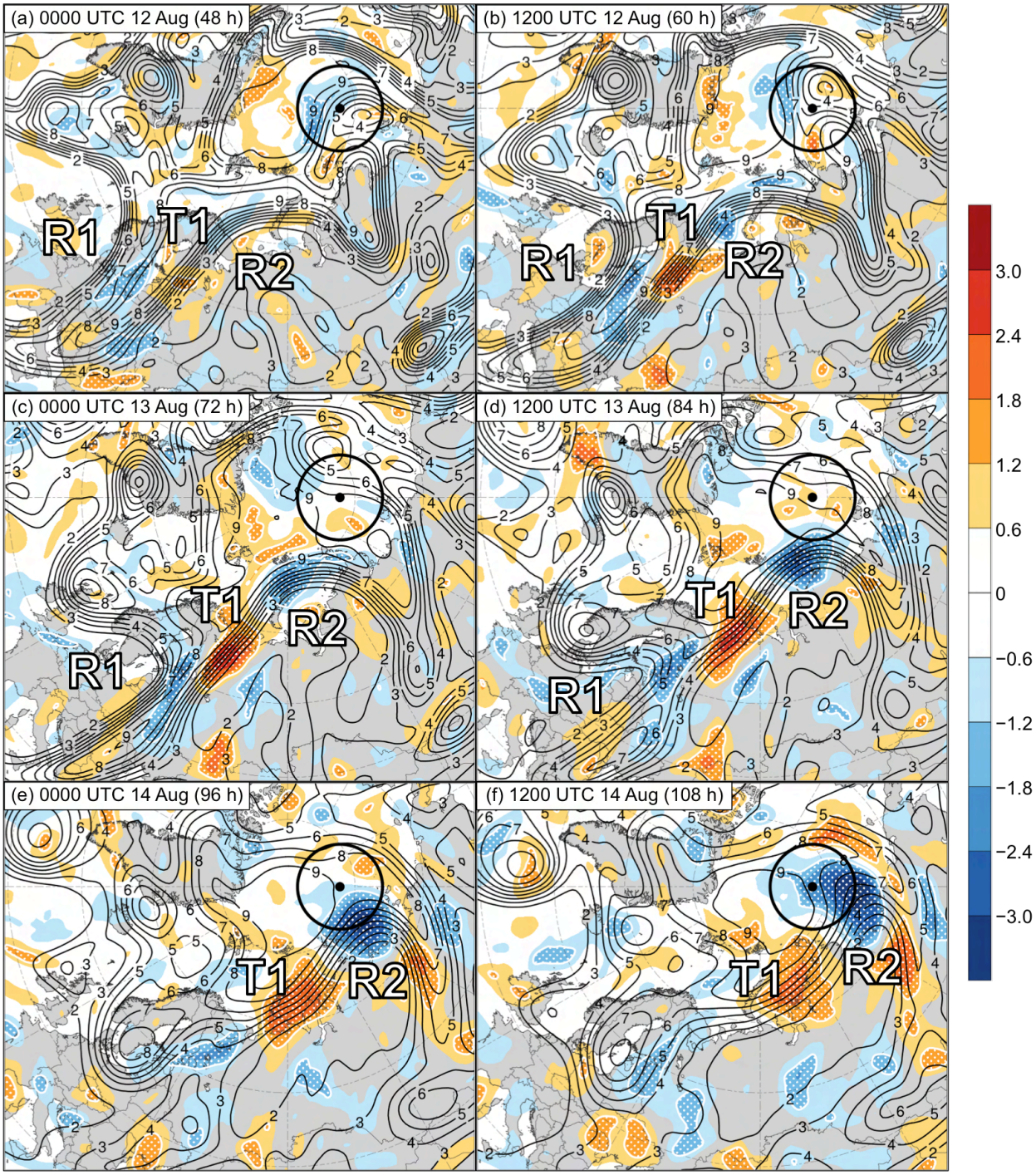

Fig. 4.8. As in Fig. 4.7, but at (a) 0000 UTC 12 August (48 h), (b) 1200 UTC 12 August (60 h), (c) 0000 UTC 13 August (72 h), (d) 1200 UTC 13 August (84 h), (e) 0000 UTC 14 August (96 h), and (f) 1200 UTC 14 August (108 h). Labels “R1”, “R2”, and “T1” indicate the positions of these respective features, which are defined in the text.

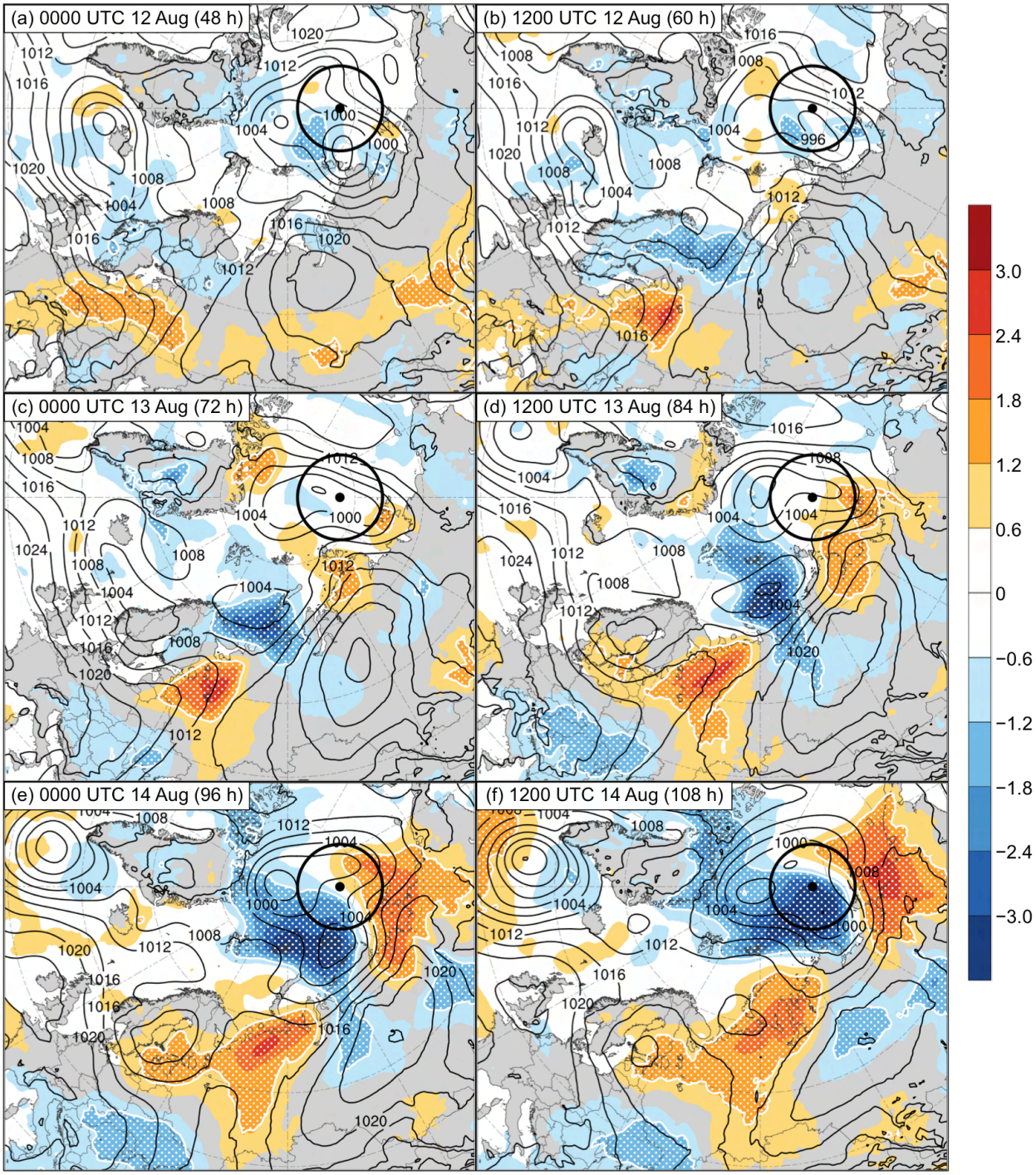

Fig. 4.9. As in Fig. 4.7, but for sensitivity of J_{AC} to SLP (hPa; shading) and ensemble mean SLP (hPa; black contours) at (a) 0000 UTC 12 August (48 h), (b) 1200 UTC 12 August (60 h), (c) 0000 UTC 13 August (72 h), (d) 1200 UTC 13 August (84 h), (e) 0000 UTC 14 August (96 h), and (f) 1200 UTC 14 August (108 h).

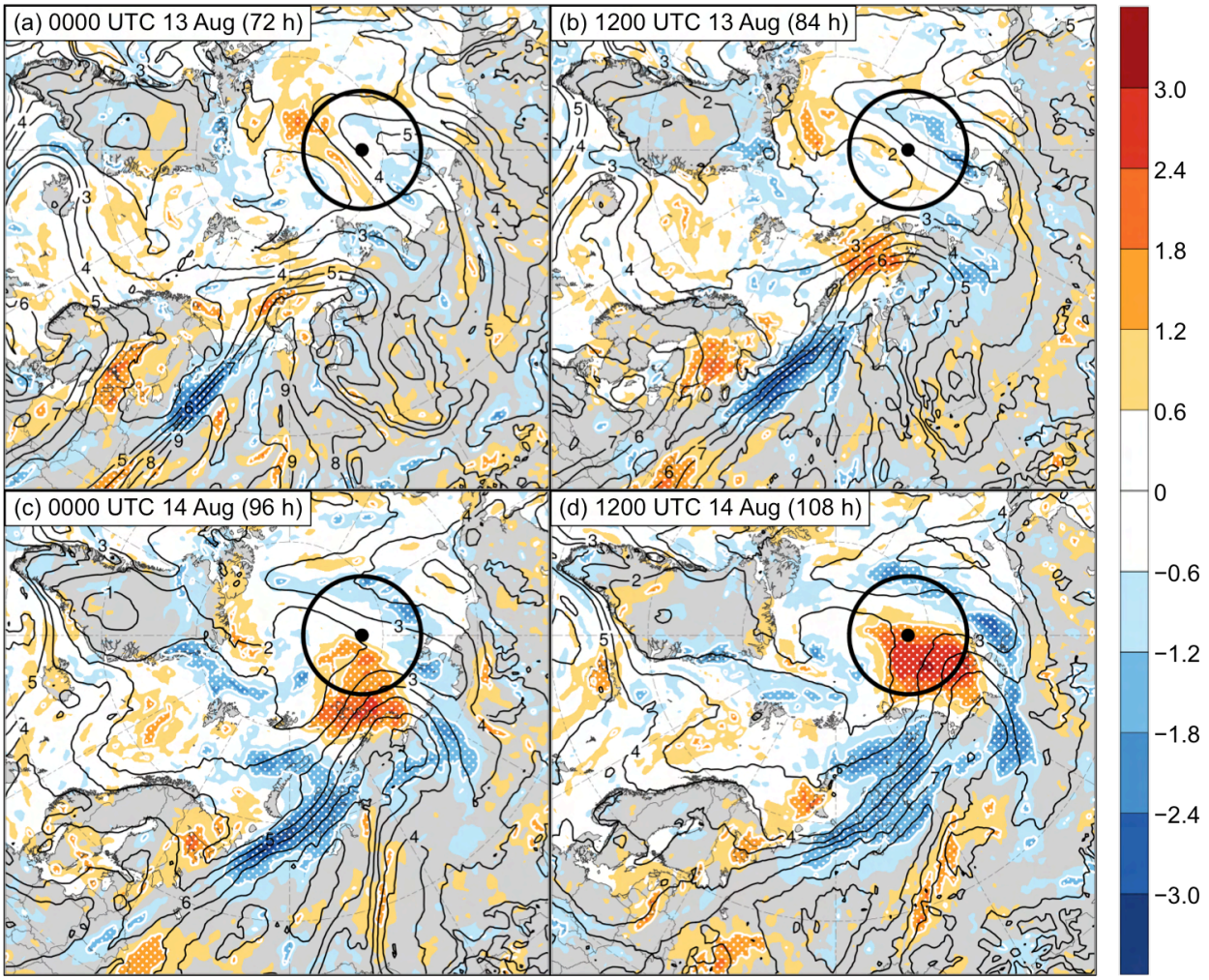

Fig. 4.10. As in Fig. 4.7, but for sensitivity of J_{AC} to 850-hPa specific humidity (hPa; shading) and ensemble mean 850-hPa specific humidity (g kg^{-1}; black contours) at (a) 0000 UTC 13 August (72 h), (b) 1200 UTC 13 August (84 h), (c) 0000 UTC 14 August (96 h), and (d) 1200 UTC 14 August (108 h).

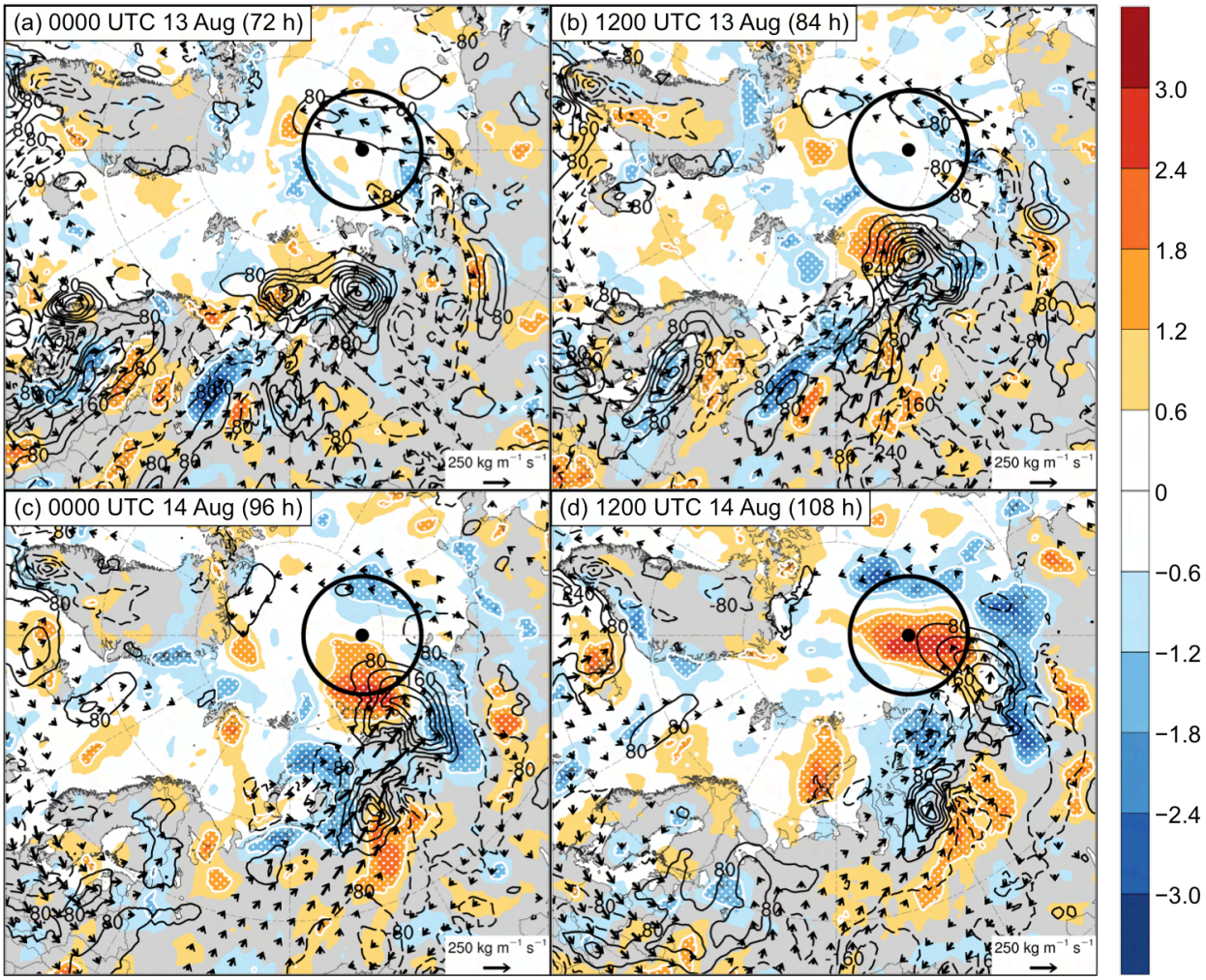

Fig. 4.11. As in Fig. 4.7, but for sensitivity of J_{AC} to 1000–850-hPa IMFC area averaged within 200 km of each grid point (hPa; shading), ensemble mean 1000–850-hPa IMFC area averaged within 200 km of each grid point [every 80 W m^{-2}; black contours (solid for positive values and dashed for negative values)], and ensemble mean 1000–850-hPa IVT (kg m^{-1} s^{-1}; vectors) at (a) 0000 UTC 13 August (72 h), (b) 1200 UTC 13 August (84 h), (c) 0000 UTC 14 August (96 h), and (d) 1200 UTC 14 August (108 h).

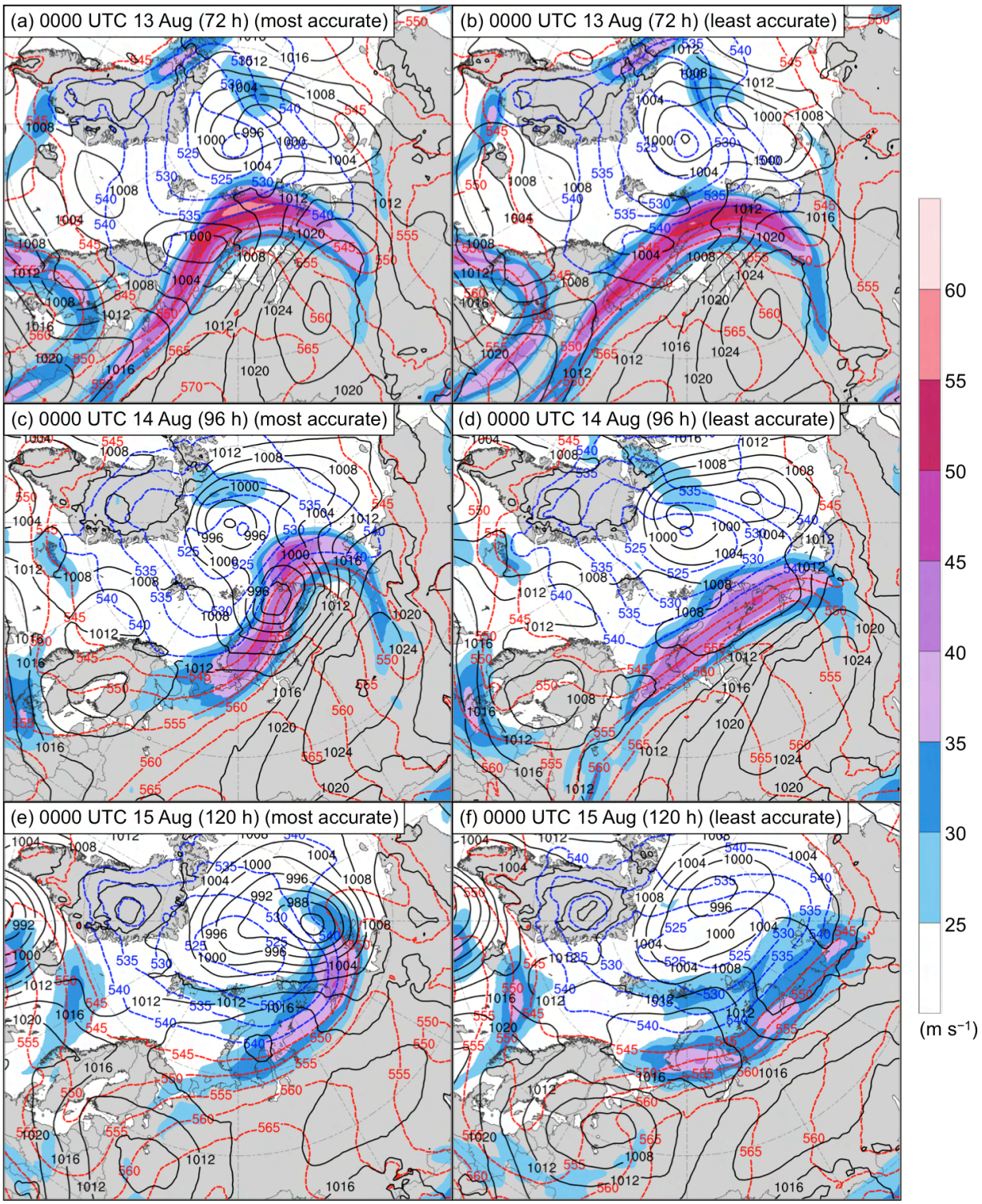

Fig. 4.12. Composites of 300-hPa wind speed (m s^{-1}; shading), 1000–500-hPa thickness (dam; dashed red and blue contours), and SLP (hPa; black contours) at (a),(b) 0000 UTC 13 August (72 h), (c),(d) 0000 UTC 14 August (96 h), and (e),(f) 0000 UTC 15 August (120 h). Composites for most-accurate ensemble forecasts are given in (a),(c),(e) and composites for least-accurate ensemble forecasts are given in (b),(d),(f).

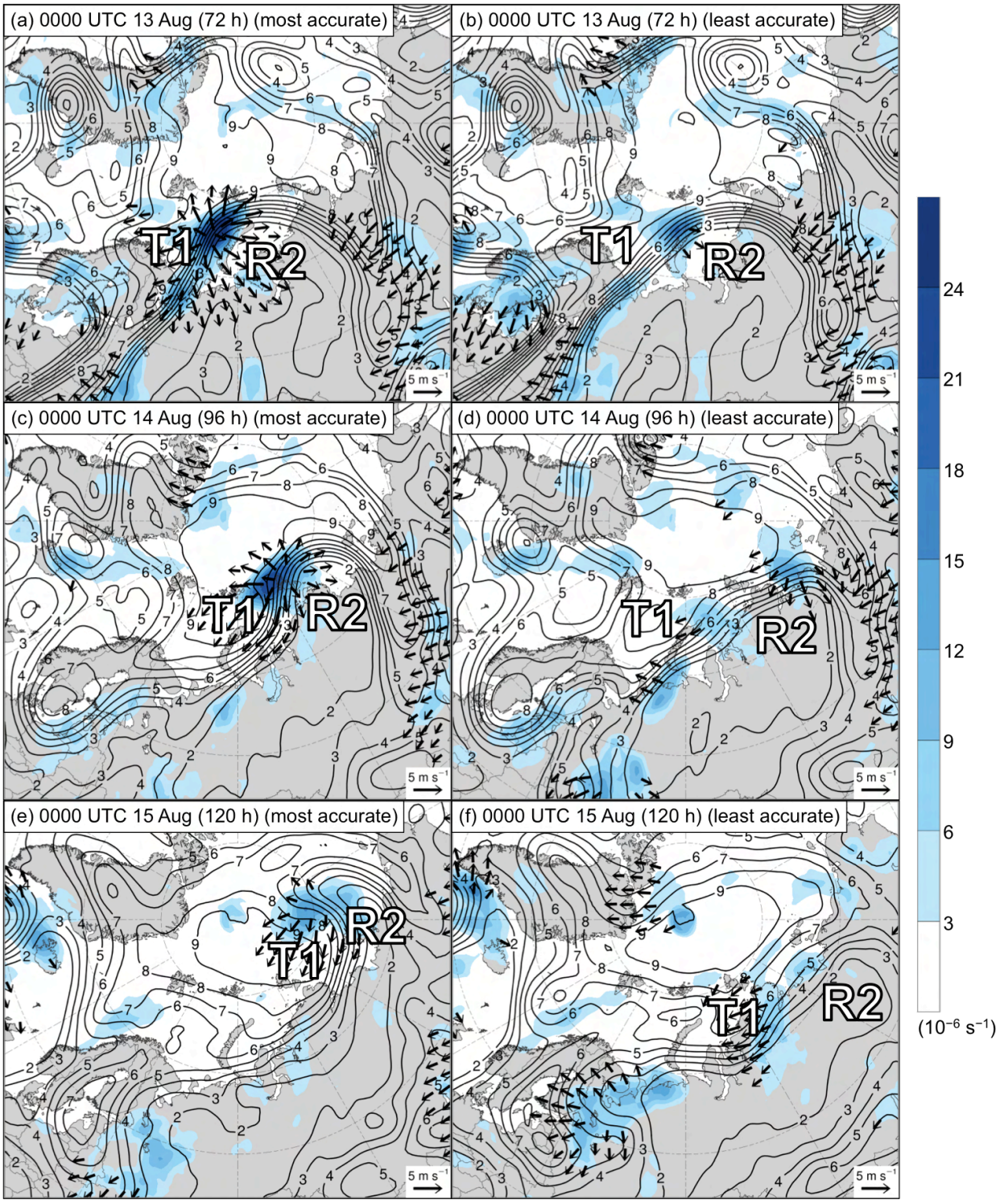

Fig. 4.13. As in Fig. 4.12, but for 300-hPa divergence area averaged within 200 km of each grid point (10^{-6} s^{-1}; shading), 300-hPa irrotational wind area averaged within 200 km of each grid point (m s^{-1}; vectors), and 250-hPa PV area averaged within 200 km of each grid point (PVU; dark gray contours). Labels "R2" and "T1" indicate the positions of these respective features, which are defined in the text.

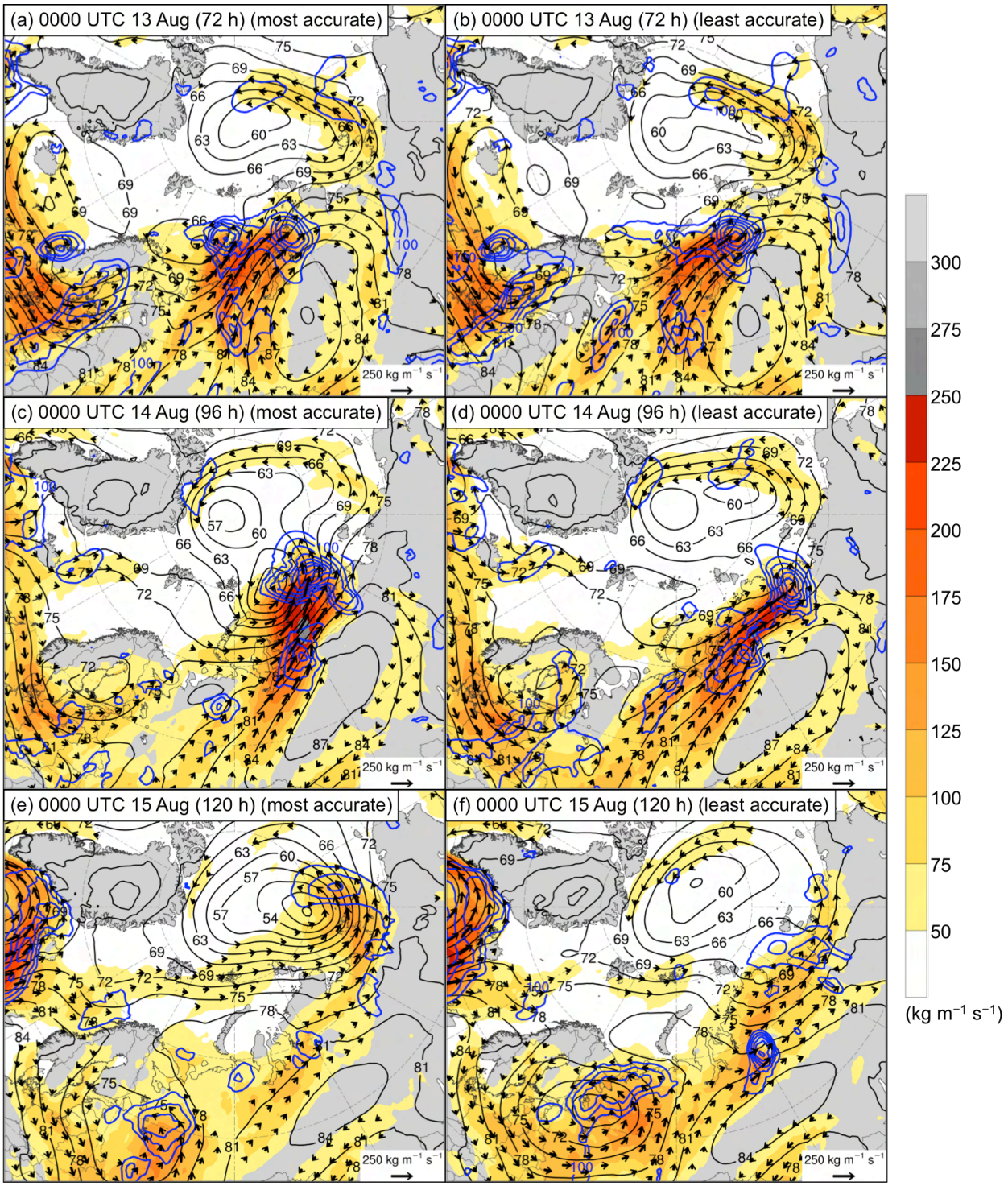

Fig. 4.14. As in Fig. 4.12, but for 1000–850-hPa IVT (kg m^{-1} s^{-1}; shading and vectors), positive values of 1000–850-hPa IMFC area averaged within 200 km of each grid point (every 100 W m^{-2}; blue contours), and 925-hPa geopotential height (dam; black contours).

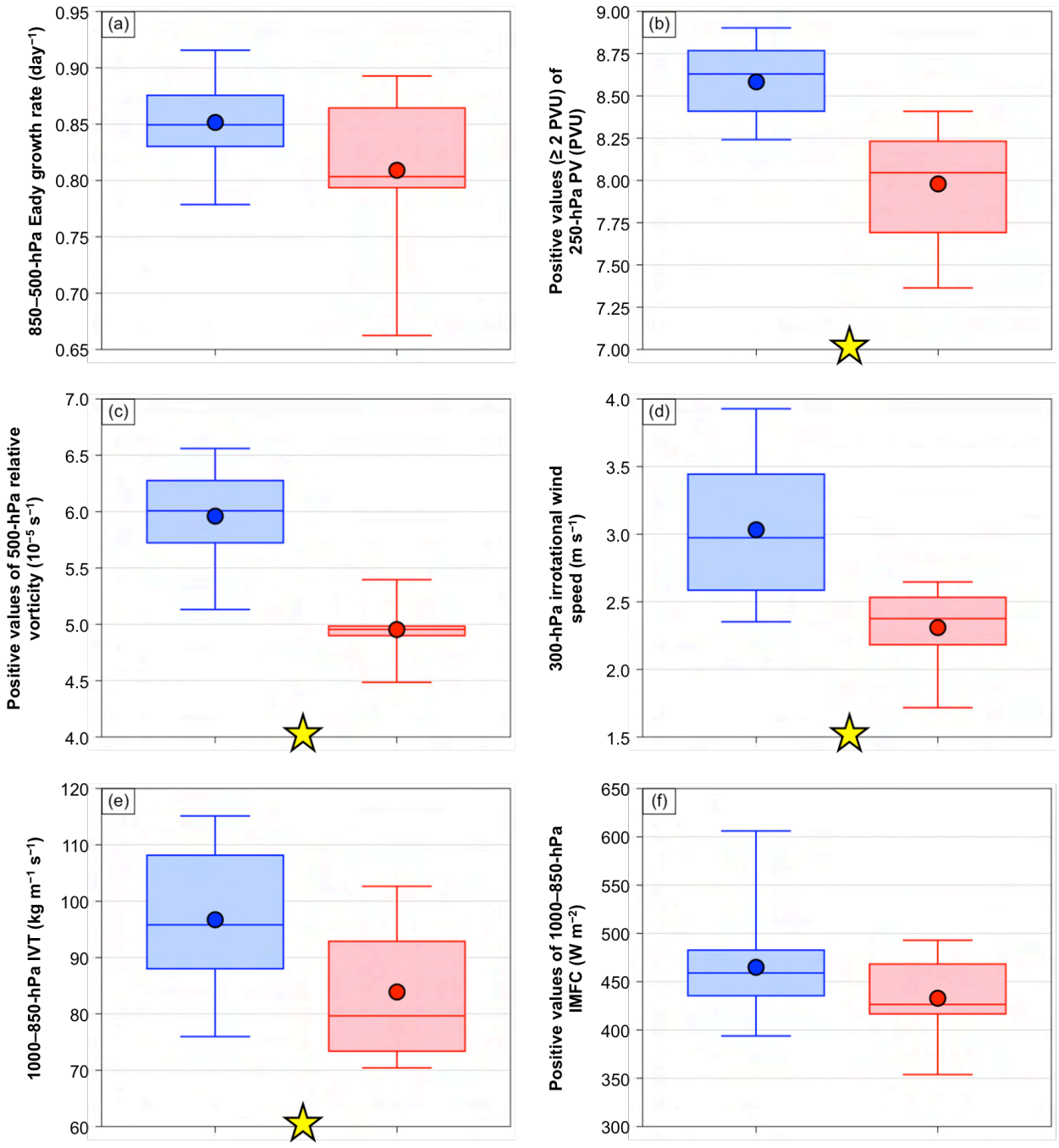

Fig. 4.15. Distributions of (a) area-averaged 850–500-hPa Eady growth rate (day^{-1}), (b) area-averaged positive values (≥ 2 PVU) of 250-hPa PV (PVU), (c) area-averaged positive values of 500-hPa relative vorticity (10^{-5} s^{-1}), (d) area-averaged 300-hPa irrotational wind speed (m s^{-1}), (e) area-averaged 1000–850-hPa IVT (kg m^{-1} s^{-1}), and (f) area-averaged positive values of 1000–850-hPa IMFC (W m^{-2}) for the most-accurate ensemble forecasts (blue) and the least-accurate ensemble forecasts (red) at 0000 UTC 14 August (96 h). The quantities in (a)–(f) are area-averaged within a 1000-km radius from the center of AC16 for each of the aforementioned ensemble forecasts. Dots indicate the mean values, boxes indicate the IQR, and whiskers extend to the minimum and maximum values. Yellow stars indicate statistical significance at the 95%

confidence level between the mean values of the quantities for the most-accurate ensemble members and the mean values of the quantities for the least-accurate ensemble members.

5. Summary and recommendations for future work

a. Summary

The purpose of this dissertation was to improve understanding of Arctic environmental conditions and ACs during periods of low and high forecast skill of the synoptic-scale flow over the Arctic during summer, which were referred to as low-skill periods and high-skill periods, respectively. The first component of this dissertation consisted of a climatological comparison of characteristics of the Arctic environment, and of the frequency, characteristics, and forecast skill of ACs, between low-skill periods and high-skill periods. The second component of this dissertation consisted of an examination of features and processes influencing the evolution of strong low-skill ACs during low-skill periods and strong high-skill ACs during low-skill periods. The third component of this dissertation consisted of a case study examination of features and processes influencing the forecast skill of a selected strong low-skill AC during a low-skill period.

1) Climatological comparison of the Arctic environment and of ACs between low-skill and high-skill periods

Climatologies of low-skill and high-skill periods during the summers of 2007–2017, and climatologies of ACs occurring during these respective periods, were constructed. Climatologies of low-skill and high-skill periods were constructed based on standardized anomalies of area-averaged RMSE of day-5 500-hPa geopotential height forecasts over the Arctic from the 1° GEFS reforecast dataset version 2. Selected dynamic and thermodynamic quantities characterizing the Arctic environment were compared between low-skill and high-skill periods to address the hypothesis that the Arctic environment tends to be characterized by greater synoptic-

scale flow amplitude, greater baroclinic growth rates, and greater latent heating during low-skill periods compared to high-skill periods. The comparison of selected dynamic and thermodynamic quantities supports the aforementioned hypothesis. There tends to be anomalously high-amplitude synoptic-scale flow, anomalously large lower-tropospheric baroclinicity, anomalously large lower-to-midtropospheric Eady growth rates, anomalously large moisture transport, and anomalously large latent heating over the Arctic relative to climatology throughout low-skill periods. There tends to be anomalously low-amplitude synoptic-scale flow, anomalously small lower-tropospheric baroclinicity, anomalously small lower-to-midtropospheric Eady growth rates, anomalously small moisture transport, and anomalously small latent heating over the Arctic relative to climatology throughout high-skill periods.

Forecast errors related to baroclinic processes (e.g., Sanders 1986; Tribbia and Baumhefner 2004; Davies and Didone 2013; Boisseri et al. 2014; Selz and Craig 2015) and latent heating (e.g., Davies and Didone 2013; Rodwell et al. 2013; Madonna et al. 2015; Martínez-Alvarado et al. 2016; Grams et al. 2018) have been shown to contribute to forecast errors in the synoptic-scale flow over the middle latitudes. It is anticipated that given there is greater lower-tropospheric baroclinicity, greater lower-to-midtropospheric Eady growth rates, greater moisture transport, and greater latent heating over the Arctic during low-skill periods, there may be greater forecast errors related to baroclinic processes and greater forecast errors related to latent heating during low-skill periods. These greater forecast errors may help explain the lower forecast skill of the synoptic-scale flow over the Arctic during low-skill periods.

The greater synoptic-scale flow amplitude, greater lower-tropospheric baroclinicity, greater lower-to-midtropospheric Eady growth rates, greater moisture transport, and greater latent heating over the Arctic during low-skill periods compared to high-skill periods suggest

that the Arctic environment may be more conducive for AC development and intensification during low-skill periods compared to high-skill periods. It was hypothesized that ACs occur more frequently across the Arctic, tend to be stronger, and tend to be embedded in more favorable dynamic and thermodynamic environments for development and intensification during low-skill periods compared to high-skill periods. A comparison between ACs during low-skill periods and ACs during high-skill periods supports the aforementioned hypothesis. AC track frequencies are higher across much of the Arctic during low-skill periods compared to high-skill periods. ACs during low-skill periods tend to be statistically significantly stronger, and tend to be embedded in regions characterized by statistically significantly larger lower-tropospheric baroclinicity, statistically significantly larger lower-to-midtropospheric Eady growth rates, statistically significantly larger moisture transport, and statistically significantly larger latent heating, compared to ACs during high-skill periods.

It was hypothesized that ACs are characterized by lower forecast skill during low-skill periods compared to high-skill periods. Forecast errors related to baroclinic processes (e.g., Sanders 1986; Zhu and Thorpe 2006; Zhang et al. 2007; Zheng et al. 2013) and latent heating (e.g., Zhang et al. 2003, 2007; Doyle et al. 2014) have been shown to contribute to forecast errors in midlatitude cyclones. It was anticipated that given the tendency for greater lower-tropospheric baroclinicity, greater lower-to-midtropospheric Eady growth rates, greater moisture transport, and greater latent heating in the vicinity of ACs during low-skill periods, there may be greater forecast errors related to baroclinic processes and greater forecast errors related to latent heating in the vicinity of ACs during low-skill periods. These greater forecast errors may contribute to lower forecast skill of ACs during low-skill periods. The mean intensity RMSE of ACs during low-skill periods tends to be slightly higher than the mean intensity RMSE of ACs

during high-skill periods for forecast lead times of 2–5 days and 7 days, and statistically significantly higher than the mean intensity RMSE of ACs during high-skill periods for forecast lead times of 1 and 6 days. There are no statistically significant differences in the mean values of position RMSE between ACs during low-skill periods and ACs during high-skill periods for all forecast lead times examined. Therefore, the hypothesis that ACs are characterized by lower forecast skill during low-skill periods compared to high-skill periods is marginally supported in terms of forecast skill of intensity of ACs and is not supported in terms of forecast skill of position of ACs.

ACs during low-skill periods and ACs during high-skill periods were separated into the following four skill categories based on the forecast skill of intensity for the 5-day forecast lead time: low-skill ACs during low-skill periods, high-skill ACs during low-skill periods, low-skill ACs during high-skill periods, and high-skill ACs during high-skill periods. It was hypothesized that low-skill ACs during low-skill periods tend to be stronger and tend to be embedded in more favorable dynamic and thermodynamic environments for development and intensification compared to high-skill ACs during low-skill periods. Similarly, it was hypothesized that low-skill ACs during high-skill periods tend to be stronger and tend to be embedded in more favorable dynamic and thermodynamic environments for development and intensification compared to high-skill ACs during high-skill periods. Low-skill ACs during low-skill periods tend to be statistically significantly stronger, and tend to be embedded in regions characterized by larger lower-tropospheric baroclinicity, larger lower-to-midtropospheric Eady growth rates, statistically significantly larger moisture transport, and statistically significantly larger latent heating compared to high-skill ACs during low-skill periods. Low-skill ACs during high-skill periods tend to be stronger, and tend to be embedded in regions characterized by larger lower-

tropospheric baroclinicity, statistically significantly larger lower-to-midtropospheric Eady growth rates, larger moisture transport, and comparable latent heating compared to high-skill ACs during high-skill periods. Therefore, the aforementioned hypotheses are supported, except when comparing latent heating between low-skill ACs during high-skill periods and high-skill ACs during high-skill periods.

The tendency for low-skill ACs during low-skill periods to be statistically significantly stronger than high-skill ACs during low-skill periods and the tendency for low-skill ACs during high-skill periods to be stronger than high-skill ACs during high-skill periods are consistent with the findings of Yamagami et al. (2019) and Capute and Torn (2021). Yamagami et al. (2019) and Capute and Torn (2021) show that ACs with lower forecast skill of intensity tend to be stronger. The tendency for low-skill ACs during low-skill periods to be embedded in regions characterized by larger lower-to-midtropospheric Eady growth rates compared to high-skill ACs during low-skill periods and the tendency for low-skill ACs during high-skill periods to be embedded in regions characterized by statistically significantly larger lower-to-midtropospheric Eady growth rates compared to high-skill ACs during high-skill periods are consistent with the findings of Capute and Torn (2021). Capute and Torn (2021) find that low-skill ACs are typically embedded in regions of larger lower-to-midtropospheric Eady growth rates compared to high-skill ACs.

Of all four skill categories of ACs, low-skill ACs during low-skill periods tend to be the strongest and tend to be embedded in the most favorable dynamic and thermodynamic environments for development and intensification. It is hypothesized that relatively large forecast errors that may be associated with relatively large lower-tropospheric baroclinicity, relatively large lower-to-midtropospheric Eady growth rates, relatively large moisture transport, and relatively large latent heating found in the vicinity of low-skill ACs during low-skill periods may

help explain the low forecast skill of intensity of this category of ACs. Given the distinction between low-skill ACs during low-skill periods and the other skill categories of ACs, and given the challenges low-skill ACs during low-skill periods may pose to human activities in the Arctic, it was of interest to examine features and processes influencing the evolution and forecast skill of low-skill ACs during low-skill periods.

2) Features and processes influencing the evolution of strong low-skill ACs and strong high-skill ACs

Features and processes influencing the evolution of strong low-skill ACs during low-skill periods and strong high-skill ACs during low-skill periods were examined by constructing AC-centered composites for these respective categories of ACs. It was hypothesized that TPVs, baroclinic zones, and WCBs, and TPV–AC interactions, baroclinic processes, and latent heating, influence the evolution of strong low-skill ACs during low-skill periods and strong high-skill ACs during low-skill periods. It was further hypothesized that the aforementioned features and processes tend to be more robust for strong low-skill ACs during low-skill periods. Throughout the rest of this section, strong low-skill ACs during low-skill periods and strong high-skill ACs during low-skill periods are referred to as strong low-skill ACs and strong high-skill ACs, respectively.

The strong low-skill ACs attain a lowest SLP in the range of 962–979 hPa when located in the Arctic. The strong low-skill ACs develop and intensify in regions characterized by strong lower-to-midtropospheric baroclinicity and relatively large lower-to-midtropospheric Eady growth rates, suggesting that baroclinic processes likely play an important role in the development and intensification of strong low-skill ACs. Previous studies of ACs also show the

importance of baroclinic processes to the development and intensification of ACs (e.g., Simmonds and Rudeva 2012; Aizawa et al. 2014; Yamazaki et al. 2015; Tao et al. 2017a,b; Yamagami et al. 2017). The composite analysis suggests that strong low-skill ACs develop and intensify in a region of lateral upper-tropospheric jet coupling associated with dual upper-tropospheric jet streaks, which is a favorable region for cyclone development (e.g., Uccellini and Kocin 1987). The composite analysis suggests that the dual upper-tropospheric jet streaks evolve into a cyclonically curved upper-tropospheric jet streak as the strong low-skill ACs intensify, with the strong low-skill ACs becoming positioned in the favorable poleward exit region of the cyclonically curved upper-tropospheric jet streak. It is hypothesized that the evolution of the dual upper-tropospheric jet streaks into a cyclonically curved upper-tropospheric jet streak is related to the reconfiguration of the regions of strong lower-to-midtropospheric baroclinicity in the vicinity of the strong low-skill ACs, which likely occurs partly in response to lower-to-midtropospheric thermal advection in the vicinity of the strong low-skill ACs. Tao et al. (2017b) similarly show that two upper-tropospheric jet streaks influencing the development and intensification of AC12 evolve into a cyclonically curved upper-tropospheric jet streak as AC12 intensifies.

TPVs and TPV–AC interactions likely play an important role in the development and intensification of the strong low-skill ACs. The composite analysis suggests that the strong low-skill ACs develop and intensify downstream of a 500-hPa relative vorticity maximum and an associated upper-tropospheric PV maximum, which likely are signatures of a TPV. The composite analysis suggests that TPVs gradually approach the strong low-skill ACs as the strong low-skill ACs intensify, such that the vertical tilt between TPVs and the strong low-skill ACs gradually decreases. The decrease in vertical tilt is consistent with QG theory for the

development of midlatitude cyclones (e.g., Martin 2006, section 8.8). The decrease in vertical tilt is also suggestive of interaction between TPVs and the strong low-skill ACs. The composite analysis suggests that TPVs become vertically superposed with the strong low-skill ACs as the strong low-skill ACs reach peak intensity and gradually weaken. The vertical superposition of TPVs with the strong low-skill ACs is associated with the formation of a tropospheric-deep cyclone exhibiting an equivalent barotropic structure. Previous studies, including Aizawa et al. (2014), Aizawa and Tanaka (2016), Tao et al. (2017a,b), and Yamagami et al. (2017), similarly show that TPVs become vertically superposed with ACs and exhibit an equivalent barotropic structure, at or around the time the ACs reach peak intensity.

As discussed in section 1b(2)ii, latent heating has been shown to play an important role in the development and intensification of midlatitude cyclones in numerous studies (e.g., Tracton 1973; Kuo and Reed 1988; Reed et al. 1988, 1992; Kuo et al. 1991; Davis et al. 1993; Stoelinga 1996; Wernli et al. 2002), but there has been a dearth of research on the role of latent heating in the development and intensification of ACs. IVT and IMFC were examined to determine the possible role of latent heating in the development and intensification of the strong low-skill ACs. The composite analysis suggests that the strong low-skill ACs are associated with a relatively strong corridor of IVT, which may be a manifestation of WCBs and/or ARs associated with the strong low-skill ACs. Accompanying the IVT corridor is a well-defined region of IMFC in the vicinity of the strong low-skill ACs. The region of IMFC implies that latent heating occurs in the vicinity of the strong low-skill ACs and likely contributes to the development and intensification of the strong low-skill ACs. Collocated with the well-defined region of IMFC are regions of lower-to-midtropospheric ascent, upper-tropospheric divergence, and upper-tropospheric irrotational outflow, which likely are signatures of the latent heating.

The composite analysis for the strong low-skill ACs suggests that a combination of TPV–AC interactions, baroclinic processes, and latent heating likely contribute to the development and intensification of this category of ACs. A composite analysis for the strong high-skill ACs was also conducted to determine how features and processes influencing the evolution of strong high-skill ACs compare to features and processes influencing the evolution of strong low-skill ACs. The strong high-skill ACs attain a lowest SLP in the range of 967–991 hPa when located in the Arctic, and almost all of the strong high-skill ACs are weaker than the strong low-skill ACs. The composite analysis for the strong high-skill ACs suggests that these ACs interact with TPVs in a region of moderate lower-to-midtropospheric baroclinicity and moderate lower-to-midtropospheric Eady growth rates, and that these ACs are associated with an IVT corridor and regions of moderate latent heating.

To compare features and processes influencing the evolution of the strong low-skill ACs and strong high-skill ACs, selected dynamic and thermodynamic quantities were area-averaged within a 1000-km radius from the centers of the individual ACs at various times throughout the evolution of the individual ACs. Baroclinic processes were shown to likely support the development and intensification of the strong high-skill ACs, but to a lesser extent compared to the strong low-skill ACs. The mean values of area-averaged lower-to-midtropospheric Eady growth rate are smaller (by 0.09–0.14 day^{-1}) for the strong high-skill ACs compared to the strong low-skill ACs. The mean values of area-averaged upper-tropospheric wind speed are lower (by 5.0–5.9 m s^{-1}) for the strong high-skill ACs compared to the strong low-skill ACs. TPVs and TPV–AC interactions were shown to likely support the development and intensification of the strong high-skill ACs, but to a lesser extent compared to the strong low-skill ACs. The mean values of area-averaged upper-tropospheric PV are smaller (by 0.8–1.1

PVU) for the strong high-skill ACs compared to the strong low-skill ACs. The mean values of area-averaged 500-hPa relative vorticity are smaller (by 0.9–1.9 × 10^{-5} s^{-1}) for the strong high-skill ACs compared to the strong low-skill ACs.

Latent heating was shown to possibly support the development and intensification of the strong high-skill ACs, but to a lesser extent compared to the strong low-skill ACs. The mean values of area-averaged IVT are smaller (by 36–81 kg m^{-1} s^{-1}) for the strong high-skill ACs compared to the strong low-skill ACs. The mean values of area-averaged IMFC are smaller (by 48–183 W m^{-2}) for the strong high-skill ACs compared to the strong low-skill ACs. It is hypothesized that the more robust features and processes influencing the strong low-skill ACs compared to the strong high-skill ACs may be associated with larger forecast errors that may help explain the lower forecast skill of intensity of the strong low-skill ACs compared to the strong high-skill ACs.

3) Features and processes influencing the forecast skill of a selected strong low-skill AC

A representative strong low-skill AC during a low-skill period was examined to understand what features and processes may influence the forecast skill of strong low-skill ACs during low-skill periods. The representative strong low-skill AC during a low-skill period is AC16, which occurred during 13–19 August 2016. Features and processes influencing the forecast skill of AC16 were determined by conducting an ensemble-based sensitivity analysis (ESA) of AC16 and by comparing the most-accurate and least-accurate ensemble forecasts of AC16. The ESA and the comparison of forecasts were utilized to address the hypothesis that forecast errors in TPVs, baroclinic zones, and WCBs, and forecast errors in TPV–AC interactions, baroclinic processes, and latent heating, contribute to forecast errors in strong low-

skill ACs during low-skill periods. Based on the ESA and the comparison of forecasts, the extent to which the aforementioned hypothesis may be supported is unknown, such that future work is required to address the aforementioned hypothesis. Recommendations for future work are provided in the next section. Results from the ESA and the comparison of forecasts are now summarized.

The ESA suggests that the predictability of AC16 is sensitive to the amplitude and strength of an upper-tropospheric trough (T1), and to the strength of an embedded TPV, upstream of AC16. It is speculated from the ESA that an eastward shift in an upper-tropospheric ridge over the North Atlantic and western Eurasia early in the forecasts may be associated with a more amplified and stronger T1, and a stronger embedded TPV, later in the forecasts. It is further speculated that a more amplified and stronger T1, and a stronger embedded TPV, may be associated with greater amplification of the downstream upper-tropospheric flow, and concomitantly greater development and intensification of AC16.

The comparison of forecasts indicates that a more amplified upper-tropospheric flow in the vicinity of AC16 in the most-accurate ensemble forecasts compared to the least-accurate ensemble forecasts is associated with stronger upper-tropospheric divergence and irrotational outflow. The stronger upper-tropospheric divergence and irrotational outflow likely contribute to the greater development and intensification of AC16 in the most-accurate ensemble forecasts compared to the least-accurate ensemble forecasts.

It is hypothesized from the ESA and the comparison of forecasts that forecast errors in T1 and the embedded TPV, and forecast errors in other upper-tropospheric features, may contribute to forecast errors in AC16. Previous studies, including Yamagami et al. (2018a) and Johnson and Wang (2021), suggest that forecast errors in TPVs and other upper-tropospheric features can

contribute to forecast errors in ACs. Previous studies (e.g., Sanders 1986, 1992; Kuo and Reed 1988; Sanders et al. 2000; Langland et al. 2002; Chang et al. 2013; Zheng et al. 2013; Lamberson et al. 2016) have demonstrated that forecast errors in midlatitude cyclones can be linked to forecast errors in upper-tropospheric features, such as upper-tropospheric troughs and ridges. Langland et al. (2002), Chang et al. (2013), and Lamberson et al. (2016) have also demonstrated that upper-tropospheric forecast errors influencing the forecast skill of midlatitude cyclones can propagate downstream as structures resembling wave packets. It is hypothesized from the ESA that upper-tropospheric forecast errors influencing the forecast skill of AC16 may also propagate downstream as structures resembling wave packets.

The comparison of forecasts suggests that AC16 develops in regions of comparable lower-to-midtropospheric baroclinicity and comparable lower-to-midtropospheric Eady growth rates between the most-accurate and least-accurate ensemble forecasts. However, there is a more amplified thickness trough and ridge in the vicinity of AC16 in the most-accurate ensemble forecasts compared to the least-accurate ensemble forecasts. From Sutcliffe development theory, cyclogenesis is favored between a thickness trough and ridge, in response to the advection of thermal vorticity by the thermal wind (e.g., Carlson 1998, section 8.1). Given the more amplified thickness trough and ridge in the vicinity of AC16 in the most-accurate ensemble forecasts, it is hypothesized that there may be greater advection of thermal vorticity by the thermal wind between the thickness trough and ridge that contributes to the greater intensification of AC16 in the most-accurate ensemble forecasts.

The ESA and the comparison of forecasts suggest that a northwestward shift in a moisture corridor and in a region of latent heating in the vicinity of AC16 is associated with a more accurate prediction of AC16. There are mixed signals whether greater latent heating is

associated with a more accurate prediction of AC16. It is speculated that greater upper-tropospheric dynamical forcing that may be associated with the suggested stronger TPV embedded in T1 upstream of AC16 in the most-accurate ensemble forecasts compared to the least-accurate ensemble forecasts may support greater latent heating in the vicinity of AC16 in the most-accurate ensemble forecasts. However, area-averaged lower-tropospheric IMFC in the vicinity of AC16 is comparable between the most-accurate and least-accurate ensemble forecasts. Although area-averaged lower-tropospheric IVT in the vicinity of AC16 is statistically significantly larger for the most-accurate ensemble forecasts compared to the least-accurate ensemble forecasts, the maximum magnitude of lower-tropospheric IVT in the vicinity of AC16 is comparable between the most-accurate and least-accurate ensemble forecasts.

b. Recommendations for future work

The results presented in this dissertation motivate a variety of future research opportunities. The low-skill and high-skill periods identified in this dissertation could be stratified by synoptic weather pattern, as done by Yamagami and Matsueda (2021), in order to determine what synoptic weather patterns are less or more predictable. Self-organizing maps (e.g., Kohonen 1995) could be utilized to identify common synoptic weather patterns during low-skill and high-skill periods. Composite analyses of common synoptic weather patterns during low-skill and high-skill periods could be constructed to examine the evolution of features and processes associated with the common synoptic weather patterns.

Predictability studies of additional strong low-skill ACs could be carried out to determine how the features and processes hypothesized to influence the prediction of AC16 compare to features and processes that may influence the prediction of other strong low-skill ACs. The ESA

for AC16 suggests that the prediction of AC16 exhibits sensitivity to the strength of a TPV. It would be of interest to determine the extent to which the prediction of other strong low-skill ACs exhibit sensitivity to the strength of TPVs.

A number of features and processes were suggested to contribute to the development and intensification of strong low-skill ACs. However, the extent to which the various features and processes contribute to the development and intensification of the strong low-skill ACs has not been established in this dissertation. The extent to which forecast errors related to features and processes influencing AC16 contribute to forecast errors in AC16 also remains an open question. Numerical modeling studies of selected strong low-skill ACs, such as AC16, could be carried out to determine the sensitivity of the development and intensification of the selected strong low-skill ACs to various features and processes. As an example of a numerical modeling study, the sensitivity of the development and intensification of a selected strong low-skill AC to latent heating could be determined by comparing a numerical simulation of the AC with no moist processes included to a simulation of the AC with moist processes included, as done by Kuo and Reed (1988) for a midlatitude cyclone. As another example of a numerical modeling study, the sensitivity of the development and intensification of a selected strong low-skill AC to the strength of TPVs could be determined via numerical simulations in which the strength of TPVs is changed, as done by Tao et al. (2017b) for AC12. The strength of a TPV could be changed, for example, by varying the dynamic tropopause potential temperature pattern associated with the TPV. The impact of the changes in the strength of the TPV on diagnostic quantities related to AC development, such as cyclonic vorticity advection by the horizontal wind, could then be examined.

The sources of moisture for the IVT corridors associated with the strong low-skill ACs in section 3c(1) were not examined. Fearon et al. (2021) show that sources of moisture for moist intrusions associated with ACs during summer include surface evaporation over the Gulf Stream and surface evaporation over high-latitude continental landmasses. A trajectory analysis could be conducted following the approach employed by Fearon et al. (2021) to determine how the sources of moisture for the IVT corridors influencing the strong low-skill ACs compare to the sources of moisture for the moist intrusions examined by Fearon et al. (2021).

REFERENCES

Aizawa, T., and H. L. Tanaka, 2016: Axisymmetric structure of the long lasting summer Arctic cyclones. *Polar Sci.*, **10**, 192–198. https://doi.org/10.1016/j.polar.2016.02.002.

Aizawa, T., H. L. Tanaka, and M. Satoh, 2014: Rapid development of arctic cyclone in June 2008 simulated by the cloud resolving global model NICAM. *Meteorol. Atmos. Phys.*, **126**, 105–117, https://doi.org/10.1007/s00703-013-0272-6.

Asplin, M. G., R. Galley, D. G. Barber, and S. Prinsenberg, 2012: Fracture of summer perennial sea ice by ocean swell as a result of Arctic storms. *J. Geophys. Res.*, **117**, C06025, https://doi.org/10.1029/2011JC007221.

Bauer, P., L. Magnusson, J.-N. Thépaut, and T. M. Hamill, 2016: Aspects of ECMWF model performance in polar areas. *Quart. J. Roy. Meteor. Soc.,* **142**, 583–596, https://doi.org/10.1002/qj.2449.

Baumgart, M., M. Riemer, V. Wirth, F. Teubler, and S. T. K. Lang, 2018: Potential vorticity dynamics of forecast errors: A quantitative case study. *Mon. Wea. Rev.*, **146**, 1405–1425, https://doi.org/10.1175/MWR-D-17-0196.1.

Berman, J. D., and R. D. Torn, 2019: The impact of initial condition and warm conveyor belt forecast uncertainty on variability in the downstream waveguide in an ECWMF case study. *Mon. Wea. Rev.*, **147**, 4071–4089, https://doi.org/10.1175/MWR-D-18-0333.1.

Biernat, K. A., L. F. Bosart, and D. Keyser, 2021: A climatological analysis of the linkages between tropopause polar vortices, cold pools, and cold air outbreaks over the central and eastern United States. *Mon. Wea. Rev.*, **149**, 189–206, https://doi.org/10.1175/MWR-D-20-0191.1.

Binder, H., M. Boettcher, C. M. Grams, H. Joos, S. Pfahl, and H. Wernli, 2017: Exceptional air mass transport and dynamical drivers of an extreme wintertime Arctic warm event. *Geophys. Res. Lett.,* **44,** 12028–12036, https://doi.org/10.1002/2017GL075841.

Boisserie, M., P. Arbogast, L. Descamps, O. Pannekoucke, and L. Raynaud, 2014: Estimating and diagnosing model error variances in the Météo-France global NWP model. *Quart. J. Roy. Meteor. Soc.*, **140**, 846–854, https://doi.org/10.1002/qj.2173.

Bosart, L. F., G. J. Hakim, K. R. Tyle, M. A. Bedrick, W. E. Bracken, M. J. Dickinson, and D. M. Schultz, 1996: Large-scale antecedent conditions associated with the 12–14 March 1993 cyclone ("Superstorm '93") over eastern North America. *Mon. Wea. Rev.*, **124**, 1865–1891, https://doi.org/10.1175/1520-0493(1996)124<1865:LSACAW>2.0.CO;2.

Bougeault, P., and Coauthors, 2010: The THORPEX Interactive Grand Global Ensemble. *Bull. Amer. Meteor. Soc.*, **91**, 1059–1072, https://doi.org/10.1175/2010BAMS2853.1.

Bray, M. T., S. M. Cavallo, and H. B. Bluestein, 2021: Examining the relationship between tropopause polar vortices and tornado outbreaks. *Wea. Forecasting*, **36**, 1799–1814, https://doi.org/10.1175/WAF-D-21-0058.1.

Brodzik, M. J., B. Billingsley, T. Haran, B. Raup, and M. H. Savoie, 2012: EASE-Grid 2.0: Incremental but significant improvements for Earth-gridded data sets. *ISPRS Int. J. Geoinf.*, **1**, 32–45, https://doi.org/10.3390/ijgi1010032.

Capute, P. K., and R. D. Torn, 2021: A comparison of Arctic and Atlantic cyclone predictability. *Mon. Wea. Rev.*, **149**, 3837–3849, https://doi.org/10.1175/MWR-D-20-0350.1.

Carlson, T. N., 1998: *Mid-Latitude Weather Systems*. Amer. Meteor. Soc., 507 pp.

Cavallo, S. M., and G. J. Hakim, 2009: Potential vorticity diagnosis of a tropopause polar cyclone. *Mon. Wea. Rev.*, **137**, 1358–1371, https://doi.org/10.1175/2008MWR2670.1.

Cavallo, S. M., and G. J. Hakim, 2010: Composite structure of tropopause polar cyclones. *Mon. Wea. Rev.*, **138**, 3840–3857, https://doi.org/10.1175/2010MWR3371.1.

Cavallo, S. M., and G. J. Hakim, 2012: Radiative impact on tropopause polar vortices over the Arctic. *Mon. Wea. Rev.*, **140**, 1683–1702, https://doi.org/10.1175/MWR-D-11-00182.1.

Chang, E. K. M., M. Zheng, and K. Raeder, 2013: Medium-range ensemble sensitivity analysis of two extreme pacific extratropical cyclones. *Mon. Wea. Rev.*, **141**, 211–231, https://doi.org/10.1175/MWR-D-11-00304.1.

CPC, 2021: Normalized daily AO indices. CPC, accessed 1 October 2021. [Available online at ftp://ftp.cpc.ncep.noaa.gov/cwlinks/norm.daily.ao.index.b500101.current.ascii.]

Crawford, A., and M. Serreze, 2015: A new look at the summer Arctic frontal zone. *J. Climate*, **28**, 737–754, https://doi.org/10.1175/JCLI-D-14-00447.1.

Crawford, A. D., and M. C. Serreze, 2016: Does the summer Arctic frontal zone influence Arctic Ocean cyclone activity? *J. Climate*, **29**, 4977–4993, https://doi.org/10.1175/JCLI-D-15-0755.1.

Crawford, A. D., E. A. P. Schreiber, N. Sommer, M. C. Serreze, J. C. Stroeve, and D. G. Barber, 2021: Sensitivity of Northern Hemisphere cyclone detection and tracking results to fine spatial and temporal resolution using ERA5. *Mon. Wea. Rev.*, **149**, 2581–2598, https://doi.org/10.1175/MWR-D-20-0417.1.

Dai, A., D. Luo, M. Song, and J. Liu, 2019: Arctic amplification is caused by sea-ice loss under increasing CO_2. *Nat. Commun.*, **10**, 121, https://doi.org/10.1038/s41467-018-07954-9.

Davies, H. C., and M. Didone, 2013: Diagnosis and dynamics of forecast error growth. *Mon. Wea. Rev.*, **141**, 2483–2501, https://doi.org/10.1175/MWR-D-12-00242.1.

Davis, C. A., M. T. Stoelinga, and Y.-H. Kuo, 1993: The integrated effect of condensation in numerical simulations of extratropical cyclogenesis. *Mon. Wea. Rev.*, **121**, 2309–2330, https://doi.org/10.1175/1520-0493(1993)121<2309:TIEOCI>2.0.CO;2.

Dee, D. P., and Coauthors, 2011: The ERA-Interim reanalysis: Configuration and performance of the data assimilation system. *Quart. J. Roy. Meteor. Soc.*, **137**, 553–597, https://doi.org/10.1002/qj.828.

Dickinson, M. J., L. F. Bosart, W. E. Bracken, G. J. Hakim, D. M. Schultz, M. A. Bedrick, and K. R. Tyle, 1997: The March 1993 Superstorm cyclogenesis: Incipient phase synoptic- and convective-scale flow interaction and model performance. *Mon. Wea. Rev.*, **125**, 3041–3072, https://doi.org/10.1175/1520-0493(1997)125<3041:TMSCIP>2.0.CO;2.

Doyle, J. D., C. Amerault, C. A. Reynolds, and P. A. Reinecke, 2014: Initial condition sensitivity and predictability of a severe extratropical cyclone using a moist adjoint. *Mon. Wea. Rev.*, **142**, 320–342, https://doi.org/10.1175/MWR-D-13-00201.1.

Doyle, J. D., C. A. Reynolds, and C. Amerault, 2019: Adjoint sensitivity analysis of high-impact extratropical cyclones. *Mon. Wea. Rev.*, **147**, 4511–4532, https://doi.org/10.1175/MWR-D-19-0055.1.

Eguíluz, V. M., J. Fernández-Gracia, X. Irigoien, and C. M. Duarte, 2016: A quantitative assessment of Arctic shipping in 2010–2014. *Sci. Rep.*, **6**, 30682, https://doi.org/10.1038/srep30682.

Fearon, M. G., J. D. Doyle, D. R. Ryglicki, P. M. Finocchio, and M. Sprenger, 2021: The role of cyclones in moisture transport into the Arctic. *Geophys. Res. Lett.*, **48**, e2020GL090353, https://doi.org/10.1029/2020GL090353.

Froude, L. S. R., 2010: TIGGE: Comparison of the prediction of Northern Hemisphere extratropical cyclones by different ensemble prediction systems. *Wea. Forecasting*, **25**, 819–836, https://doi.org/10.1175/2010WAF2222326.1.

Grams, C. M., L. Magnusson, and E. Madonna, 2018: An atmospheric dynamics perspective on the amplification and propagation of forecast error in numerical weather prediction models: A case study. *Quart. J. Roy. Meteor. Soc.,* **144**, 2577–2591, https://doi.org/10.1002/qj.3353.

Hakim, G. J., 2000: Climatology of coherent structures on the extratropical tropopause. *Mon. Wea. Rev.*, **128**, 385–406, https://doi.org/10.1175/1520-0493(2000)128<0385:COCSOT>2.0.CO;2.

Hakim, G. J., 2005: Vertical structure of midlatitude analysis and forecast errors. *Mon. Wea. Rev.*, **133**, 567–578, https://doi.org/10.1175/MWR-2882.1.

Hakim, G. J., L. F. Bosart, and D. Keyser, 1995: The Ohio Valley wave-merger cyclogenesis event of 25–26 January 1978. Part I: Multiscale case study. *Mon. Wea. Rev.*, **123**, 2663–2692, https://doi.org/10.1175/1520-0493(1995)123<2663:TOVWMC>2.0.CO;2.

Hall, C. M., and J. Saarinen, 2010: Polar tourism: Definitions and dimensions. *Scand. J. Hospitality Tourism,* **10**, 448–467, https://doi.org/10.1080/15022250.2010.521686.

Hamill, T. M., and Kiladis, G. N, 2014: Skill of the MJO and Northern Hemisphere blocking in GEFS medium-range reforecasts. *Mon. Wea. Rev.*, **142**, 868–885, https://doi.org/10.1175/MWR-D-13-00199.1.

Hamill, T. M., G. T. Bates, J. S. Whitaker, D. R. Murray, M. Fiorino, T. J. Galarneau Jr., Y. Zhu, and W. Lapenta, 2013: NOAA's second-generation global medium-range ensemble reforecast dataset. *Bull. Amer. Meteor. Soc.*, **94**, 1553–1565, https://doi.org/10.1175/BAMS-D-12-00014.1.

Hersbach, H., and Coauthors, 2020: The ERA5 global reanalysis. *Quart. J. Roy. Meteor. Soc.*, **146**, 1999–2049, https://doi.org/10.1002/qj.3803.

Holt, B., and S. Martin, 2001: The effect of a storm on the 1992 summer sea ice cover of the Beaufort, Chukchi, and East Siberian Seas. *J. Geophys. Res.*, **106(C1)**, 1017–1032, https://doi.org/10.1029/1999JC000110.

Hoskins, B. J., and P. J. Valdes, 1990: On the existence of storm-tracks. *J. Atmos. Sci*, **47**, 1854–1864, https://doi.org/10.1175/1520-0469(1990)047<1854:OTEOST>2.0.CO;2.

Hoskins, B. J., M. E. McIntyre, and A. W. Robertson, 1985: On the use and significance of isentropic potential vorticity maps. *Quart. J. Roy. Meteor. Soc.*, **111**, 877–946, https://doi.org/10.1002/qj.49711147002.

Inoue, J., 2020: Review of forecast skills for weather and sea ice in supporting Arctic navigation. *Polar Sci.*, **27**, 100523. https://doi.org/10.1016/j.polar.2020.100523.

Johnson, A., and X. Wang, 2021: Observation impact study of an Arctic cyclone associated with a tropopause polar vortex (TPV)-induced Rossby wave initiation event. *Mon. Wea. Rev.*, **149**, 1577–1591, https://doi.org/10.1175/MWR-D-20-0285.1.

Jung, T., and M. Leutbecher, 2007: Performance of the ECMWF forecasting system in the Arctic during winter. *Quart. J. Roy. Meteor. Soc.*, **133**, 1327–1340, https://doi.org/10.1002/qj.99.

Jung, T., and M. Matsueda, 2016: Verification of global numerical weather forecasting systems in polar regions using TIGGE data. *Quart. J. Roy. Meteor. Soc.*, **142**, 574–582, https://doi.org/10.1002/qj.2437.

Jung, T., and Coauthors, 2016: Advancing polar prediction capabilities on daily to seasonal time

scales. *Bull. Amer. Meteor. Soc.*, **97**, 1631–1647, https://doi.org/10.1175/BAMS-D-14-00246.1.

Kohonen, T., 1995: *Self-Organizing Maps.* Springer, 392 pp.

Korfe, N. G., and B. A. Colle, 2018: Evaluation of cool-season extratropical cyclones in a multimodel ensemble for eastern North America and the Western Atlantic Ocean. *Wea. Forecasting*, **33**, 109–127, https://doi.org/10.1175/WAF-D-17-0036.1.

Kuo, Y.-H., and R. J. Reed, 1988: Numerical simulation of an explosively deepening cyclone in the eastern Pacific. *Mon. Wea. Rev.*, **116**, 2081–2105, https://doi.org/10.1175/1520-0493(1988)116<2081:NSOAED>2.0.CO;2.

Kuo, Y.-H., M. A. Shapiro, and E. G. Donall, 1991: The interaction between baroclinic and diabatic processes in a numerical simulation of a rapidly intensifying extratropical marine cyclone. *Mon. Wea. Rev.*, **119**, 368–384, https://doi.org/10.1175/1520-0493(1991)119<0368:TIBBAD>2.0.CO;2.

Lamberson, W. S., R. D. Torn, L. F. Bosart, and L. Magnusson, 2016: Diagnosis of the source and evolution of medium-range forecast errors for Extratropical Cyclone Joachim. *Wea. Forecasting*, **31**, 1197–1214, https://doi.org/10.1175/WAF-D-16-0026.1.

Langland, R. H., M. A. Shapiro, and R. Gelaro, 2002: Initial condition sensitivity and error growth in forecasts of the 25 January 2000 East Coast snowstorm. *Mon. Wea. Rev.*, **130**, 957–974, https://doi.org/10.1175/1520-0493(2002)130<0957:ICSAEG>2.0.CO;2.

Lawrence, H., N. Bormann, I. Sandu, J. Day, J. Farnan, P. Bauer, 2019: Use and impact of Arctic observations in the ECMWF numerical weather prediction system. *Quart. J. Roy. Meteor. Soc.*, **145**, 3432–3454, https://doi.org/10.1002/qj.3628.

Lillo, S. P., and D. B. Parsons, 2017: Investigating the dynamics of error growth in ECMWF medium-range forecast busts. *Quart. J. Roy. Meteor. Soc.*, **143**, 1211–1226, https://doi.org/10.1002/qj.2938.

Lillo, S. P., S. M. Cavallo, D. B. Parsons, and C. Riedel, 2021: The role of a tropopause polar vortex in the generation of the January 2019 extreme Arctic outbreak. *J. Atmos. Sci.*, **78**, 2801–2821, https://doi.org/10.1175/JAS-D-20-0285.1.

Lukovich, J. V., J. C. Stroeve, A. Crawford, L. Hamilton, M. Tsamados, H. Heorton, and F. Massonnet, 2021: Summer extreme cyclone impacts on Arctic sea ice. *J. Climate*, **34**, 4817–4834, https://doi.org/10.1175/JCLI-D-19-0925.1.

Madonna, E., M. Boettcher, C. M. Grams, H. Joos, O. Martius, and H. Wernli, 2015: Verification of North Atlantic warm conveyor belt outflows in ECMWF forecasts. *Quart. J. Roy. Meteor. Soc.*, **141**, 1333–1344, https://doi.org/10.1002/qj.2442.

Madonna, E., G. Hes, C. Li, C. Michel, and P. Y. F. Siew, 2020: Control of Barents Sea wintertime cyclone variability by large-scale atmospheric flow. *Geophys. Res. Lett.*, **47**, e2020GL090322, https://doi.org/10.1029/2020GL090322.

Maher, P. T., 2017: Tourism futures in the Arctic. *The interconnected Arctic—UArctic Congress 2016*, K. Latola and H. Savela, Eds., Springer, Cham, 213–220.

Martin, J. E., 2006: *Mid-latitude Atmospheric Dynamics: A First Course.* John Wiley and Sons, 324 pp.

Martínez-Alvarado, O., E. Madonna, S. Gray, and H. Joos, 2016: A route to systematic error in forecasts of Rossby waves. *Quart. J. Roy. Meteor. Soc.*, **142**, 196–210, https://doi.org/10.1002/qj.2645.

Melia, N., K. Haines, and E. Hawkins, 2016: Sea ice decline and 21st century trans-Arctic shipping routes. *Geophys. Res. Lett.*, **43**, 9720–9728, https://doi.org/10.1002/2016GL069315.

Melia, N., K. Haines, E. Hawkins, and J. J. Day, 2017: Towards seasonal Arctic shipping route predictions. *Environ. Res. Lett.*, **12**, 084005, https://doi.org/10.1088/1748-9326/AA7A60.

Messori, G., C. Woods, and R. Caballero, 2018: On the drivers of wintertime temperature extremes in the high Arctic. *J. Climate*, **31**, 1597–1618, https://doi.org/10.1175/JCLI-D-17-0386.1.

Moore, B. J., 2017: Rossby wave breaking and widespread extreme precipitation events in the central and eastern U.S. Ph.D. dissertation, University at Albany, State University of New York, Albany, NY, 182 pp.

Moore, G. W. K., 2016: The December 2015 North Pole warming event and the increasing occurrence of such events. *Sci. Rep.*, **6**, 39084, https://doi.org/10.1038/srep39084.

Ogi, M., K. Yamazaki, and Y. Tachibana, 2004: The summertime annular mode in the Northern Hemisphere and its linkage to the winter mode. *J. Geophys. Res.*, **109**, D20114, https://doi.org/10.1029/2004JD004514.

Parkinson, C. L., and J. C. Comiso, 2013: On the 2012 record low Arctic sea ice cover: Combined impact of preconditioning and an August storm. *Geophys. Res. Lett.*, **40**, 1356–1361, https://doi.org/10.1002/grl.50349.

Peng, L., X. Zhang, J.-H. Kim, K.-H. Cho, B.-M. Kim, Z. Wang, and H. Tang, 2021: Role of intense Arctic storm in accelerating summer sea ice melt: An in situ observational study. *Geophys. Res. Lett.*, **48**, e2021GL092714, https://doi.org/10.1029/2021GL092714.

Pyle, M. E., D. Keyser, and L. F. Bosart, 2004: A diagnostic study of jet streaks: Kinematic

signatures and relationship to coherent tropopause disturbances. *Mon. Wea. Rev.*, **132**, 297–319, https://doi.org/10.1175/1520-0493(2004)132<0297:ADSOJS>2.0.CO;2.

Reed, R. J., A. J. Simmons, M. D. Albright, and P. Undén, 1988: The role of latent heat release in explosive cyclogenesis: Three examples based on ECMWF operational forecasts. *Wea. Forecasting*, **3**, 217–229, https://doi.org/10.1175/1520-0434(1988)003<0217:TROLHR>2.0.CO;2.

Reed, R. J., M. T. Stoelinga, and Y.-H. Kuo, 1992: A model-aided study of the origin and evolution of the anomalously high potential vorticity in the inner region of a rapidly deepening marine cyclone. *Mon. Wea. Rev.*, **120**, 893–913, https://doi.org/10.1175/1520-0493(1992)120<0893:AMASOT>2.0.CO;2.

Rodwell, J., and Coauthors, 2013: Characteristics of occasional poor medium-range weather forecasts for Europe. *Bull. Amer. Meteor. Soc.*, **94**, 1393–1405, https://doi.org/10.1175/BAMS-D-12-00099.1.

Sanders, F., 1986: Explosive cyclogenesis over the west-central North Atlantic Ocean, 1981–84. Part II: Evaluation of LFM model performance. *Mon. Wea. Rev.*, **114**, 2207–2218, https://doi.org/10.1175/1520-0493(1986)114<2207:ECOTWC>2.0.CO;2.

Sanders, F., 1992: Skill of operational dynamical models in cyclone prediction out to five-days range during ERICA. *Wea. Forecasting*, **7**, 3–25, https://doi.org/10.1175/1520-0434(1992)007<0003:SOODMI>2.0.CO;2.

Sanders, F., S. L. Mullen, and D. P. Baumhefner, 2000: Ensemble simulations of explosive cyclogenesis at ranges of 2–5 days. *Mon. Wea. Rev.*, **128**, 2920–2934, https://doi.org/10.1175/1520-0493(2000)128<2920:ESOECA>2.0.CO;2.

Sandu, I., and P. Bauer, 2018: Improving prediction and climate monitoring of polar regions–challenges and priorities. ECMWF science blog, https://www.ecmwf.int/en/about/media-centre/science-blog/2018/improving-prediction-and-climate-monitoring-polar-regions.

Screen, J. A., and I. Simmonds, 2010: The central role of diminishing sea ice in the recent Arctic temperature amplification. *Nature*, **464**, 1334–1337, https://doi.org/10.1038/nature09051.

Selz, T., and G. C. Craig, 2015: Upscale error growth in a high resolution simulation of a summertime weather event over Europe. *Mon. Wea. Rev.*, **143**, 813–827, https://doi.org/10.1175/MWR-D-14-00140.1.

Serreze, M. C., 1995: Climatological aspects of cyclone development and decay in the Arctic. *Atmos.–Ocean*, **33**, 1–23, https://doi.org/10.1080/07055900.1995.9649522.

Serreze, M. C., and A. P. Barrett, 2008: The summer cyclone maximum over the central Arctic

Ocean. *J. Climate*, **21**, 1048–1065, https://doi.org/10.1175/2007JCLI1810.1.

Serreze, M. C., F. Carse, R. G. Barry, and J. C. Rogers, 1997: Icelandic low cyclone activity: Climatological features, linkages with the NAO, and relationships with recent changes in the Northern Hemisphere circulation. *J. Climate*, **10**, 453–464, https://doi.org/10.1175/1520-0442(1997)010<0453:ILCACF>2.0.CO;2.

Serreze, M. C., A. H. Lynch, and M. P. Clark, 2001: The Arctic frontal zone as seen in the NCEP–NCAR reanalysis. *J. Climate*, **14**, 1550–1567, https://doi.org/10.1175/1520-0442(2001)014<1550:TAFZAS>2.0.CO;2.

Simmonds, I., and I. Rudeva, 2012: The great Arctic cyclone of August 2012. *Geophys. Res. Lett.*, **39**, L23709, https://doi.org/10.1029/2012GL054259.

Simmonds, I., and I. Rudeva, 2014: A comparison of tracking methods for extreme cyclones in the Arctic basin. *Tellus*, **66A**, 25252, https://doi.org/10.3402/tellusa.v66.25252.

Simmonds, I., C. Burke, and K. Keay, 2008: Arctic climate change as manifest in cyclone behavior. *J. Climate*, **21**, 5777–5796, https://doi.org/10.1175/2008JCLI2366.1.

Sprenger, M., and Coauthors, 2017: Global climatologies of Eulerian and Lagrangian flow features based on ERA-Interim. *Bull. Amer. Meteor. Soc.*, **98**, 1739–1748, https://doi.org/10.1175/BAMS-D-15-00299.1.

Stern, D. P, J. D. Doyle, N. P. Barton, P. M. Finocchio, W. A. Komaromi, and E. J. Metzger, 2020: The impact of an intense cyclone on short-term sea ice loss in a fully coupled atmosphere-ocean-ice model. *Geophys. Res. Lett.*, **47**, e2019GL085580, https://doi.org/10.1029/2019GL085580.

Stoelinga, M. T., 1996: A potential vorticity–based study of the role of diabatic heating and friction in a numerically simulated baroclinic cyclone. *Mon. Wea. Rev.*, **124**, 849–874, https://doi.org/10.1175/1520-0493(1996)124<0849:APVBSO>2.0.CO;2.

Stroeve, J., M. M. Holland, W. Meier, T. Scambos, and M. C. Serreze, 2007: Arctic sea ice decline: Faster than forecast. *Geophys. Res. Lett.*, **34**, L09501, https://doi.org/10.1029/2007GL029703.

Tanaka, H. L., A. Yamagami, and S. Takahashi, 2012: The structure and behavior of the arctic cyclone in summer analyzed by the JRA-25/JCDAS data. *Polar Sci.*, **6**, 55–69, https://doi.org/10.1016/j.polar.2012.03.001.

Tao, W., J. Zhang, and X. Zhang, 2017a: The role of stratosphere vortex downward intrusion in a long-lasting late-summer Arctic storm. *Quart. J. Roy. Meteor. Soc.*, **143**, 1953–1966, https://doi.org/10.1002/qj.3055.

Tao, W., J. Zhang, Y. Fu, and X. Zhang, 2017b: Driving roles of tropospheric and stratospheric

thermal anomalies in intensification and persistence of the Arctic superstorm in 2012. *Geophys. Res. Lett.*, **44**, 10017–10025, https://doi.org/10.1002/2017GL074778.

Thompson, D. W. J., and J. M. Wallace, 1998: The Arctic Oscillation signature in the wintertime geopotential height and temperature fields. *Geophys. Res. Lett.*, **25**, 1297–1300, https://doi.org/10.1029/98GL00950.

Thomson, J., and W. E. Rogers, 2014: Swell and sea in the emerging Arctic Ocean. *Geophys. Res. Lett.*, **41**, 3136–3140, https://doi.org/10.1002/2014GL059983.

Torn, R. D., 2017: A comparison of the downstream predictability associated with ET and baroclinic cyclones. *Mon. Wea. Rev.*, **145**, 4651–4672, https://doi.org/10.1175/MWR-D-17-0083.1.

Torn, R. D., and G. J. Hakim, 2008: Ensemble-based sensitivity analysis. *Mon. Wea. Rev.*, **136**, 663–677, https://doi.org/10.1175/2007MWR2132.1.

Torn, R. D., and G. J. Hakim, 2015: Comparison of wave packets associated with extratropical transition and winter cyclones. *Mon. Wea. Rev.*, **143**, 1782–1803, https://doi.org/10.1175/MWR-D-14-00006.1.

Torn, R. D., and G. S. Romine, 2015: Sensitivity of central Oklahoma convection forecasts to upstream potential vorticity anomalies during two strongly forced cases during MPEX. *Mon. Wea. Rev.*, **143**, 4064–4087, https://doi.org/10.1175/MWR-D-15-0085.1.

Tracton, M. S., 1973: The role of cumulus convection in the development of extratropical cyclones. *Mon. Wea. Rev.*, **101**, 573–593, https://doi.org/10.1175/1520-0493(1973)101<0573:TROCCI>2.3.CO;2.

Tribbia, J. J., and D. P. Baumhefner, 2004: Scale interactions and atmospheric predictability: An updated perspective. *Mon. Wea. Rev.*, **132**, 703–713, https://doi.org/10.1175/1520-0493(2004)132<0703:SIAAPA>2.0.CO;2.

Uccellini, L. W., and P. J. Kocin, 1987: The interaction of jet streak circulations during heavy snow events along the East Coast of the United States. *Wea. Forecasting*, **2**, 289–308, https://doi.org/10.1175/1520-0434(1987)002<0289:TIOJSC>2.0.CO;2.

U.S. Department of the Navy, 2021: A strategic blueprint for the Arctic. 28 pp, https://media.defense.gov/2021/Jan/05/2002560338/-1/-1/0/ARCTIC%20BLUEPRINT%202021%20FINAL.PDF/ARCTIC%20BLUEPRINT%202021%20FINAL.PDF.

Valkonen, E., J. Cassano, and E. Cassano, 2021: Arctic cyclones and their interactions with the declining sea ice: A recent climatology. *J. Geophys. Res. Atmos.*, **126**, e2020JD034366. https://doi.org/10.1029/2020JD034366.

Wernli, H., and C. Schwierz, 2006: Surface cyclones in the ERA40 data set (1958–2001). Part I: Novel identification method and global climatology. *J. Atmos. Sci.,* **63**, 2486–2507, https://doi.org/10.1175/JAS3766.1.

Wernli, H., S. Dirren, M. A. Liniger, and M. Zillig, 2002: Dynamical aspects of the life cycle of the winter storm 'Lothar' (24–26 December 1999). *Quart. J. Roy. Meteor. Soc.*, **128**, 405–429, https://doi.org/10.1256/003590002321042036.

Yamagami, A., and M. Matsueda, 2021: Statistical characteristics of Arctic forecast busts and their relationship to Arctic weather patterns in summer. *Atmos. Sci. Lett.*, **22**, e1038. https://doi.org/10.1002/asl.1038.

Yamagami, A., M. Matsuda, and H. L. Tanaka, 2017: Extreme Arctic cyclone in August 2016. *Atmos. Sci. Lett.*, **18**, 307–314, https://doi.org/10.1002/asl.757.

Yamagami, A., M. Matsueda, and H. L. Tanaka, 2018a: Predictability of the 2012 great Arctic cyclone on medium-range timescales. *Polar Sci.*, **15**, 13–23, https://doi.org/10.1016/j.polar.2018.01.002.

Yamagami, A., M. Matsueda, and H. L. Tanaka, 2018b: Medium-range forecast skill for extraordinary Arctic cyclones in summer of 2008–2016. *Geophys. Res. Lett.*, **45**, 4429–4437, https://doi.org/10.1029/2018GL077278.

Yamagami, A., M. Matsueda, and H. L. Tanaka, 2019: Skill of medium-range reforecast for summertime extraordinary Arctic cyclones in 1986–2016. *Polar Sci.*, **20**, 107–116, https://doi.org/10.1016/j.polar.2019.02.003.

Yamazaki, A., J. Inoue, K. Dethloff, M. Maturilli, and G. König-Langlo, 2015: Impact of radiosonde observations on forecasting summertime arctic cyclone formation. *J. Geophys. Res. Atmos.*, **120**, 3249–3273, https://doi.org/10.1002/2014JD022925.

Zhang, F., C. Snyder, and R. Rotunno, 2003: Effects of moist convection on mesoscale predictability. *J. Atmos. Sci.*, **60**, 1173–1185, https://doi.org/10.1175/1520-0469(2003)060<1173:EOMCOM>2.0.CO;2.

Zhang, F., N. Bei, R. Rotunno, C. Snyder, and C. C. Epifanio, 2007: Mesoscale predictability of moist baroclinic waves: Convection-permitting experiments and multistage error growth dynamics. *J. Atmos. Sci.*, **64**, 3579–3594, https://doi.org/10.1175/JAS4028.1.

Zhang, J., R. Lindsay, A. Schweiger, and M. Steele, 2013: The impact of an intense summer cyclone on 2012 Arctic sea ice retreat. *Geophys. Res. Lett.*, **40**, 720–726, https://doi.org/10.1002/grl.50190.

Zhang, X., J. E. Walsh, J. Zhang, U. S. Bhatt, and M. Ikeda, 2004: Climatology and interannual variability of Arctic cyclone activity: 1948–2002. *J. Climate*, **17**, 2300–2317, https://doi.org/10.1175/1520-0442(2004)017<2300:CAIVOA>2.0.CO;2.

Zheng, M., E. K. M. Chang, and B. A. Colle, 2013: Ensemble sensitivity tools for assessing extratropical cyclone intensity and track predictability. *Wea. Forecasting*, **28**, 1133–1156, https://doi.org/10.1175/WAF-D-12-00132.1.

Zhu, H., and A. Thorpe, 2006: Predictability of extratropical cyclones: The influence of initial condition and model uncertainties. *J. Atmos. Sci.*, **63**, 1483–1497, https://doi.org/10.1175/JAS3688.1.